



POLITECNICO
MILANO 1863

SCUOLA DI INGEGNERIA INDUSTRIALE
E DELL'INFORMAZIONE

Techno-economic analysis and optimization of large-scale modular CSP tower plants

TESI DI LAUREA MAGISTRALE IN
ENERGY ENGINEERING - INGEGNERIA ENERGETICA

Author: **Rocco Manfredi Selvaggi**

Student ID: 963409

Advisor: Prof. Giampaolo Manzolini

Co-advisors: Giancarlo Gentile, Ettore Morosini

Academic Year: 2021-22

Abstract

The rapid growth in the installed capacity from variable renewable sources is increasingly problematic for the electric grid. Thus, concentrated solar power (CSP) appears promising, offering a low-cost thermal storage and decoupling the solar resource from the electric generation. The modular configuration, in which modules are connected to a single thermal storage and power block, solves the optical performance decay for large powers, and takes advantage of the economies of scale of the power block.

In this thesis, a techno-economic analysis of large-scale modular CSP plants using molten salts as heat transfer fluid and Rankine cycles is developed. Solar fields are analysed using SolarPILOT, receivers with a Matlab model and Rankine cycles with Thermoflex. In addition, a Matlab model developed from scratch is used for the analysis and optimization of the piping system, allowing the evaluation of thermal losses, pressure losses, and costs. A bottom-up methodology is also developed for designing and optimizing modular plants. Modules of different sizes and geometries are compared using the LCOH indicator, while plants are compared based on LCOE and LSP, a new parameter indicating the plants' compactness.

The results highlight the cost-effectiveness of square modules over free-shape ones, and the techno-economic benefits offered by placing the tower in the centre of circular and square modules. Configurations with polar square modules reduce the LCOE compared to equivalent conventional plants of 110 MW_{el}, at the expense of a lower compactness. The use of surrounded square modules, instead, offers much more compact plants. In the case of 45 MW_{el} with hazy sky, the modular system results in lower LCOE and a higher compactness. Finally, the study of modular plants up to 500 MW_{el} shows a gradual increase in the LCOE due to the piping system, emphasizing the convenience of plants up to 300 MW_{el} and of 2-reheats Rankine cycles. In conclusion, over a wide range of latitudes and in the case of hazy sky, large-scale modular plants offer lower LCOE by employing square polar modules and greater compactness by using square surrounded modules.

Keywords: LCOE, CSP, modular, multiple towers, piping system

Abstract in lingua italiana

Il rapido aumento della capacità installata da fonti rinnovabili variabili è sempre più problematico per la rete elettrica. Il solare termodinamico a concentrazione (CSP) appare dunque promettente, offrendo un accumulo di calore a basso costo e disaccoppiando la risorsa solare dalla generazione elettrica. La configurazione modulare, in cui i moduli sono collegati ad un unico sistema di accumulo e ciclo di potenza, risolve il decadimento delle prestazioni ottiche ad elevate potenze, e sfrutta le economie di scala del ciclo di potenza.

Nella presente tesi si sviluppa un'analisi tecno-economica di impianti CSP modulari di grande taglia, che impiegano sali fusi come fluido termovettore e cicli Rankine. I campi solari sono analizzati con SolarPILOT, i ricevitori con un modello Matlab e i cicli Rankine con Thermoflex. Inoltre, si sviluppa integralmente un modello Matlab per l'analisi e l'ottimizzazione del sistema di tubature del fluido termovettore, permettendo la valutazione delle perdite termiche, di pressione, e dei costi. Si definisce anche una metodologia dettagliata per il dimensionamento e l'ottimizzazione di impianti modulari. Moduli di diverse taglie e geometrie sono confrontati tramite l'indicatore LCOH, mentre gli impianti sono confrontati tramite LCOE e LSP, nuovo parametro che ne indica la compattezza.

I risultati evidenziano la convenienza dei moduli quadrati rispetto a quelli con forma libera, oltre ai benefici tecno-economici offerti dal posizionamento della torre al centro dei moduli circolari e quadrati. Configurazioni con moduli quadrati polari riducono il parametro LCOE rispetto ad impianti convenzionali equivalenti da 110 MW_{el} , a sfavore di una compattezza inferiore. L'impiego di moduli quadrati circondati offre invece impianti molto più compatti. Nel caso di potenze di 45 MW_{el} ad elevata foschia, la soluzione modulare offre un LCOE inferiore e una compattezza maggiore. Infine, lo studio di impianti modulari fino a 500 MW_{el} evidenzia un progressivo incremento del LCOE a causa del sistema di tubature, sottolineando la convenienza di impianti fino a 300 MW_{el} e di cicli Rankine con 2 risurriscaldamenti. In sintesi, in un ampio intervallo di latitudini e ad elevata foschia, gli impianti modulari di grande taglia offrono LCOE inferiori impiegando moduli polari quadrati e maggiori compattezze utilizzando moduli quadrati circondati.

Parole chiave: LCOE, CSP, modulare, torri multiple, sistema di tubature

Contents

Abstract	i
Abstract in lingua italiana	iii
Contents	v
1 Introduction	1
2 Concentrated Solar Power	9
2.1 Solar resource	10
2.2 Concentration systems	12
2.2.1 Parabolic trough	13
2.2.2 Linear Fresnel	14
2.2.3 Parabolic dish	14
2.2.4 Solar tower	14
2.3 Solar tower components	15
2.3.1 Heliostat field	15
2.3.2 Receiver	17
2.3.3 Tower	18
2.3.4 Piping system, HTF, TES	20
2.3.5 Power block	22
2.4 State of the art	23
2.5 Research trends	23
2.6 Modular technology	26
2.6.1 Literature review and existing plants	26
2.6.2 Advantages	28
2.6.3 Disadvantages	29
3 Methodology	31

3.1	Solar field model	32
3.1.1	Optical efficiency	38
3.1.2	Off-design	39
3.2	Receiver thermal model	41
3.2.1	Off-design	44
3.3	Piping system model	44
3.3.1	Structure	45
3.3.2	Pressure constraints	47
3.3.3	Mechanical design and thermal losses	48
3.3.4	Pressure losses	51
3.3.5	Velocity optimization	52
3.3.6	Off-design	53
3.4	Power Block model	54
3.4.1	1-reheat cycle	55
3.4.2	2-reheats cycle	55
3.4.3	Off-design	56
3.5	Modular plant design and optimization	56
3.6	Conventional plant design and optimization	59
3.7	Annual analysis	60
4	Case study	63
4.1	Vast Solar modules	63
4.2	Large scale modular plants	63
4.2.1	Locations and scenarios	64
4.2.2	Solar field	67
4.2.3	Tower, Receiver	69
4.2.4	Piping, TES	70
4.2.5	Power block	71
4.3	Cost model	71
4.3.1	CAPEX	71
4.3.2	OPEX	77
4.3.3	LCOE	78
4.3.4	LCOH	78
5	Results and discussion	81
5.1	Billboard discretization	81
5.2	Vast Solar modules	82
5.2.1	Optical efficiency maps	82

5.2.2	Receiver tubes diameter optimization	83
5.2.3	Receiver size optimization	84
5.3	Large scale modular plants	85
5.3.1	Tower location in surrounded modules	85
5.3.2	Modules	91
5.3.3	Plants	101
5.3.4	Modularity up to 500 MW _{el}	110
6	Conclusions and future developments	115
	Bibliography	119
A	Appendix A	125
B	Appendix B	127
	List of Figures	129
	List of Tables	133
	Ringraziamenti	135

1 | Introduction

In recent decades, the topic of energy has been gaining a more central place in the global debate. The various conjugations of climate change are now increasingly evident in the world in which we live. Extreme heat waves, the magnitude of wildfires, periods of droughts alternating with increasingly intense storm events and floods, the rapid melting of glaciers and polar ice caps, the resulting rise in the sea levels, are just a few alarm bells that our planet is changing rapidly. Most of these events can be traced back to the rise in the global average temperature (global warming), which compared to pre-industrial levels has now reached $+1.01^{\circ}\text{C}$ [1] as shown in Figure 1.1 and is heading toward $+1.5^{\circ}\text{C}$ or even $+2^{\circ}\text{C}$ by 2100. As reported in [2], "we have already passed the point of no return for the modest climate-action scenario where the share of renewables increases by 2% each year. In this scenario, unless we remove carbon dioxide from the atmosphere, it is no longer possible to achieve the 1.5°C target in 2100 with a probability of 67%".

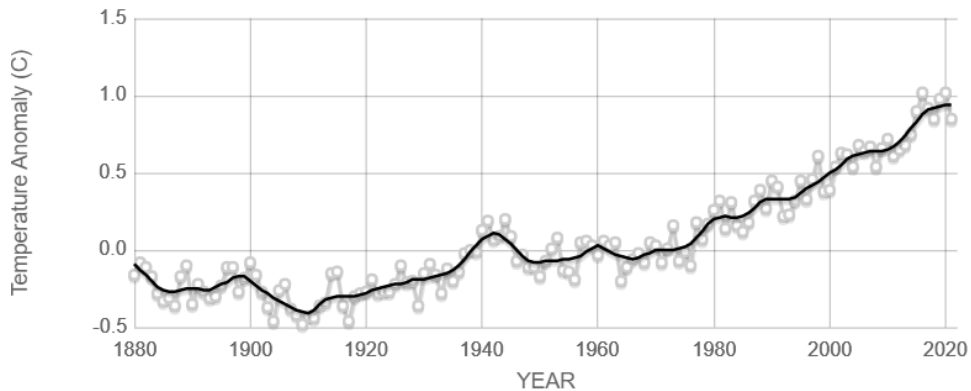


Figure 1.1: Global temperature anomaly compared to pre-industrial levels [1]

The increase in the planet's average temperature is a direct consequence of the growth in the concentration of greenhouse gases (GHG) in the atmosphere. The molecules of these gases absorb and re-emit some of the infrared radiation emitted from the Earth's surface, overheating the planet and reducing the amount of radiation that passes through the atmosphere and is lost in space [3]. The main greenhouse gases are water vapor (H_2O), carbon dioxide (CO_2), methane (CH_4), ozone (O_3), nitrous oxides (N_2O), and

fluorocarbons [4]. In Figure 1.2 the trend of the main anthropogenic GHG emissions over the last decades is illustrated.

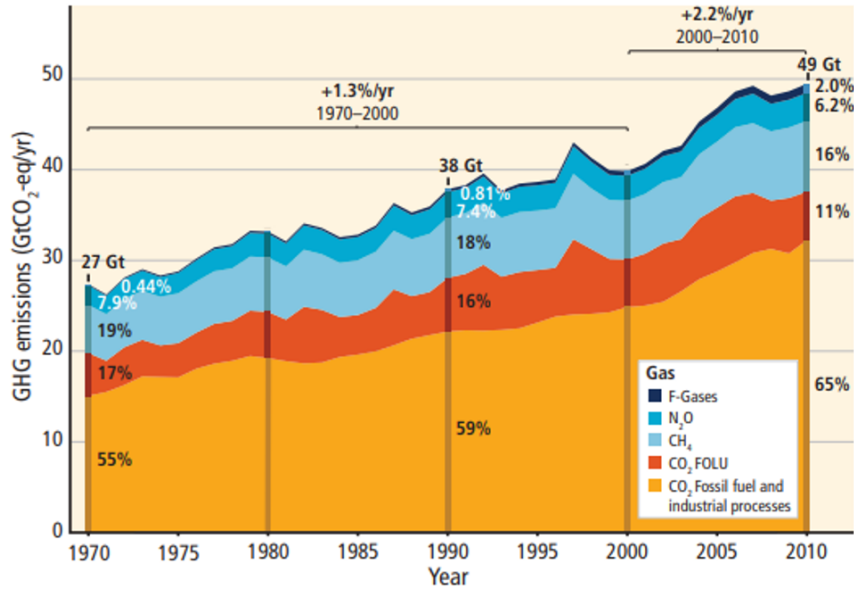


Figure 1.2: Total annual anthropogenic GHG emissions by gases 1970 – 2010 [5]

CO₂, resulting from the combustion of fossil fuels' carbon chains and from industrial processes, constitutes the main component by mass and it is also the one with the most significant growth. Figure 1.3 shows the trend of the average CO₂ concentration in the atmosphere over the last 800.000 years, which varies in accordance with the changes in the Earth's orbit dictated by the Milanković cycles [6].

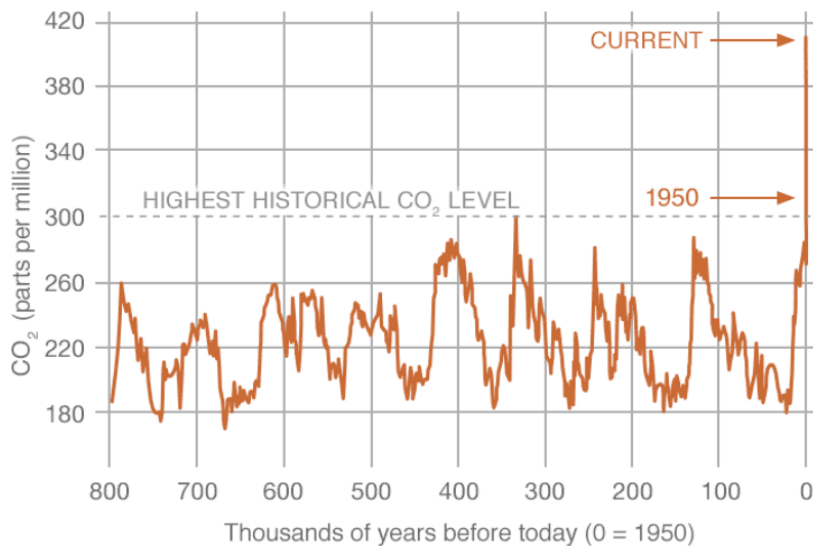


Figure 1.3: Historical trend of the CO₂ atmospheric concentration [1]

From the 1950 values, the measured CO₂ concentration grew to values never seen before, reaching 419 ppm in 2022 [1], a +50% compared to the beginning of industrial era. This abrupt change, which is occurring on a human time scale rather than a geological scale, is uniquely attributable to humans, as confirmed by the outcomes obtained from [7] according to which 97.1% of the scientific literature agrees with the anthropogenic global warming thesis.

To limit the effect of a disastrous change in the planet's climate, it is therefore necessary to immediately curb CO₂ emissions by adopting green technologies in all responsible sectors, such as power generation, industry, transportation, and residential. In this regard, it is needed to adopt as soon as possible the use of renewable and nuclear technologies coupled with cheap and environmentally friendly storage systems. Some sectors can be greatly electrified, while low-carbon fuels, such as biofuels or green hydrogen, should be employed in those sectors that are harder to electrify

In addition, energy is an instrumental right that is closely interconnected with the environment and the society [8]. In fact, it accelerates the countries' socio-economic development and improves the quality of life. In this regard, Sustainable Development Goal (SDG) number 7, established by the United Nations in the 2030 Agenda for Sustainable Development, states: "Ensure access to affordable, reliable, sustainable and modern energy for all" [9]. Energy ensures some basic human needs such as food preservation and agriculture, water purification and distribution, health, education, security, and development of economic activities. As shown in Figure 1.4, Total Energy Supply per capita and Gross National Income per capita have an almost linear trend, especially in low-income countries. Consequently, it can be inferred that the energy supply is an index of economic development.

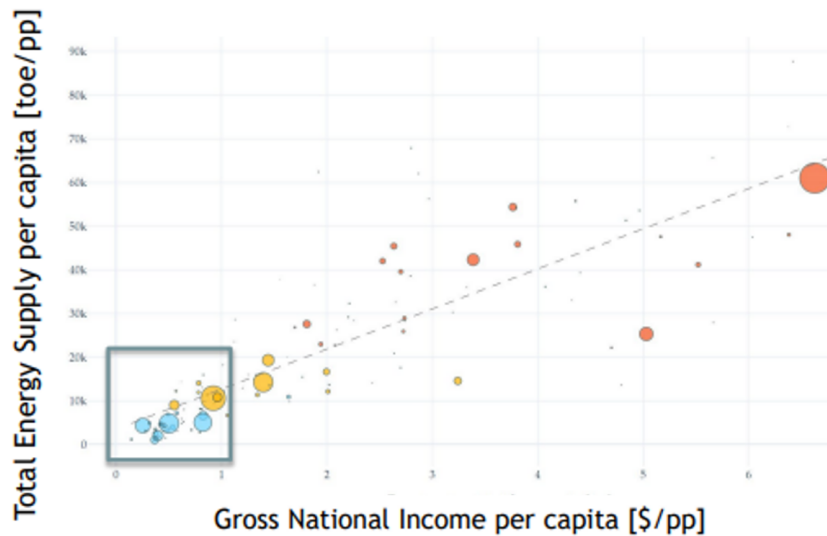


Figure 1.4: Total energy supply per capita over gross national income per capita of all the countries worldwide [8]

In this context, renewable energy sources enable a fast achievement of SDG 7, since more than 1 billion people worldwide still lack access to electricity and 2.7 billion still rely on traditional biomass like wood and agricultural by-products for domestic needs [8]. Renewables enable decentralized power generation, being more scalable and modular than traditional fossil fuelled power plants, saving transmission and distribution costs and allowing access to electricity even in remote locations. Second, they are often economically competitive with traditional fossil sources and exploit local resources, eliminating the fuel supply-chain issues and increasing countries' energy security. Finally, they greatly reduce the GHG and pollutant gases emissions, allowing to fight climate change in the light of SDG 13 “Take urgent action to combat climate change and its impacts” [9].

Due to the recent war in Europe and its strategic and political consequences, the price of some fossil fuels has increased significantly, especially natural gas, as shown in Figure 1.5. This makes even more clear the need to invest in energy sources that are independent of the randomness of gas prices, and provides the opportunity to achieve a marked reduction of direct CO₂ emissions from the energy sector. Moreover, at current gas prices, renewable sources become automatically more competitive from a power generation cost perspective. Figure 1.6 shows the recent electricity costs of the main renewable technologies.



Figure 1.5: EU natural gas price trend [€/MWh] in the last five years, updated to 21/10/2022 [10]

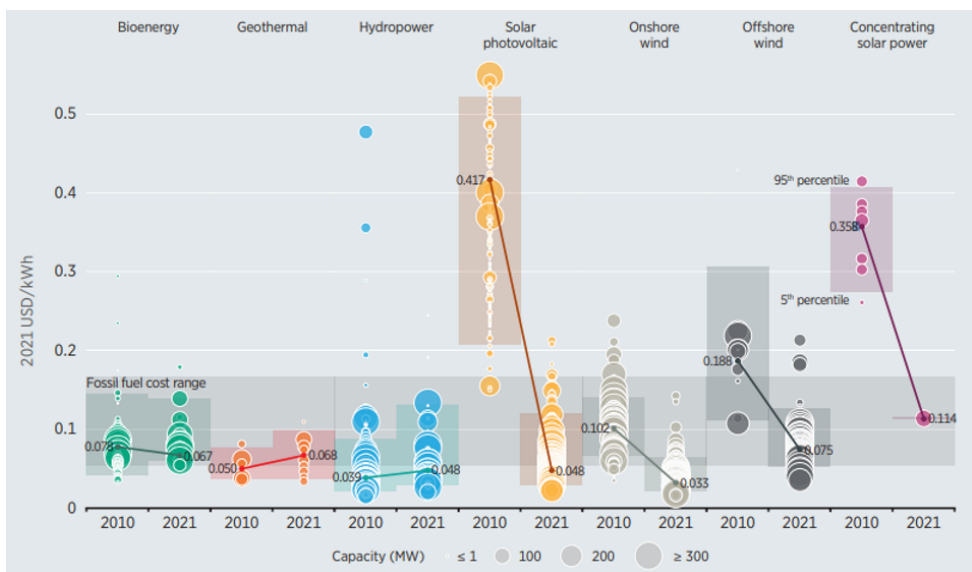


Figure 1.6: Global weighted average LCOEs [\$/kWh] from newly commissioned, utility-scale renewable power generation technologies, 2010 – 2021 [11]

A zero-emission future for the power sector is possible, but it is certainly not simple. Concerning electric power generation, renewables and nuclear will have to coexist, possibly the former to cover demand fluctuations and the latter for base load.

However, at present only 32 countries worldwide have operational fission nuclear reactors [12], and such technology is often discarded due to the fear of local populations. Italy, for example, ended the exploitation of nuclear power with the November 8th and 9th 1987

referendum, promoted in the aftermath of the Chernobyl's disaster on April 26th, 1986. In contrast to current fission technologies, nuclear fusion would offer much safer reactors and would avoid radioactive waste production, although the commercialization of this technology still seems far away. The most ambitious project for a large-scale nuclear fusion reactor is ITER (International Thermonuclear Experimental Reactor) [13]. This reactor, currently under construction, plans to ignite the first plasma in December 2025 and to start the deuterium-tritium operations in 2035. Thereafter, "ITER will contribute to the design of the next-generation machine, DEMO" that will begin the operations in the 2040s. "Beyond DEMO, the final step would be the construction of a prototype reactor, fully optimized to produce electricity competitively. [...] Most forecasts place this phase at the middle of the century".

Thus, the most accepted and quickly implementable green technologies are renewables, which are needed to meet the broad set of CO₂ emission reduction targets. In this scenario, a key role will be played by storage. In fact, looking for example at the trend of electricity generation from renewable sources in OECD countries over the last three decades (Figure 1.7), variable renewable energy sources (VRES) are growing rapidly. These are mainly wind and solar photovoltaic, but also the share of hydroelectric given by run off river plants. VRES are random, thus non-programmable and independent of the demand curve.

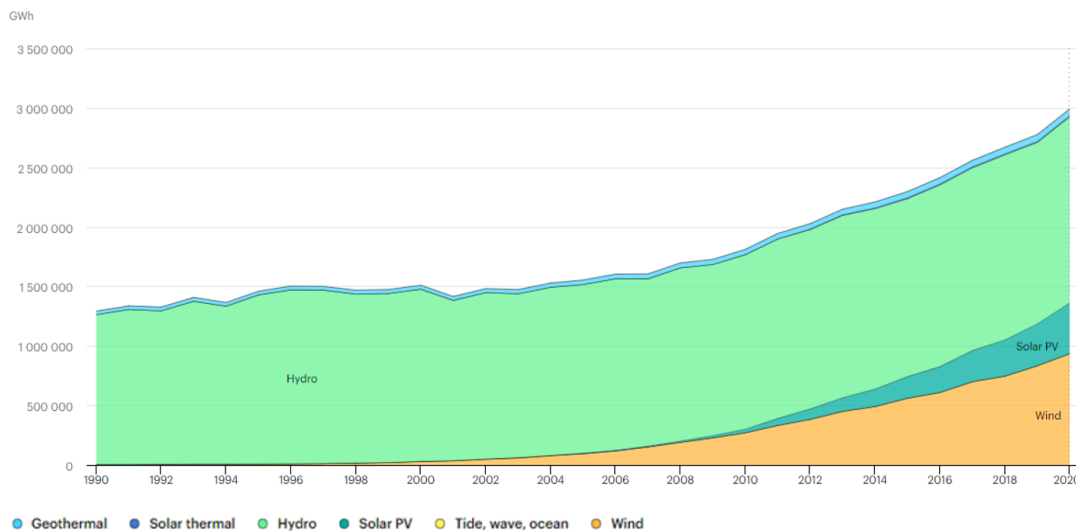


Figure 1.7: Renewable electricity generation by source (non-combustible), OECD Total 1990 – 2020 [14]

According to [15], as shown in Figure 1.8, above a certain threshold of energy generated by VRES, an excess of renewables starts to emerge and some storage systems are required.

This need increases further if high renewable penetration is to be achieved.

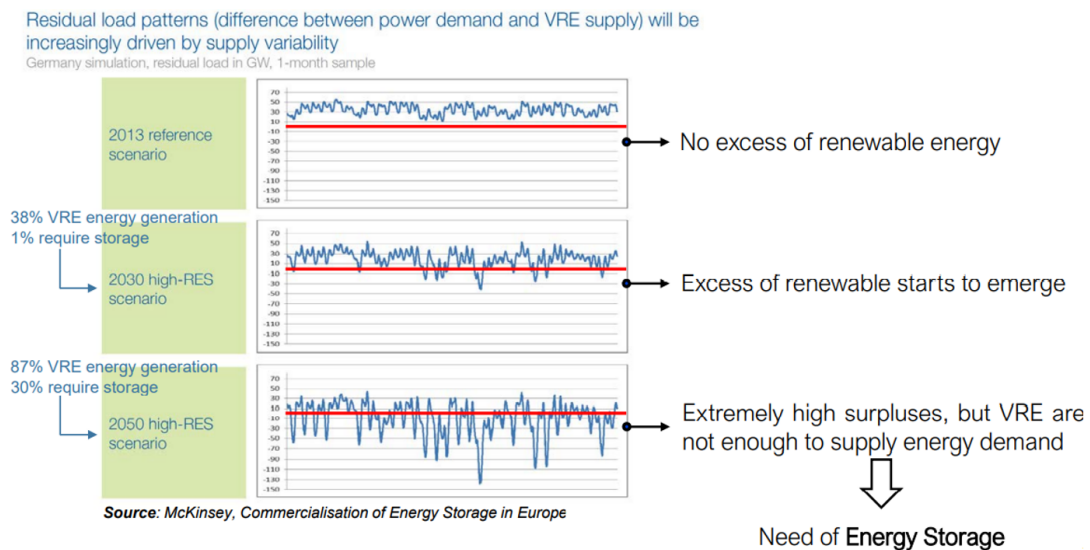


Figure 1.8: Effect of VRES electricity generation on the grid [16]

Looking at the broad spectrum of renewables, the solution is not unique, even excluding the large-scale application of Lithium-Ion batteries. In fact, Lithium batteries are very expensive – even the value of 71 \$/kWh_{el} projected for 2050 [17] is much higher than other storage technologies such as CSP, where the equivalent electric storage cost is 50-70 \$/MWh_{el} – and the supply chain issues are significant. Although wind and solar photovoltaic offer among the lowest production costs, they are not dispatchable, unlike other power generation technologies such as geothermal, biomass, hydroelectric with a reservoir and concentrated solar thermal. However, many of these solutions are very site-specific depending on the presence, respectively, of geothermal anomalies, forests or crop fields, mountains with sufficient altitudes and water flow rates, or highly irradiated regions at relatively low latitudes. Further storage possibilities are provided by pumped hydroelectric plants, hydrogen, and compressed air.

The study, development, and market competitiveness of dispatchable technologies and low-cost storage systems, capable of matching the power generation curve to the demand curve, are of paramount importance to achieving the goal of a high renewable penetration.

2 | Concentrated Solar Power

Concentrated Solar Power (CSP) is a renewable technology that converts solar radiation into electricity through a series of intermediate steps and using different components, including an energy storage system. This allows thermal energy to be stored during the day and to be converted into electricity at night, decoupling solar resource from power generation. Such programmability makes the plant dispatchable. However, such storage only occurs daily and not on a seasonal basis, unlike large hydroelectric dam plants.

The worldwide installed capacity of CSP plants is currently very low, only 6 GW compared to the 3146 GW of all renewables including hydropower in 2021 [18], while new installations are still proceeding slowly, as shown in Figure 2.1. However, the potential of this technology is undiscussed. In addition to being dispatchable, in fact, CSP can be synergistically coupled within hybrid plants to photovoltaic (PV), geothermal, biomass, and water desalination.

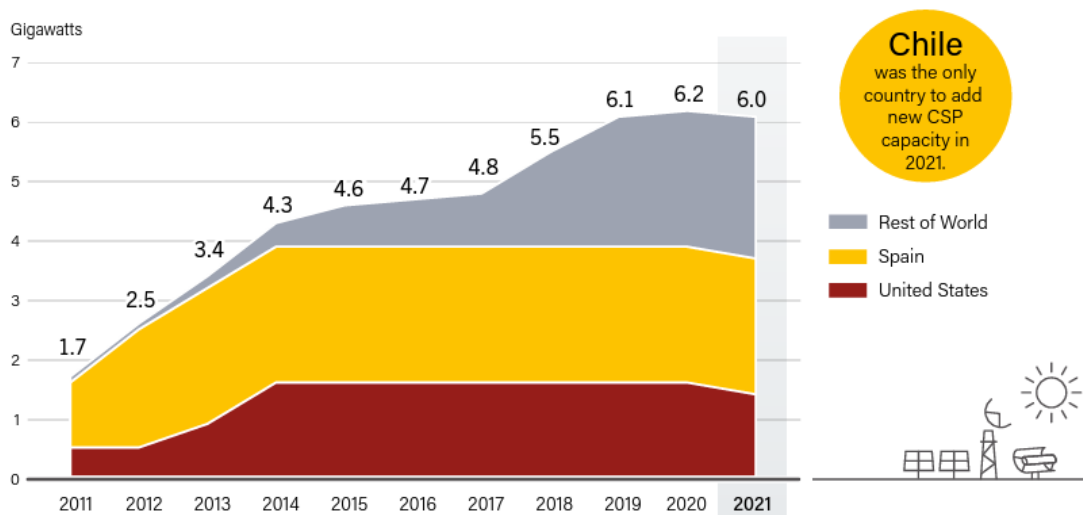


Figure 2.1: Concentrating solar thermal power global capacity, by country and region, 2011 – 2021 [18]

In CSP plants, solar energy faces three main conversion steps, all of which affect the plant efficiency. Each of them must be optimized to reduce the cost of energy production.

First, the direct solar radiation is collimated and concentrated onto a receiver through a reflection-based optical system, which must have high reflectivity especially at the wavelengths associated to the solar spectrum. Unlike PV, diffuse radiation, equivalent to around 10% of the total radiation, cannot be exploited [3]. Concentration is needed to increase the thermal efficiency and to reduce receiver costs, and involves the use of a tracking system to follow the variation in the sun position. In contrast, the principle of refraction is never employed on a large scale because of the enormous cost and size that lenses would have. Next, the receiver converts radiation into high-temperature thermal energy by means of a heat transfer fluid (HTF), which is then stored in the storage system. Finally, the HTF transfers heat to a power cycle, which converts it into electricity.

2.1. Solar resource

Solar radiation, resulting from the nuclear fusion of hydrogen atoms within the sun, reaches the outer limit of the Earth's atmosphere with an average power density of 1367 W/m^2 . This is the solar constant and establishes the limiting factor in terms of power production from solar technologies. The amount of radiation reaching the ground is always lower than the solar constant because of the atmospheric absorption and attenuation of some wavelengths due to molecules like H_2O and CO_2 . The resulting radiation depends on both atmospheric conditions and the thickness of the atmosphere crossed by the radiation. The Air Mass coefficient (AM) is the relative length of the direct-beam path along the atmosphere compared to a vertical path at sea level, at which $\text{AM} = 1$. An example of the AM coefficient is shown in Figure 2.2. Because of these effects, the maximum radiation on the Earth's surface under optimal conditions is around 1000 W/m^2 .

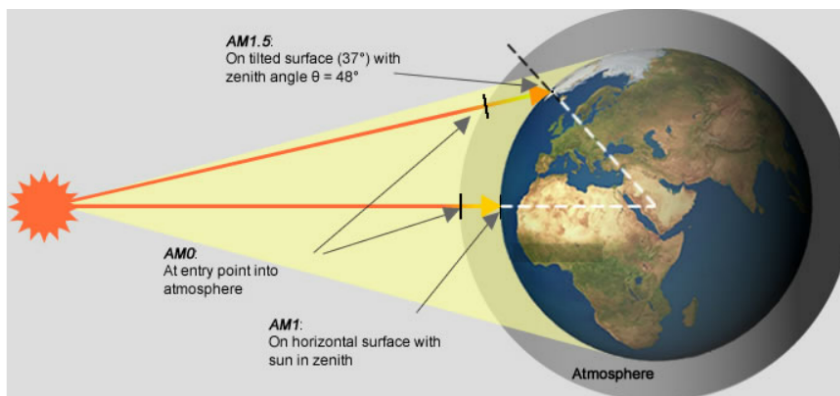


Figure 2.2: Examples of the Air Mass coefficient [19]

The solar radiation reaching the ground is very diluted, however, the total power received

by the planet's surface from the sun averages around 89000 TW while the world primary power average consumption is 20 TW [3]. Therefore, the enormous opportunity that such renewable source guarantees is evident. Two key indicators for assessing the feasibility of a Concentrating Solar Power plant are (DNI):

- Direct Normal Irradiance: amount of solar radiation received in a collimated beam on a surface normal to the sun at its current position in the sky [W/m^2]. The maximum value is around $1000 \text{ W}/\text{m}^2$.
- Direct Normal Irradiation: amount of solar radiation received in a collimated beam on a surface normal to the sun during a 60-minute period [$\text{kWh}/\text{m}^2\text{y}$]. The yearly DNI is the sum of the hourly Direct Normal Irradiations over the year and typical acceptable values for solar plants' construction correspond to yearly DNI $> 1800 \text{ kWh}/\text{m}^2\text{y}$.

Figure 2.3 shows the yearly DNI map worldwide, from which the most suitable locations for CSP plants can be identified.

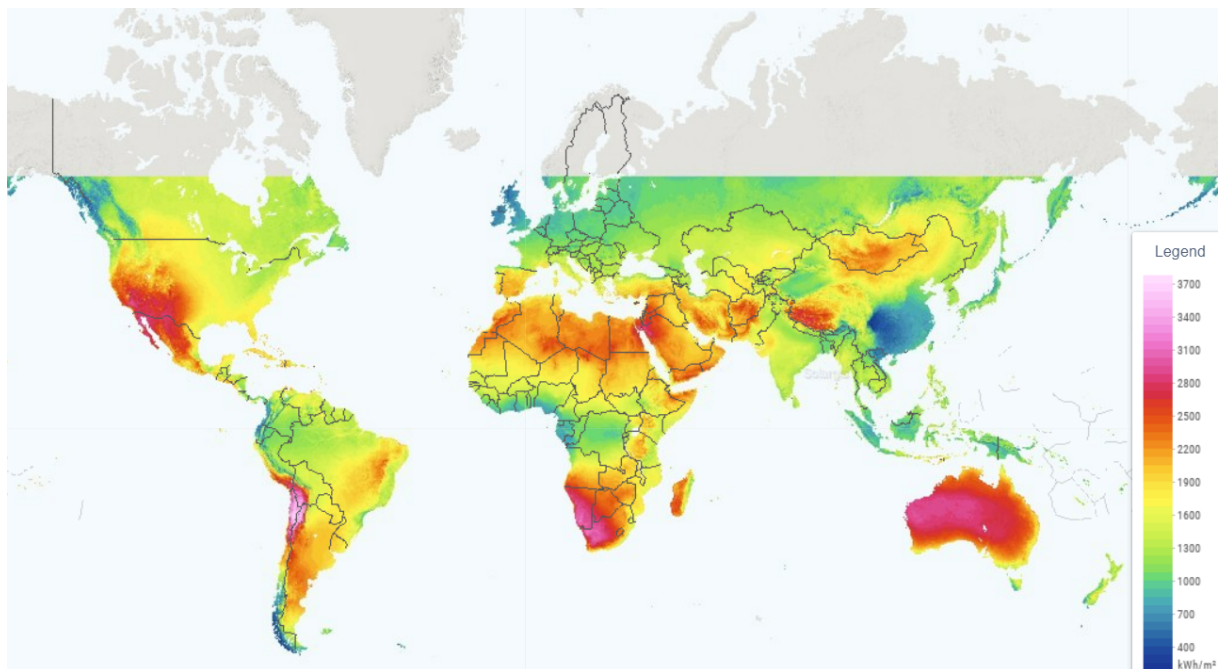


Figure 2.3: Yearly Direct Normal Irradiation worldwide [$\text{kWh}/\text{m}^2\text{y}$] [20]

The regions with larger DNIs are those around the Tropic of Cancer and the Tropic of Capricorn, at latitudes $+23^{\circ}26'$ and $-23^{\circ}26'$, respectively. Such low-latitude regions are characterized by low AM coefficients and are mostly desert, meaning scarcity of rainfalls and thus of cloud events that would reduce the DNI, as happens near the equator where

rainfalls are much more abundant. Moreover, the DNI in the Southern Hemisphere around the Tropic is on average higher than in the Northern Hemisphere, reaching its maximum in the Atacama Desert, in Chile, where values up to 3700 kWh/m²y can be obtained. This desert has a combination of very favourable conditions for a CSP installation: low latitude, very little rainfall, and high altitude, which further reduces the AM coefficient. Just for comparison, the maximum annual DNI in Italy, reached in Sicily, is around to 1900 kWh/m²y, while the peak value at European level is found in Spain and does not exceed 2300 kWh/m²y.

Thus, it is possible to fully understand how CSP technology, as renewable, dispatchable, and easily coupled with seawater desalination plants, is essential in certain regions of the planet. This is the case of low-latitude arid regions, where little rainfall precludes both hydropower and the presence of biomass, in contexts often lacking geothermal anomalies.

2.2. Concentration systems

Four different optical concentration systems exist, and they are classified according to the shape of the receiver and the reflecting surface, as shown in Figure 2.4. The reflecting surface can be continuous, based on a parabolic shape, or discrete, consisting of multiple flat surfaces that move independently simulating a parabolic surface overall. Receivers can be linear or point focus, and they are placed in the focus of the parabolic reflecting surfaces. The maximum concentration ratio for a point focus system tied to a 2-axis tracking is 46200, while for a linear focus system with 1-axis tracking it is 215 [3]. This is because 1-axis tracking can balance just one angle and thus it has a non-zero incidence angle even in optimal conditions. Therefore, 2-axis tracking point focus systems have a much higher potential both in terms of efficiency and cost reduction.

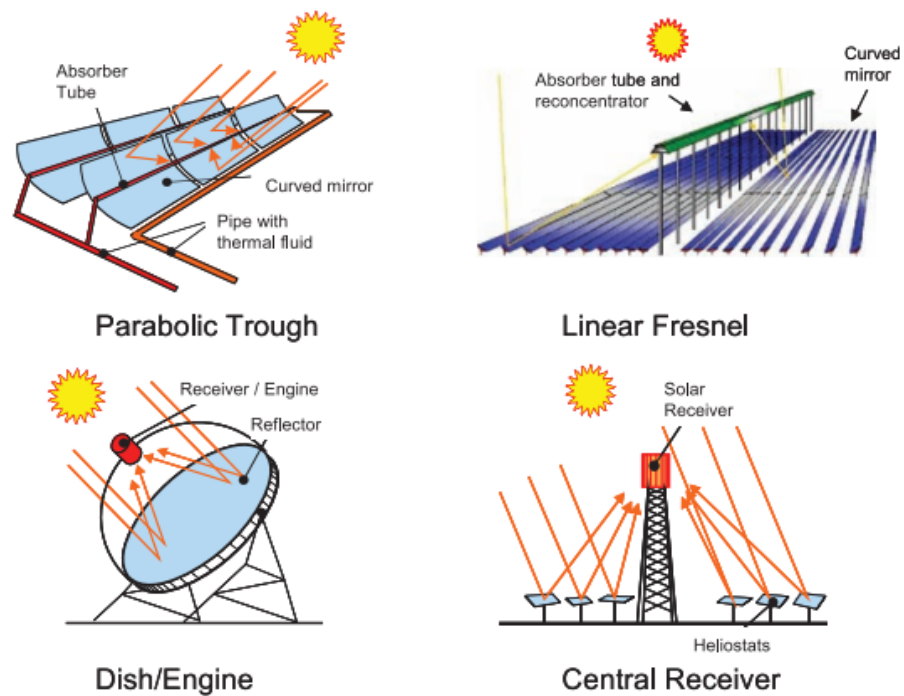


Figure 2.4: Schematic diagrams of the four Solar Thermal Energy systems [21]

2.2.1. Parabolic trough

The parabolic trough system consists of continuous parabolic mirrors of standard size (currently about 6m aperture and 12m length [3]) that reflect the radiation onto a linear absorber, consisting of an outer glass envelope and an absorber tube, separated by a cavity in which vacuum is made to reduce convection heat losses. For such systems, two different tracking strategies are possible.

- North-South tracking: the azimuth angle is balanced while the zenith angle is penalized. This means that the energy production is more balanced over the day and worse in winter, maximizing the yearly production. This strategy is mainly used at low latitudes.
- East-West tracking: the zenith angle is balanced while the azimuth angle is penalized. This means that the energy production is more balanced over the year and worse during the day, providing a much more homogeneous production. This strategy is used at higher latitudes.

The same tracking strategies, as well as the use of synthetic oil as heat transfer fluids, are valid for the Linear Fresnel technology. The intrinsic modularity of this technology is an advantage because it can be scaled up according to the request.

2.2.2. Linear Fresnel

In contrast to the parabolic trough, the linear Fresnel system consists of a series of rectangular ground-based mirrors, forming a discrete surface which reflects the radiation onto a linear absorber with 1-axis tracking. This configuration reduces the wind drag effect on the mirrors allowing the adoption of lighter and cheaper structures. It also minimizes the land occupancy by reducing the shading among the collector rows and reduces the tracking energy consumption since the receiver is fixed and does not move along with the whole structure. Also, using secondary reflectors above the receiver, absent in the parabolic trough technology, higher concentration ratios can be achieved. However, compared to the previous case, the optical efficiency of Fresnel collectors is lower due to the reduced cosine efficiency of the farthest mirrors.

2.2.3. Parabolic dish

The parabolic dish technology consists in continuous parabolic-shaped mirrors with 2-axis tracking. It can reach 31% solar-to-electric efficiency due to the high concentration ratios, much more than other configurations. The power block consists of a Stirling engine, located just behind the receiver. Stirling engines are characterized by with high cycle efficiency for small sizes, opposed to the classical Brayton or Rankine cycles. The development of such technology is mainly limited by cost and reliability. Costs are high due to the absence of a thermal storage system and the geometric limitations on the size of a single dish, resulting in a maximum power output of 25 - 30 kW_{el} with limited economies of scale.

2.2.4. Solar tower

Tower plants with central receivers have a discrete 2-axis tracking system and are referred to as punctual Fresnel systems. The individual reflecting mirrors are called heliostats and approximate a discretized parabola, even if the incidence angle can vary greatly between them. Each heliostat has an independent driver, electric or hydraulic, that allows for its movement. An increase in the tower height reduces the incidence angle, increasing the optical efficiency. However, it also leads to an increase in costs, atmospheric attenuation, and power consumed by the HTF pump to overcome the geodetic head, therefore it is always necessary to investigate this trade-off. In contrast, the impact of its shadow on the heliostats is negligible. This technology enables the use of molten salts as HTF, with 600°C maximum temperature, unlike synthetic oil used in linear collector technologies which reaches 400°C [3]. The significant temperature increase improves the PB efficiency.

2.3. Solar tower components

CSP tower plants consist of several components that enable the progressive conversion of solar radiation into electricity. A solar field reflects the radiation against a receiver, mounted on the top of a tower. From this, a piping system carries the HTF to the storage system. Finally, the storage is connected to a power block that produces electricity and feeds it into the grid. A schematization of CSP tower plants is shown in Figure 2.5.

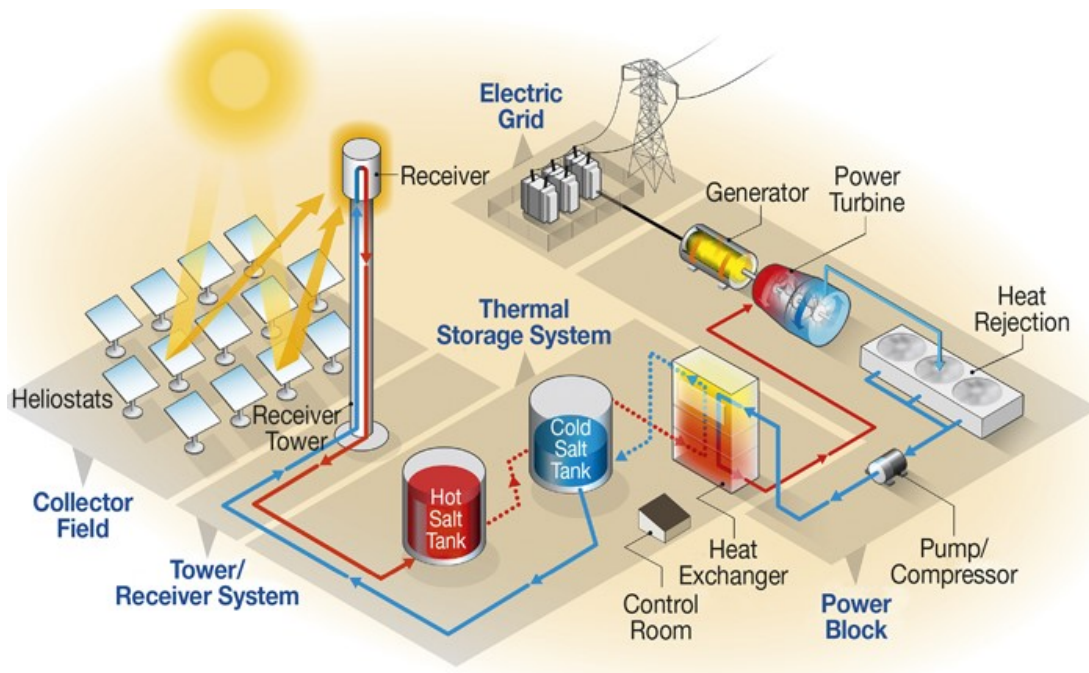


Figure 2.5: Schematization of a CSP tower plant with direct configuration [22]

2.3.1. Heliostat field

The arrangement of heliostats in the field can be polar or surrounded.

Polar fields are mostly used at high latitudes for small or medium size plants. All mirrors are on the same side with respect to the tower, the side that allows maximizing cosine efficiency. They are located north of the tower in the Northern Hemisphere and south of the tower in the Southern Hemisphere. This configuration allows for a more homogeneous power production throughout the year than surrounded fields. An example of the polar field layout is shown in Figure 2.6.



Figure 2.6: PSI 10 and PSI 20 CSP plants, located in Andalusia, Spain [23]

Surrounded fields, on the other hand, are used for larger plants generally at low latitudes. The mirrors surround the tower, and with no space constraints the fields generally have an oval shape reaching up to few km in length on the larger side. There are typically more mirrors on the north side in the Northern Hemisphere and on the south side in the Southern Hemisphere to maximize the optical performance. The mirrors are located around the tower to minimize the land occupied by the field and the average distance from the receiver, while reducing mutual shading. An example of a surrounded field is shown in Figure 2.7.



Figure 2.7: Crescent Dunes CSP plant, located in Nevada, USA [24]

2.3.2. Receiver

The shape of the receiver generally depends on the field layout. In fact, for technologies employing liquid HTF, surrounded fields need external cylindrical receivers, while polar fields can use cavity receivers, which minimize thermal losses, or Billboard receivers, which are simpler and cheaper but not yet adopted in commercial plants. All these receivers, shown in Figure 2.8, are hit by the solar radiation and usually consist of one or two parallel HTF streams flowing within a series of panels. Each panel is made of a manifold that distributes the flow in many parallel side-by-side vertical tubes, whose diameters varies according to the trade-off between heat transfer and pressure losses. Finally, a second manifold on the other end of the panel collects the flow and conveys it to the next panel. To maximize the thermal efficiency, the receiver tubes are covered with a coating material that has high absorptivity and low emissivity, such as Pyromark [25]. In addition, different hydraulic configurations are possible, depending on the thermal balance between flows and pressure losses.

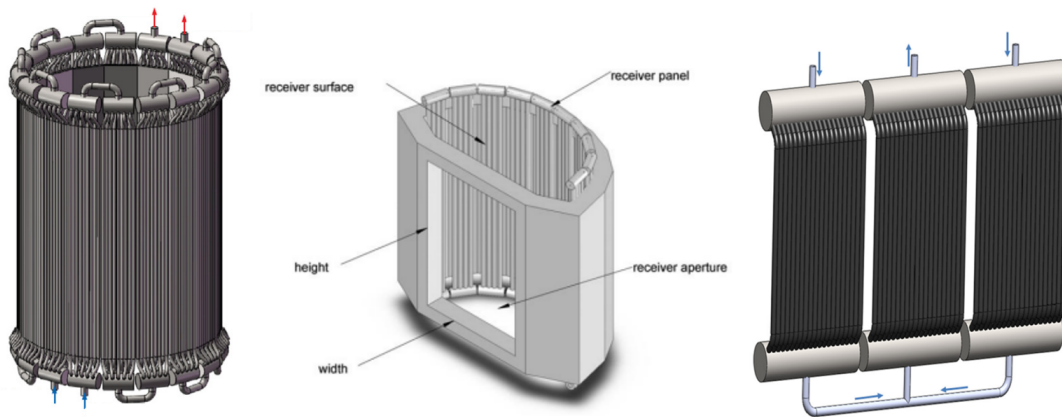


Figure 2.8: Cylindrical (left) [26], cavity (middle) [27], and Billboard (right) [28] receivers

Volumetric receivers are used to heat up air within Integrated Solar Combined Cycles, that integrate methane duct burners to further raise the air temperature.

Finally, falling particle receivers are also under study. Here, a layer of solid particles precipitates from above, is hit by the solar flux and accumulates inside the tower. These solid HTF are usually based on silica sand (SiO_2) or alumina (Al_2O_3), that are stable above 1000°C . Hence, they allow much higher temperatures to be reached, although some issues regarding the displacement and uplift facilities of solid particles still exist.

The use of HTFs other than solar salts, such as liquid sodium in tubular receivers, air in volumetric receivers and solid particles in particle receivers, is studied to increase the

maximum temperature at the power block inlet, allowing for the installation of higher-performance Rankine cycles or even adopting Brayton cycles, combined cycles, or supercritical CO₂ cycles, to increase the electricity generation efficiency.

2.3.3. Tower

Almost all large-scale plants use concrete towers to elevate the receiver, as the one shown in Figure 2.9.



Figure 2.9: Concrete tower in the Cerro Dominador CSP plant, Chile [29]

However, some recently built small-size plants with lower towers employ the steel monopole technology, derived from wind turbines, or steel lattice towers, to reduce costs. In fact, if the plants are not too large, lower towers, lighter receivers, and smaller pipes inside the tower (riser and downcomer) are needed. Therefore, simpler and cheaper solutions already developed in other technological fields are considered. The main technologies that fulfil these needs are the steel lattice, mainly used for telecommunications and electrical transmission, and the steel monopole, largely employed for the wind turbines. However, this is not a novelty since several CSP plants with such towers already exist worldwide, in which some structural and geometrical changes to convert these technologies to CSP application are made.

Some examples of steel lattice tower plants are:

- Vast Solar's modular plant in Jemalong, Australia, with 27m towers [30].

- The Greenway plant in southern Turkey, with a 60m tower [31].
- The SUPCON Delingha 10 MW plant with two 80m towers [32], one of which is shown in Figure 2.10.
- The Ivanpah plant in California (USA), consisting of three independent 140m towers [33].



Figure 2.10: Steel lattice 80m tower in SUPCON Delingha 10 MW plant [32]

As for the steel monopole:

- The Sierra SunTower plant in California (USA) [34], with 55m towers, shown in Figure 2.11.



Figure 2.11: Steel monopole 55m towers in Sierra SunTower plant [35]

- The Sundrop plant in Port Augusta (Australia) [36], with a 127m tower, shown in Figure 2.12.



Figure 2.12: Steel monopole 127m tower in Sundrop plant [37]

The wind industry is now well established in the production of wind turbines reaching considerable heights. Looking at the onshore models on the market with major hub heights among the industry leaders, it can be found:

- Siemens Gamesa SG 6.6-170: hub height = 165m [38].
- Vestas V172-7.2: hub height = 175m [39].
- General Electric Cypress GE-164: hub height = 167m [40].

Thus, the industrial processes for producing steel monopole towers of such heights are more than consolidated, and the need for slightly larger towers to accommodate the riser, the downcomer and the receiver support is not a significant issue from an industrial perspective.

2.3.4. Piping system, HTF, TES

The piping system is used to move the heat transfer fluid from the receiver to the storage. Usually, the HTF consists in solar salts, which chemical composition is $\text{NaNO}_3\text{-KNO}_3$ (0.60-0.40 on a molar basis) [41]. A cold pipeline is used to carry the salts from the

storage to the receiver, while a hot pipeline flanking the previous one takes the reverse route. The goal of the piping system is to transfer as much HTF as possible while minimizing thermal losses, pressure losses, and costs. In addition, the plant configuration can be direct or indirect, as shown in Figure 2.13.

In the direct configuration, the HTF coincides with the storage media, which is the fluid stored inside the storage system's tanks. In this case there is only one heat exchanger between the HTF and the power block. Such configuration is generally adopted in salts-based plants.

Alternatively, in the indirect configuration, the HTF and the storage media do not coincide and two heat exchangers are installed, the first between the HTF and the storage media and the second between the HTF and the power block. This configuration is adopted in the case where the HTF cannot be stored for cost reasons or because of its physical properties. In this case, an additional heat exchanger increasing costs and reducing the power block's inlet temperature is necessary.

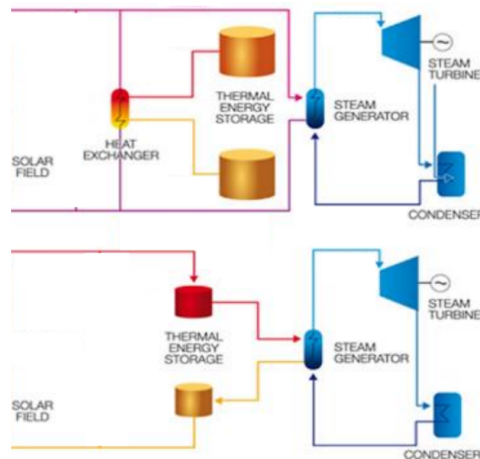


Figure 2.13: Indirect (up) and direct (down) configurations of CSP plants [42]

The Thermal Energy Storage (TES) generally has two tanks, one for the hot fluid (565°C for solar salts), that is filled during the day and emptied during the night, and one for the cold fluid (290°C for solar salts) that performs the opposite cycle. An alternative TES solution is the Thermocline (Figure 2.14), which is a single tank with a temperature gradient inside that keeps the high-temperature fluid in the upper region and the low-temperature fluid in the lower one thanks to a density difference. This configuration eliminates the cost of two tanks but penalizes the energy conversion due to the temperature variation over time, which reduces the amount of energy stored. For this reason, the thermocline solution is not used in large-scale CSP plants.

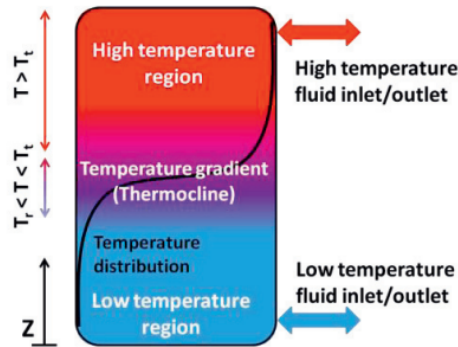


Figure 2.14: Schematization of a thermocline storage system [43]

Finally, it is also possible to build plants without any storage system, but this reduces the convenience and cancels the dispatchability advantage over PV.

2.3.5. Power block

The most diffused power block (PB) for CSP tower applications is the subcritical steam Rankine cycle, which provides good efficiency and reliability at acceptable costs. However, the upper limit dictated by both temperature (565°C with solar salts) and size (usually tower plants do not exceed 110 MW_{el}) severely limits the possibility of increasing the electric efficiency and achieving significant economies of scale. These limitations also preclude supercritical cycles and 2 reheats, which would both bring efficiency benefits. This is usually done, indeed, for cycles around 500 MW_{el} , well beyond the current size of CSP tower plants [3]. In addition, the cycle's condenser is often air-cooled, due to the scarcity of water in the locations where such plants are built, providing worse heat transfer properties and adding the fans' consumption to the auxiliary losses. The current net electric efficiency of such Rankine cycles for CSP application is around 40-42%.

An interesting alternative consists of supercritical CO_2 cycles. Carbon dioxide is much less corrosive than steam and allows for higher temperatures to be reached with a minimal consumption in the compression phase, which takes place in the region near the CO_2 critical point ($T_c = 30.98^{\circ}\text{C}$, $p_c = 73.77\text{bar}$). Also due to the convenience of adding a recuperator at the turbine outlet, the net electric efficiencies can reach 48%. Another advantage of sCO_2 cycles is the compactness of all PB components compared to Rankine ones, which leads to a cost reduction. A multitude of cycle configurations that would allow the efficiency to be further increased is under study.

2.4. State of the art

The state of the art of CSP technology consists in 50-100 MW_{el} tower plants in low-latitude arid or even desert locations. Typically, the plants have surrounding heliostat fields with oval shape and external cylindrical receivers placed on top of concrete towers. The heat transfer fluid consists of solar salts, which also serve as storage media in the two tanks of the sensible thermal energy storage. Hence, these plants have direct configuration, and the operating temperatures range from 290°C to 565°C. Lastly, the power block consists in subcritical steam Rankine cycles with 1 reheat and typically with air-cooled condensers. The main issues are due to the Rankine cycle, because the power output is limited by the field optical efficiency, and the cycle efficiency is limited in turn by the low HTF maximum temperature and the small power block size. Moreover, the high freezing temperature of solar salts is another limit. Finally, these plants have massive capital expenditures and long construction times.

2.5. Research trends

The improvements being studied on CSP are different and concern the solar field, the receiver, the heat transfer fluid, and the power block, for which the most promising solution consists in sCO₂ cycles.

The use of HTFs that allow the achievement of higher temperatures and thus higher power block efficiency is one of the most studied trends, particularly with regards to liquid sodium, air, and solid particles. A liquid sodium pilot plant built by Vast Solar is already operational in Jemalong, New South Wales, Australia [30]. It is a 1.1 MW_{el} modular plant in which sodium is used as both HTF and storage media, with a storage capacity of 3h. Another benefit of sodium, besides the higher maximum temperature, is the reduction of trace heating losses due to its lower freezing temperature (97.7°C versus 220°C for solar salts) [44]. [45] establishes that a temperature increase up to 600°C and 640°C achieved by salts with high-performance composition does not bring significant benefits compared to the reference case at 565°C, due to the contextual increase in costs. Finally, [46] proposes an interesting solution consisting in a multi-tower solar-only combined cycle with olivine particles as HTF in an up-flow fluidized-bed cavity receiver. Although this solution improves the optical and thermal performance and increases the cycle's inlet temperature, it shows a 5% loss in the particle path while large costs of particle transport subsystems, like conveyors and bucket elevators, are expected. Therefore, it is concluded that, within modular systems, solid particle HTFs are not attractive.

Regarding the receiver, an interesting study in [47] analyses the performance of a new configuration for small-scale plants, namely a 10 MW_{th} tubed volumetric cavity receiver suitable for molten salts. This configuration, states the author, could be used effectively within modular plants with many fields connected to a single TES and PB to take advantage of their economies of scale. The results indicate that such configuration would achieve 90% thermal efficiency and drastically reduce the peak metal temperature on the outer surface of the tubes.

Another interesting solution consists of Decoupled Solar Combined Cycles (DSCC) where a multi-tower solar field with air receivers and small Brayton cycles at the top of each tower deliver the exhaust heat to a single TES and Rankine bottoming cycle by an HTF. The study of such a configuration in [48] results in a reduction of the Levelized Cost of Electricity (LCOE) between 24.75% and 31% compared to a conventional CSP plant. In contrast, [49] states that the increased complexity of the plant scheme can just outweigh the increased costs, while the LCOE has little sensitivity to the number of towers.

A possibility for small-scale plants consists of small polar fields that convey the radiation into liquid sodium cavity receivers, with a TES located above the tower employing a phase change material as storage media. The TES on the tower is just below a Stirling engine. Such a configuration is called STEALS (Solar Thermal to Electricity via Advanced Latent heat Storage) and is discussed in [50] and [51]. The results indicate a lower LCOE than conventional CSP plants and higher optical and thermal efficiency, even if the power block efficiency is low due to the small size.

An innovative solution from a solar field perspective consists in a surrounding heliostat field with two towers aligned on the East-West axis. It can also be seen as two oval-shaped surrounding fields, each with one tower, having an intersection region in the middle. The heliostats in such region technically belong to both fields and can alternately point to the receiver that maximizes the optical performance at a given time instant or on an annual basis, considering the effects of shading and blocking due to the different orientations between neighbouring heliostats. An example of this solution is shown in Figure 2.15. The comparison is made with a conventional single-tower system of equivalent power and the optimized parameters are: field layout, tower height, receiver size, distance between towers (thus the degree of intersection of the fields), and number of towers.

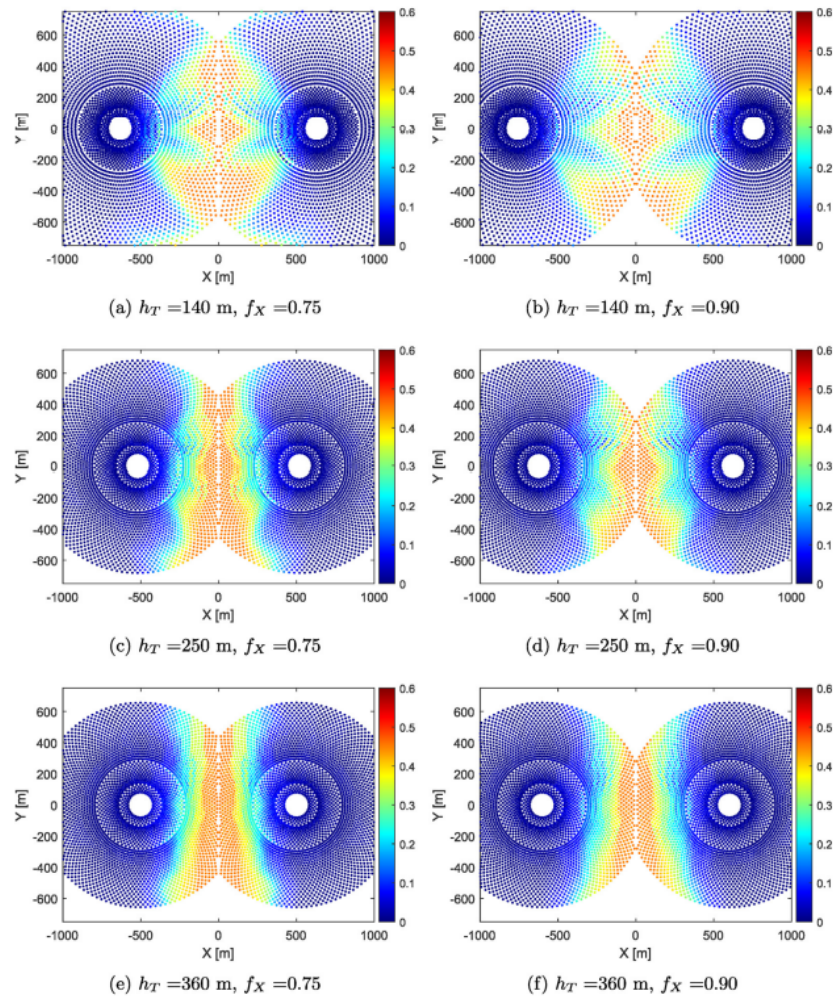


Figure 2.15: Fraction of annual DNI-weighted energy reflected by every heliostat to the adjacent field's central receiver during the daylight hours over the year. h_T is the tower height and f_X is the relative distance between the towers [52]

The results vary depending on the study and the assumptions, as well as the size of the plant under analysis. [53] indicates an optical efficiency increase associated to a significant increase in the LCOE due to the additional costs of a second tower and receiver. In contrast, [54] finds an increase in the annual optical efficiency equal to just 0.26% between a multi-tower field and 2 single tower fields of equivalent size. [55] indicates that a merged field with two towers would lead to an optical gain of 5-8% when compared to a single tower field of equivalent size, but only a 1% increase when compared to 2 single tower fields whose total power is equivalent. In [52] the comparison between a dual-tower field and an equivalent single-tower field shows an increase in the annual optical efficiency of 1.5% in favour of the dual-tower case. [56], which considers the addition of the second tower South of the first rather than on the East-West axis, reports a 3.64% increase in

the annual optical efficiency for 50 MW_{th} associated to a higher Levelized Cost of Heat (LCOH), which indicates that adding an extra tower and receiver is not convenient. The same study also reports that, above 400 MW_{th}, the multi-tower solution provides a more advantageous LCOH than the single-tower analogue.

Overall, this solution brings modest optical benefits, which are partially or totally compensated by the increased costs for additional towers and receivers. In particular, the optical benefits are most pronounced when comparing a merged dual-tower system with a single conventional system of equivalent power, while they are almost negligible when comparing the same dual-tower system with two single-tower systems whose total powers are equivalent. Finally, the increase in the control system's complexity and in the tracking consumption for heliostats with multi-aiming strategy should also be considered. Hence, it is decided not to proceed with the multi-tower merged-fields analysis in this thesis, but to analyse the modular case with multiple solar fields and no heliostats in common.

2.6. Modular technology

An interesting CSP innovation is the realization of modular tower plants, with multiple independent solar fields connected by a branched piping system to a centralized thermal energy storage and power block.

2.6.1. Literature review and existing plants

The few studies in literature on CSP tower plants' modularity are quite discordant.

For example, [45] compares a conventional central tower plant and a modular plant with 5 towers, both with a total capacity of 125 MW_{el}. The study concludes that the multi-tower plant leads to a distinctly higher LCOE than the conventional one despite achieving higher efficiencies. It is stated that this is mainly due to the higher costs for receivers and piping system. It is also remarked that even with an increase in atmospheric attenuation, which should favour modular plants, the conventional case has a 5% lower LCOE.

In another study [57], a comparison is made between a conventional central tower plant and 3 different modular plants with 3, 4, and 5 towers for the same total capacity of 150 MW_{el}. It results that the solar-to-electric efficiency increases with the number of towers, thus reducing the size of each module, and that the plant's output is more balanced between summer and winter. Finally, the multi-tower approach is claimed to reduce the plant's cost up to 10%.

Some examples of modular plants already exist worldwide, despite being very small in

size.

The Jemalong pilot plant (New South Wales, Australia) [30] built by Vast Solar [58] and completed in 2018 (Figure 2.16), consists of 5 rectangular polar modules of 1.2 MW_{th} each to produce 1.1 MW_{el} with a 3h storage. The HTF is liquid sodium, while the five 27m towers are steel lattice and receivers are cavity type.



Figure 2.16: Jemalong modular pilot plant by Vast Solar [58]

The Sierra Sun Tower plant (California, USA) [34] built by eSolar [59], was completed in 2010 and ended the commercial operations in 2015. It is depicted in Figure 2.17 and consists of 4 rectangular modules to produce a total of 5 MW_{el} without storage. The HTF employed is water while the two 55m towers are steel monopole, and the receivers are dual cavity type. The power block consists of a Rankine cycle.



Figure 2.17: Sierra Sun Tower modular plant by eSolar [60]

2.6.2. Advantages

A CSP modular configuration brings many advantages along with some drawbacks, compared to the traditional configuration with a single field and one tower.

First, because of the optical efficiency increase due to the compactness of modules, a modular plant allows for the lowering of capital expenditures (CAPEX) and operating expenditures (OPEX) of the heliostat field.

Then, thanks to modularity, it is possible to remove the power limit which is currently around 110 MW_{el} due to the subsequent decay in optical performances, allowing the centralized TES and PB to scale up. This is reflected in greater economies of scale for these components and increased electric efficiency of the power block due to the larger size, as well as in the possibility of using more efficient PB configurations such as adding a second reheat or a supercritical heating, which are currently absent in PBs for CSP application.

Modularity also reduces installation complexity, technical challenges, and building time due to the standardization of design and components and the installation in parallel. It also offers flexibility of operation, since it is not necessary to wait for the completion of all modules to start the plant, and increased plant's availability in case of maintenance, since it is possible to stop only some modules rather than the whole plant.

Then, smaller modular fields imply smaller heliostats, which suffer less from the wind drag effect and can be built with lighter and cheaper structures. The multitude of towers provides mutual wind shielding while the lower height results in a lower wind velocity on the receiver, reducing its thermal losses by forced convection and allowing the tower construction with cheaper technologies than concrete. The main alternatives are steel monopole or steel trusses.

As for the receiver, the reduced amount of metal related to its small size, and hence to the smaller diameter of its tubes, allows for a lower thermal inertia and thus a more effective and localized control.

From the land consumption perspective, the modular layout also brings advantages. Thanks to both the increase in the optical efficiency, the possibility to design rectangular or square modules minimizing the empty spaces, and the reduced distance between consecutive rows of heliostats, more compact installations can be obtained, extending CSP plants even to locations with stricter space limitations.

Finally, many small fields with many towers, rather than a single field with a taller tower, reduce the air flux zone, lowering the risks for the local fauna and the aviation sector.

2.6.3. Disadvantages

The main drawbacks of modular plants consist in the increase in the number of towers and receivers to be purchased. This could take advantage of economies of scale for the higher number of pieces, but no longer economies of scale on the individual components' size are possible, especially for the receiver, leading to higher CAPEXs and OPEXs.

In addition, many drawbacks are related to the piping system. In fact, the piping in conventional plants is very simple since it only runs inside the tower and few meters on the ground to the TES at its base. In contrast, such system is necessarily branched in modular plants since it must convey the HTF from each tower to the centralized TES, implying piping lengths even in the order of km for large-scale plants, similarly to what happens in parabolic trough plants. The main drawbacks of the piping system are therefore thermal, pressure and economic.

The piping's thermal efficiency for a modular plant is lower than the conventional one because of the larger exchanging surface of pipes and the non-isothermal mixings at the junctions in the hot HTF path.

Piping pressure losses are greater than in single fields due to the increase in both distributed losses (total length) and concentrated losses (greater number of joints and el-

bows). However, in modular configurations, the receiver pressure losses are lower due to the smaller size, thus the trade-off on pressure losses needs to be investigated further.

Finally, the CAPEXs and OPEXs of a modular plant's piping system are significantly higher because of the greater amount of materials (steel, insulations) and number of expansion loops, valves, and supports (in the frequent case where pipes are elevated above the ground). In addition, the larger electric trace heating system, necessary to prevent the freezing of salts within the piping, leads to a growth in both the auxiliary consumption and costs.

In Table 2.1, a summary of the advantages and drawbacks of modular plants is reported.

Advantages of modular plants	Disadvantages of modular plants
<p>Higher $\eta_{optical}$: lower SF Capex, Opex Higher P_{max}: econ. of scale TES, PB Improved PB layouts Reduced complexity & building time Larger availability Reduced wind drag effect on heliostats Lower receiver convective losses Lower receiver pressure losses Small towers: cheaper technologies Small receivers: lower thermal inertia Reduced land consumption Smaller air flux zone</p>	<p>More receivers: higher Capex, Opex Larger piping: higher Capex, Opex Higher piping thermal losses Higher piping pressure losses More towers Larger trace heating system</p>

Table 2.1: Advantages and disadvantages of modular plants over conventional plants

3 | Methodology

The purpose of this thesis is the techno-economic analysis and optimization of large-scale modular plants, to evaluate the main trade-offs between costs and benefits, and to define the possible cost-effectiveness of these plants compared to their centralized counterparts. To proceed with the analysis, accurate models of each component, and a generalized bottom-up methodology that defines the design and the optimizations to carry out the comparisons, are required.

The development of thermodynamic models for the major components is necessary to derive their performances both under optimal conditions and on an annual basis. In addition, such models provide useful parameters for estimating costs. The model of each component is developed using a specific software and must be generic and flexible with respect to the inputs. The wider the range of cases that can be analysed, the more effective the model is. Moreover, a model must provide outputs with as little error as possible in reasonable computational times, even though these requirements are often in opposition. In the present study, 3 different software packages are used to analyse the major components: SolarPILOT [61] to model the solar field, Matlab [62] for receiver and piping models, and Thermoflex [63] for power block models.

The components can be optimized either individually or considering the whole plant. Sometimes the configuration obtained from the optimization of a single component may not coincide with the result of the overall plant's optimization. In this eventuality, the optimal solution for the plant must be preferred since the goal is to minimize the LCOE, which includes the effect of all components together. Moreover, unlike conventional plants, modular plants have an additional complexity due to the different possibilities in layout, geometry and technology employed by individual modules, and the greater extent and complexity of the piping system.

Two procedures for designing modular plants are possible. The top-down approach starts with a conventional plant of given power and breaks it down into a different number of modules. In contrast, in the bottom-up case, a variety of modules' configurations are analysed, and the optimal ones are used in the plant design. In this thesis, the bottom-up

approach is preferred because, although it implies a larger number of cases, it allows for more generic results, as they are independent of the starting plant's size. A schematic of the methodology is reported in Figure 3.1. Starting from the climatic and geometric conditions of each module, the solar field is first generated, and the results in terms of power delivered to the receiver are used as inputs to run the receiver models. Having applied this procedure to all modules, the minimum LCOH ones are selected, and their number and geometry are used to run the piping model. Then, the power block model is also applied, completing the analysis and allowing for the LCOE evaluation of the few remaining options. Finally, the least-LCOE or the most compact plant is selected.

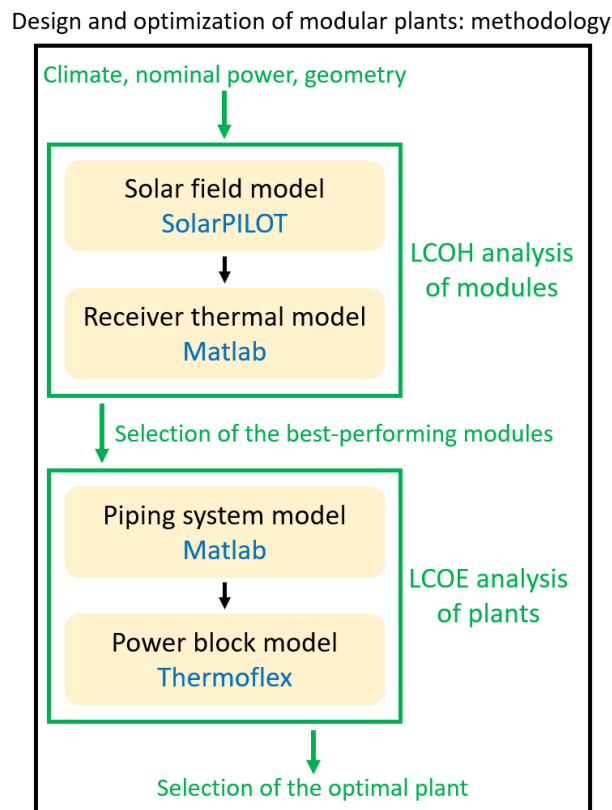


Figure 3.1: Schematic of the methodology

3.1. Solar field model

The solar field model is derived from SolarPILOT. This is an open-source software provided by NREL (National Renewable Energy Laboratory [64]), the Solar Power Tower Integrated Layout and Optimization Tool (SolarPILOT). The solar field model is needed to obtain the field's design layout and the annual operation, providing the heat flux on the receiver's surface to be used on an hourly basis in the receiver thermal model. The main inputs and outputs are listed in Table 3.1.

Input sections	Outputs
Climate	Field layout
Layout setup	Heat flux on receiver surface
Heliostats properties	Detailed optical efficiencies
Receiver properties	Power absorbed by the receiver
Performance simulation setup	Number of heliostats

Table 3.1: Input sections and main outputs of the solar field model on SolarPILOT

Starting from the "climate" section, it is possible to import the climatic files of many locations present in the software library, or alternatively new ones can be created through specific websites such as [65]. Such files contain a Typical Meteorological Year with the annual DNI and dry ambient temperature on an hourly basis, as well as several other parameters. It is necessary that the plant location is defined in terms of the latitude, longitude, elevation, and time zone so that the sun position can be evaluated correctly.

It is also needed to set the atmospheric conditions. In this thesis, the default "limb-darkened sun" model is chosen as the sun shape model, which specifies the sun intensity as a function of the angular distance from the centroid of the sun disc:

$$\Phi(\theta) = 1 - 0.5138 \cdot (\theta/0.00465)^4$$

Where θ is the displacement angle from the centroid of the solar disc and $\Phi(\theta)$ is the intensity profile of the sun as a function of the displacement angle.

The "weather file data" is used as insolation model, determining the DNI intensity and other weather values, because it accounts for the site-specific weather variability and local weather trends throughout the year, thus it is the best to determine the optimal layout for sites with asymmetric daily insolation profiles.

Finally, with regard to the atmospheric attenuation model, which determines the fraction of energy that is lost from each heliostat to the receiver by atmospheric scattering (the distance between them is defined as slant range), the default settings for both a typical clear day and a typical hazy day are used: the curves are implemented as the "DELSOL3 Clear Day" and "DELSOL3 Hazy Day," respectively, and are depicted in Figure 3.2. The visibility is defined as the maximum horizontal distance through the atmosphere at which objects can be seen by an unaided eye.

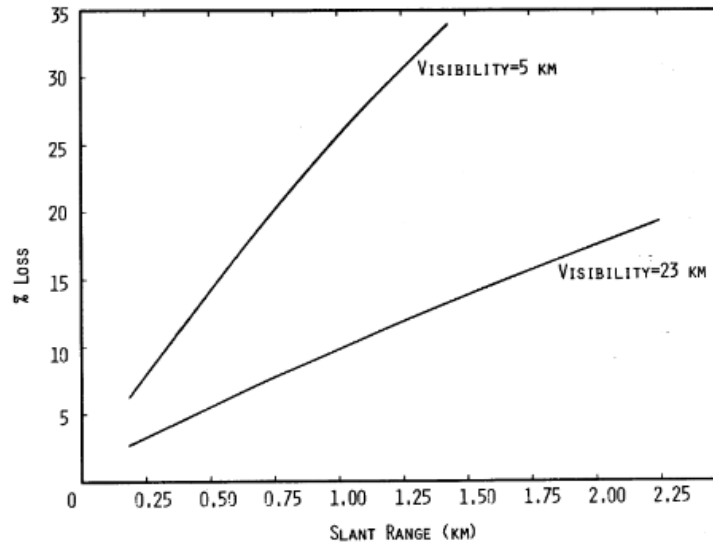


Figure 3.2: Trend of the attenuation losses as a function of the slant range for DELSOL clear and hazy day models [61]

The "layout setup" section allows to define all the parameters that affect the positioning of individual heliostats with respect to the tower. The procedure followed by SolarPILOT consists of filling the entire space within the defined land boundaries with heliostats and then removing them progressively, starting from those with the lowest optical efficiency, until the design power is reached. For the heliostat selection criteria, the "power-to-receiver" principle is chosen since it is recommended by SolarPILOT, ranking the heliostats with a set of representative profiles in which 4 days with a 2-hour frequency selected by the software are simulated throughout the year. This procedure results in a good compromise between accuracy of results and computational time. Other selection criteria for the heliostats are based on the optical efficiency items or depend on the electricity selling price. However, these strategies do not maximise the power delivered by each heliostat, thus they do not allow for the minimization of costs.

The solar field design power is the desired thermal power provided by the heliostat field on the outer surface of the receiver. The design-point DNI value is chosen as the maximum DNI at the plant location or can be computed as the DNI that is overcome just for a certain small fraction of hours over the year, and does not exceed 1000 W/m^2 because of what already explained about the solar resource. The sun location at design point is the condition under which the plant is designed. In the present study, summer solstice (the condition of maximum plant productivity) is chosen to maximize the annual energy production. Note that in SolarPILOT, summer solstice always refers to June 21st, as well as winter solstice to December 21st. Thus, for plants located in the Southern Hemisphere,

it is necessary to set winter solstice (December 21st) to make a summer sizing. The sizing at the spring or fall equinox, instead, leads to a less extreme design that reduces total costs, but does not allow for the full exploitation of the solar resource in summer, leading to a consistent defocusing of mirrors and a lower annual electricity production.

Regarding field boundaries, a minimum and a maximum field radius can be set as the distance from the tower. The minimum radius affects the design in a significant way because it determines the amount of high optical performance mirrors located close to the tower. Finally, it is possible to enter Cartesian coordinates of regions in which to place or from which to exclude heliostats, in case of space constraints or if a certain field shape is to be imposed.

From the same section it is also possible to set the tower height and the field layout method, which is generally Radial Stagger or Cornfield.

The radial stagger layout method is suitable for surrounding fields and consists of arranging the rows of heliostats alternately along iso-azimuth lines with constant radii, as shown in Figure 3.3. The initial distance between heliostats in a row is determined by the azimuth spacing factor. As rows are added radially, the distance between neighbouring heliostats in the same radial row increases. When the ratio of the current absolute distance to the original one exceeds the azimuthal spacing reset limit, the spacing is restored to the original distance. The spacing between rows in radial direction is a function of the row radius. The two main radial spacing methods offered by SolarPILOT (algorithms for calculating inter-row spacing) are Eliminate Blocking and No Blocking Dense.

The Eliminate Blocking option attempts to radially space the rows so that heliostats along an iso-azimuth lines do not block reflected light from reaching the receiver. As the radial position of the rows increases, the elevation angle of the receiver decreases and the distance between rows must increase to avoid blocking. This is between alternate rows since each intermediate row is azimuthally offset and does not contribute to blocking.

The No Blocking-dense method, adopted in this study, is a variant of the Eliminate Blocking. Heliostats close to the tower are limited in radial spacing by the collision radius instead of the blocking distance, thus the entire heliostat is in full view of the receiver and cannot be blocked by closer rows. Under this circumstance, heliostats can be arranged closely, without regard to heliostats in adjacent rows [61].

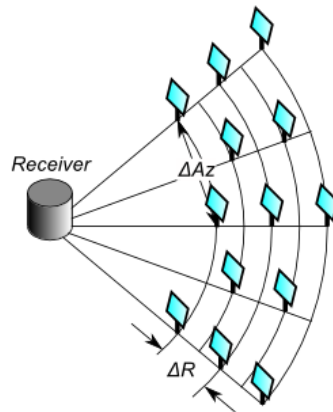


Figure 3.3: Radial stagger layout method [61]

The cornfield layout method, shown in Figure 3.4, is often used in small polar fields and allows heliostats to be aligned in straight rows, typically along Cartesian axes. SolarPILOT allows the spacing to be specified on both East-West (X) and North-South (Y) axes. The distances between heliostats in the X and Y directions are given by the product of the heliostat width and the spacing factors.

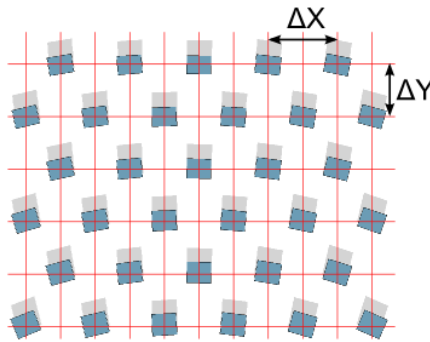


Figure 3.4: Cornfield layout method [61]

In the "heliostats" section all the parameters involved in the heliostat design are defined, namely size, number and arrangement of panels if they are made with multiple mirrors, focusing type on the receiver, optical error parameters and mirror performance parameters. Concerning the latter, the reflective surface ratio is the ratio of the active reflective area to the total structural area. The mirror reflectivity is considered in a clean state and affects the optical performance. The soiling factor represents the fraction of reflected light after considering the dirtiness of the surface, so it depends on the local conditions and affects the overall mirror reflectivity.

The "receiver" section allows to determine the geometry (external cylindrical or flat plate), dimensions, acceptance and orientation angles, placement, and coefficients for receiver losses. About the thermal losses, these are set to zero within SolarPILOT since they are calculated more accurately through the models developed on Matlab.

In the "simulations" section, it is possible to get the layout of the solar field along with its performance under a given condition, as well as to perform parametric analyses. The performance simulation is employed to evaluate the system's design conditions.

The heliostat aim point method allows to set the pointing strategy, which is implemented to reduce the peak incident flux on the receiver surface by maximizing the average flux. These methods affect the optical efficiency due to spillage losses, representing a compromise between receiver flux distribution and optical efficiency loss. The image of a mirror is the 2D surface on a target that is hit by its reflected rays: this surface has not the same size as the mirror, but it enlarges with the distance from the target. The image size priority aiming method, chosen for the present study, is implemented for both flat-plate and cylindrical receivers. This method determines the aiming position of heliostats by sequentially placing their images on the receiver at the lowest flux points. The order of image placement is determined by the size of the image as it appears on the receiver. Therefore, images with significant distortions at larger distances are placed first. After each placement, a local minimum in flux intensity is identified and the subsequent heliostats are placed in that location. The aiming points are placed within a region offset from the receiver edges equal to the product of the standard deviation of the image size and the positioning cut-off factor. As the image size or the cut-off factor increase, the allowed positioning region narrows. Compared to other methods, the image size priority provides a more homogeneous distribution of the images while respecting the heat flux constraint.

The flux simulation model specifies the engine used to evaluate the system's performance. The Hermite analytical model is employed. This estimates the distribution of light reflected from each heliostat using a modified Gaussian equation and a truncated polynomial expansion of the Hermite series [61].

The flux grid resolution parameters specify the number of flux intensity evaluation positions in the horizontal and vertical dimensions of the receiver. As the number increases, the resolution of the flux evaluation grows. A value of 100 flux nodes in both horizontal and vertical directions, necessary to run the receiver model with sufficient accuracy, is set.

Finally, the "results" section allows the layout of the solar array to be displayed with the optical efficiencies of each individual heliostat, as well as the heat flux map on the

outer surface of the receiver, which provides the peak flux value. There is also a system summary with the key outputs related to the system design and performances, with a special emphasis on the optical losses.

3.1.1. Optical efficiency

The optical efficiency of solar tower systems is expressed by the ratio of the power reaching the receiver's outer surface to the net power delivered by the sun over the mirrors:

$$\eta_{opt} = \frac{Q_{rec}}{DNI \cdot n_{hel} \cdot A_{hel}} = \rho_{hel} \cdot \eta_{cos} \cdot \eta_{shad} \cdot \eta_{block} \cdot \eta_{att} \cdot \eta_{int}$$

- ρ_{hel} is the mirror reflectivity after including the effect of the soiling factor.
- η_{cos} is the cosine efficiency, which is the ratio of actual power delivered by heliostats to the receiver to the maximum power it could deliver if the incidence angle was zero, and it is an average value of all heliostats in the field. An example is shown in Figure 3.5. This is one of the main optical loss contributions and it is the reason why in surrounding fields more mirrors are placed to the north of the tower for systems located in the northern hemisphere. The value mainly depends on the mutual position between each heliostat and the tower, the tower height, and the sun position.

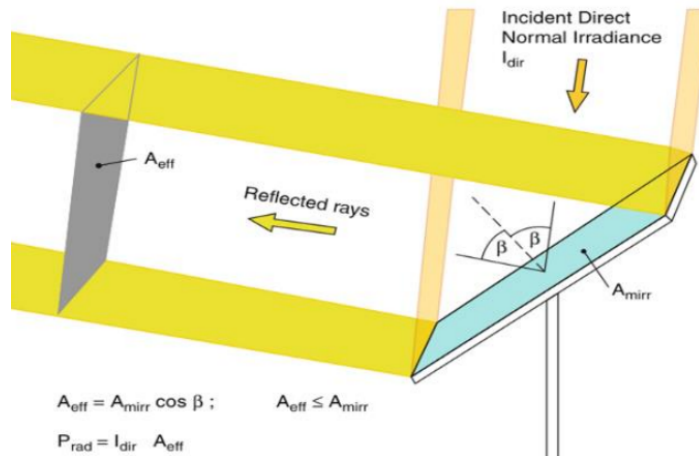


Figure 3.5: Cosine loss mechanism [66]

- η_{shad} is the shading efficiency and represents the proportion of power lost due to heliostats casting shadows on neighbours, preventing the radiation from reaching a portion of them. This value depends only on the layout method and the sun position.

- η_{block} is blocking efficiency and accounts for the power loss due to light that is reflected from heliostats onto the back of adjacent ones, without reaching the receiver. It only depends on the layout method and the sun position.
- η_{att} is the attenuation efficiency and considers the effect of atmospheric attenuation in the transmission of reflected light due to the distance between heliostats and receiver. Attenuation is caused by atmospheric scattering, in which light interacts with water vapor, dust, or other particulate matter and is reflected, refracted, or absorbed. This value depends on the distance between each heliostat and receiver, and on the local atmospheric conditions.
- η_{int} is the image intercept efficiency (or spillage efficiency) and happens because the images widen with distance from the focal point and thus may fail to intercept the receiver aperture. Light that strikes non-absorbing surfaces such as oven boxes, refractory walls, or the tower structure, or light that misses the receiver entirely is accounted for. This value depends on the size of heliostats and receiver, their relative distance, the aiming strategy, and the heliostats' optical error parameters.

3.1.2. Off-design

The off-design of the solar field is evaluated through optical efficiency maps as a function of the sun position. In particular, the field optical efficiency is calculated for specific values of azimuth angle and elevation angle, that is also called solar altitude angle and is equal to $90^\circ - \text{zenith angle}$. From these, a matrix is obtained and interpolated in two dimensions to ensure that the optical performance can be derived under every condition. Figure 3.6 shows the angles needed to describe the sun position.

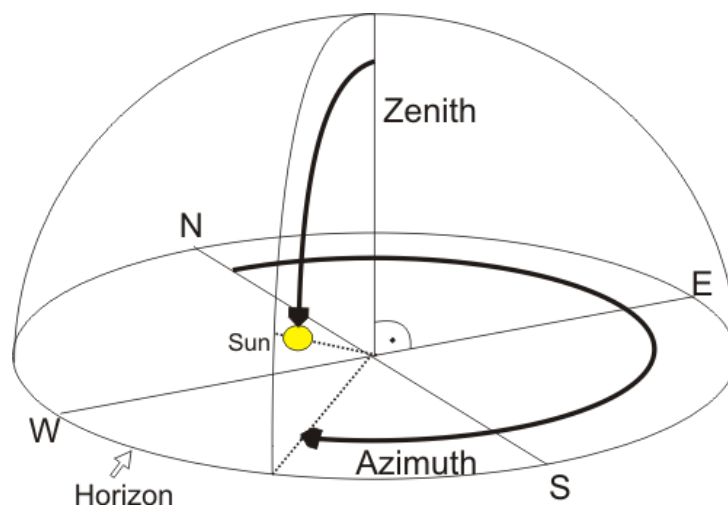


Figure 3.6: Azimuth angle and Zenith angle [67]

Having the matrix, it is necessary to calculate the angles that determine the sun position for each hour of the year at a specific location, knowing latitude, longitude, and Standard Time Zone (STZ). The zenith angle (θ_Z) is derived from:

$$\cos \theta_Z = \sin \delta \cdot \sin \Phi_{LAT} + \cos \delta \cdot \cos \Phi_{LAT} \cdot \cos \omega = \sin \alpha_S$$

While the azimuth angle (γ_S) from:

$$\cos \gamma_S = \frac{\sin \alpha_S \cdot \sin \Phi_{LAT} - \sin \delta}{\cos \alpha_S \cdot \cos \Phi_{LAT}} \cdot \text{sign}(\Phi_{LAT}) + 180^\circ$$

Where α_S is the solar elevation, ϕ_{LAT} is the plant's latitude, δ is the declination angle and ω is the hour angle. The declination angle is the angle between the equator and the straight line connecting the centre of the Earth to the centre of the Sun. This angle varies seasonally and is calculated by the equation:

$$\delta = 23.45^\circ \cdot \sin \frac{360 \cdot (n + 284)}{365}$$

Where 23.45° is the inclination of the Earth's equatorial plane with respect to the ecliptic plane of its orbit around the sun, n is the day number in the year starting from January 1st = 1, and the sine argument is expressed in degrees.

The hour angle is the angle between the meridian where the plant is located and the meridian whose plane contains the sun: it is zero at solar noon and increases by 15° every hour:

$$\omega = 15^\circ \cdot (t_S[h] - 12)$$

Where t_S is the solar time, which differs from the local clock time because it indicates 12:00 when the azimuth is exactly 180° . This difference is because the local clock time refers to the reference meridian for the specific STZ, as well as due to the variation in the Earth's rotational speed during the year because of the orbit's eccentricity and the ecliptic's obliquity. The equation to calculate the solar time is:

$$t_S [h] = t + \frac{(\Phi_{LONG} - \Phi_{STD})}{15^\circ} + \frac{E_n}{60}$$

Where Φ_{LONG} is the longitude of the plant and Φ_{STD} is the longitude of the STZ reference meridian obtained from:

$$\Phi_{STD} = STZ \cdot 15^\circ$$

Since there are 24 time zones along the Earth's circumference, therefore $360^\circ/24 = 15^\circ$. Finally, E_n is a correction factor obtained from the "equation of time":

$$E_n = 229.18 \cdot \left(0.000075 + 0.001868 \cdot \cos \left(360 \cdot \frac{n-1}{365} \right) - 0.03277 \cdot \sin \left(360 \cdot \frac{n-1}{365} \right) - 0.014615 \cdot \cos \left(2 \cdot 360 \cdot \frac{n-1}{365} \right) - 0.04080 \cdot \sin \left(2 \cdot 360 \cdot \frac{n-1}{365} \right) \right)$$

Where the arguments of trigonometric functions are expressed in degrees and n is the day number in the year.

3.2. Receiver thermal model

The receiver model is based on the thermal model for external cylindrical receivers described in [68]. This is a 2D model entirely developed in Matlab and allows the sizing and evaluation of thermal and pressure losses of both external cylindrical and Billboard receivers through their breakdown into flows, panels, and tubes, starting from the heat flux maps obtained from SolarPILOT. Tubular receivers are composed of panels in series arranged in one or more flow paths, and each panel consists of many tubes in parallel mounted vertically to minimize the mechanical bending stresses due to their own weight. To maximize the absorption of the incident solar radiation, the tubes are coated with a high-absorptivity paint. The hydraulic circuit is designed accounting for the flux distribution: in the hottest part of the receiver, on the north side in the northern hemisphere, the coldest fluid flows in a co-current configuration to decrease tubes' mechanical stress and to avoid the overheating of the HTF. The maximum temperature at which the receiver can operate is constrained by the receiver's material and the HTF boiling point. An example of the flux asymmetry in cylindrical receivers is shown in Figure 3.7.

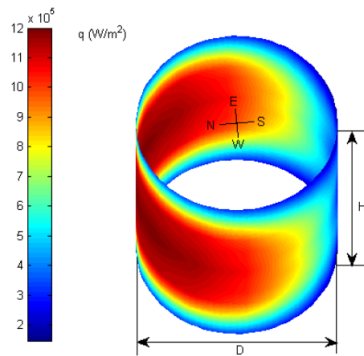


Figure 3.7: Typical flux asymmetry on cylindrical receivers [25]

The model works for various types of HTF, such as solar salts and liquid sodium, and pipe materials, such as Haynes 230, Alloy 800H and Alloy 740H. Going into the details, for symmetric heat flux maps, as in the present study, it is possible to run the model for only half of the receiver, halving the run time but maintaining high accuracy. It is also possible to optimize the outer diameter of the tubes according to the trade-off between HTF pumping power consumption, due to pressure losses that decrease as the diameter increases, and receiver heat transfer efficiency, which exhibits a maximum. The standard outer diameters and the relative thicknesses used for this optimization are obtained from the ANSI/ASME B36.10M standard [69] and are shown in Table 3.2.

Diameter [mm]	6.35	10.3	13.7	17.1	21.3	26.7	33.4	42.2	48.3	60.3
Thickness [mm]	1.22	1.24	1.65	1.65	1.65	1.65	1.65	1.65	1.65	1.65

Table 3.2: Standard diameters and thicknesses employed in the tubes optimization

From the receiver dimensions, after setting the tubes' outer diameter, thickness and spacing, along with the number of flows and panels, the model derives the number of parallel tubes per panel. Then, each pipe is divided into N_{ax} axial discretizations and $N_c = 4 \cdot N_s$ circumferential discretizations. Therefore, N_s results in the number of tube's discretizations along a quarter of a circumference. These make it possible to estimate the heat conduction along the tube's circumference (among adjacent control volumes), improving the accuracy of the results. The back of each tube is in contact with an insulating and supporting material, so this region is adiabatic and does not contribute to convective and radiative heat losses. N_{ax} and N_s determine the trade-off between model accuracy and computational time.

The heat flux map from SolarPILOT is discretized and interpolated to obtain elementary heat fluxes that match the pattern of the tubes' discretizations. As shown in Figure 3.8, for each element, the heat flux faces absorption, radiative and convective losses by forced and natural convection (computed from the wind velocity as a function of the tower height, obtained by linear interpolation) on the outer tube's surface, conductive losses within the thickness, and convective losses along the inner wall due to heat exchange with the HTF.

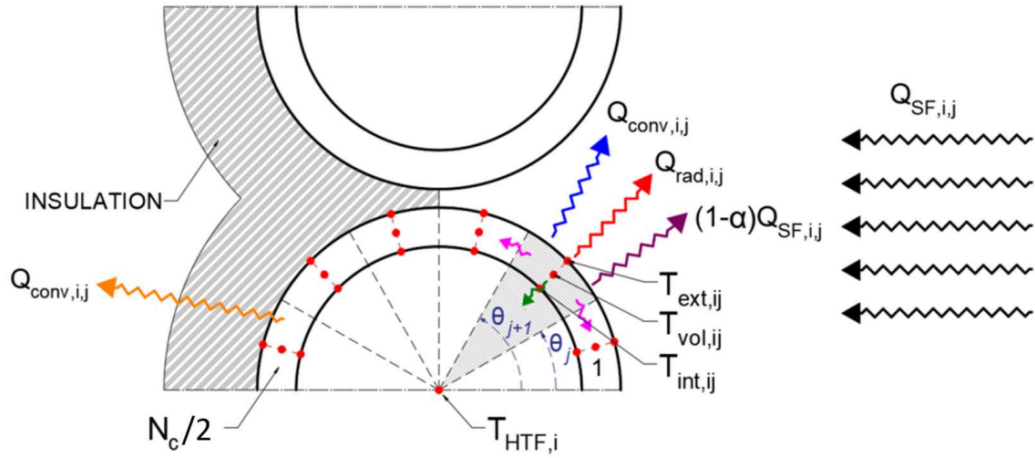


Figure 3.8: Cross section of the receiver tubes and heat transfer mechanism [68]

In the present study, 2 HTF flows are used in parallel in both receiver types, with 2 panels per flow in series in the Billboard case and 9 in the cylindrical case [70]. A single-pass model with just 1 flow within a single panel is also tested for the Billboard receiver. However, this configuration requires a much greater computational time and is not realistic for large receivers, offering less accurate results for few discretizations because of the large matrixes due to the huge panel’s size. For these reasons, such model is not employed in the study. A schematization of the two layouts studied is shown in Figure 3.9.

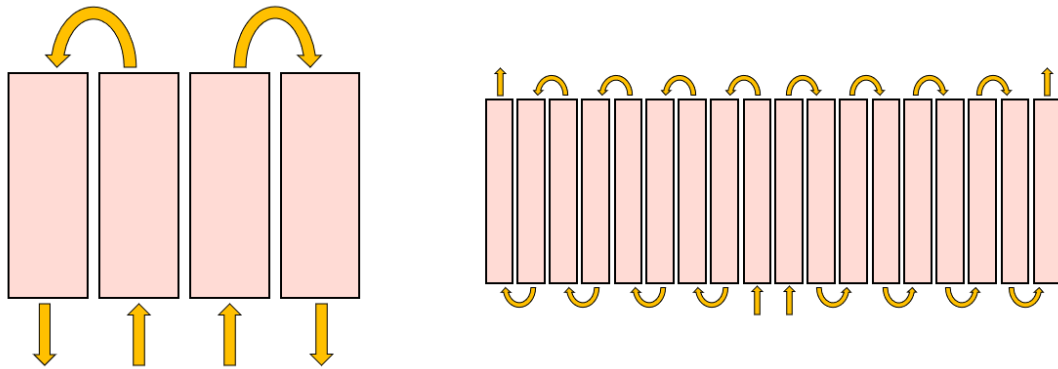


Figure 3.9: Layout of the Billboard receiver (left) and cylindrical receiver (right)

Given the need to run the model many times, it is necessary to deepen the trade-off between accuracy and computational time as a function of N_{ax} , N_s , and the receiver size (thus its external surface). This analysis is carried out for the Billboard receiver.

As for the cylindrical receiver, the computational time is generally much lower than the Billboard one because, for the same external surface, its panels (18 instead of 4) are made

of much less tubes each, therefore the matrixes are smaller. In this case, the same study on N_{ax} and N_s is already carried out in [68]. It is found that the results converge, while limiting the computational time, for $N_{ax} = 20$ and $N_s = 4$, in terms of both thermal efficiency and tubes' temperature distribution.

3.2.1. Off-design

The off-design performances are evaluated through thermal efficiency curves as a function of the thermal power ratio with respect to design conditions, by scaling the design heat flux map. In fact, the receiver performances are almost independent of the flux distribution on its surface compared to the average flux value. In practice, the receiver thermal efficiency is almost independent of the sun position.

3.3. Piping system model

When the modular configuration is considered, the piping between the storage tanks and the different solar towers must be carefully designed, and its thermo-hydraulic performances evaluated.

To address this issue, a model on Matlab is developed to assess both the performances and the costs of the piping system. This is a very flexible model, in fact it can be used for systems with any number of modules, any size and layout (surrounding or polar fields), and any HTF whose properties are specified. Also, the modelling of North-oriented and South-oriented fields is identical, as the whole system is simply rotated by 180° .

The working principle of the model is based on the assimilation of modules to rectangles, even if they can have any layout that is inscribed within a rectangle. A second assumption is that the TES and PB occupy a rectangular region with a size equivalent to one module. In addition, it is assumed that all modules have the same geometry (field layout, tower height, receiver size), always operate under the same conditions (mass flow rate, temperature difference and pressure drops in the receiver), and that the riser and downcomer inside the towers are adiabatic, while still causing pressure drops and raising costs.

The land occupied by each module is counted as the rectangle that inscribes its shape. This procedure is chosen because the empty spaces between adjacent modules, although physically unused, must necessarily be purchased since they fall within the plant's boundaries. For conventional plants, only the land bounded by the field's outermost heliostats is considered, even if irregularly shaped, since there is no reason why additional space outside the field should be purchased, and to ensure a fair comparison between the two

cases. The space occupied by the TES, PB and all auxiliary systems is calculated in the conventional system as the circular region bounded by the minimum solar field radius, in the proximity of the tower. In the modular case, this is counted in two different ways:

- If the region containing TES, PB and auxiliary systems is at the boundaries of the field, this area is the same as the conventional field case, at constant electric power.
- If this region is surrounded by modules, thus contained within the core of the plant, a surface equivalent to one module is accounted for.

3.3.1. Structure

Going into more detail about the design code, whose starting frame is like the one used in [71], this consists of a main code that in turn invokes two secondary functions, as well as a code for optimizing the HTF velocity. Furthermore, the layout of the modules on the ground can be either optimized with an additional code, having sufficient available space, or given as input with a layout matrix with the following constraints.

- The matrix must be square with odd side.
- The PB, represented by number 2, must be placed in the centre of the matrix.
- The modules are represented by number 1, while all the other values must be 0.
- All the values close to the boundaries (first and last row and column) must be 0.

Despite these purely programming constraints, such approach allows for the representation of every possible configuration within a checkerboard layout.

The scheme of a generic modular plant layout including the piping system is reported in Figure 3.10, while an example of the layout matrix for the same field is shown in Figure 3.11.

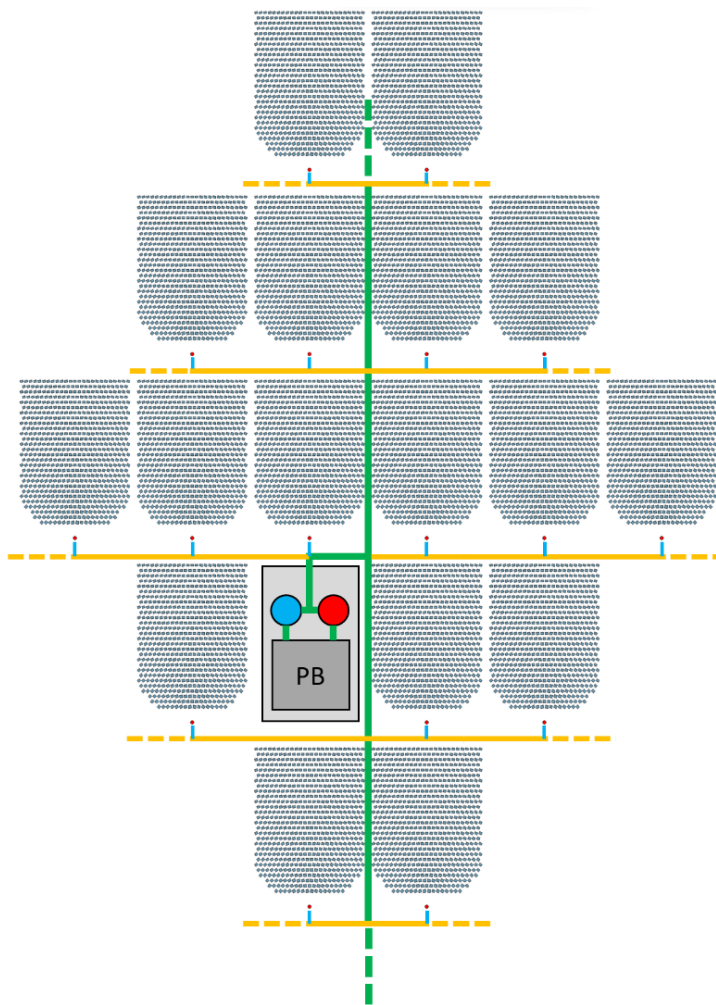


Figure 3.10: Schematization of the piping system’s modelling of a modular plant

0	0	0	0	0	0	0	0	0
0	0	0	0	0	0	0	0	0
0	0	0	0	0	0	0	0	0
0	0	0	1	1	0	0	0	0
0	0	1	1	2	1	0	0	0
0	1	1	1	1	1	1	0	0
0	0	1	1	1	1	0	0	0
0	0	0	1	1	0	0	0	0
0	0	0	0	0	0	0	0	0

Figure 3.11: Example of the layout matrix for the layout illustrated in Figure 3.10

The field layout’s optimization receives as input the size and the number of modules, and arranges them to minimize the average distance of each tower from the TES, thus minimizing thermal losses, major pressure losses and costs.

The main code is the point of interaction with the external user, where the input param-

eters are set and the outputs are provided. The field layout matrix is divided into six regions and the pipes are classified into main collectors, rows, and ground pipes to each tower, which are coloured in green, orange, and light blue, respectively, in Figure 3.10. The figure represents just one line for each path but there are actually two parallel pipelines, a cold one and a hot one. The order of the calculations follows the HTF path, first from the cold tank (which is assumed at $T_{min} = 290^{\circ}\text{C}$) to the receiver inlet and then from the receiver outlet (which is assumed at $T_{max} = 565^{\circ}\text{C}$) to the hot tank, by invoking two secondary functions for each straight pipe between two intersections. Specifically, first the geometry of all pipes is designed and their thermal losses are calculated, then the pressure losses are computed once the geometry is known. A schematic of the procedure is shown in Figure 3.12.

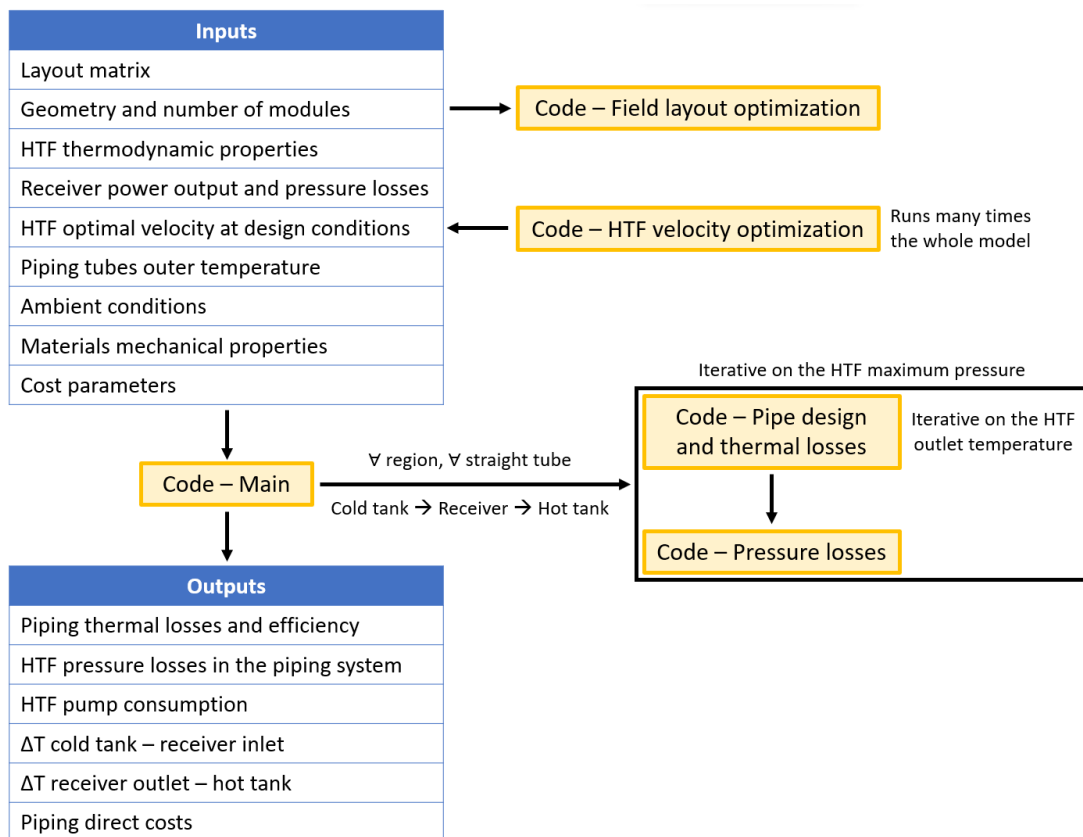


Figure 3.12: Flow diagram for the piping model of modular plants

3.3.2. Pressure constraints

The pressure jump provided by the single HTF pump at the exit of the cold tank is calculated as:

$$\Delta P_{pump,close-loop} = P_{loss,pip} + \Delta P_{rec}$$

$$\Delta P_{pump,open-loop} = P_{loss,pip,cold} + \Delta P_{rec} + \Delta P_{geo,tower} + \max((P_{loss,pip,cold}) - \Delta P_{geo,tower}, 0)$$

If the storage configuration is indirect, in a closed-loop layout, the geodetic term is not considered in the pressure losses as it is fully recovered.

If the direct storage configuration is adopted, the geodetic pressure drops of the HTF flowing to the top of the tower are included but they can be partially recovered in the hot path of the piping system, since the layout is open-loop.

The maximum pressure, that is the HTF pump outlet pressure, is required to overcome all the pressure drops from the TES to the tower under the most unfavourable conditions and back, including those attributed to the receiver, assuming the presence of regulation valves at the base of each tower ensuring isobaric mixes.

Finally, two additional pressure constraints are set. The pressure at the receiver outlet must not be lower than the ambient pressure to avoid the HTF evaporation in the operating temperature range. Moreover, the pressure in the storage tanks must not be lower than the ambient one to avoid infiltrations from outside.

3.3.3. Mechanical design and thermal losses

In the code for the piping design and thermal analysis, the inner diameter of the duct D_{int} of each piping section is computed from the HTF velocity v_{HTF} and knowing its mass flow rate m_{HTF} as:

$$D_{int} = \sqrt{\frac{4 \cdot m_{HTF}}{\pi \cdot \rho_{HTF} \cdot v_{HTF}}}$$

while the thickness t is computed from [72] to resist to the mechanical stress with a security factor $F = 1.5$

$$t = \frac{(P_{max} - P_{amb}) \cdot D_{int}}{2 \cdot \frac{\sigma_{adm}}{F} + 0.4 \cdot (P_{max} - P_{amb})}$$

Where P_{max} is the maximum pressure at the outlet of the HTF pump ($= P_{cold,tank} + \Delta P_{pump}$), P_{amb} is the ambient pressure and σ_{adm} is the admissible normal stress, which is set according to [73].

All the pipes of the system are sized on the maximum pressure. This conservative assumption is made both for safety reasons and for computational simplicity. Anyway, the hot piping path is generally at high pressure, due to the recovery of the geodetic head at the base of the tower.

In addition, the number and length of the U-shaped expansion loops needed to accommodate the piping thermal expansion are also computed, assuming a fixed distance between two consecutive loops. In Figure 3.13 the geometry of an expansion loop is shown, while the relation from [74] is used to compute its width W_{loop} .

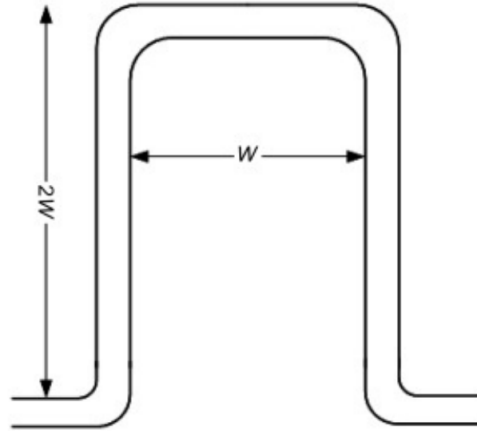


Figure 3.13: Geometry of an expansion loop [75]

$$W_{loop} = 15 \cdot \sqrt{\alpha_{exp} \cdot (T_{HTF} - T_{amb}) \cdot D_{in,max} \cdot \frac{L_{pipe}}{N_{loops}}}$$

Where α_{exp} is the material's temperature expansion coefficient, T_{HTF} is the HTF local temperature, T_{amb} is the ambient temperature, $D_{in,max}$ is the maximum pipe's inlet diameter, L_{pipe} is the length of the straight pipe, and N_{loops} is the number of expansion loops within that length.

The material adopted for piping is stainless steel 316. To minimize thermal losses, two layers of mineral fiber having different maximum temperatures (the first 600°C and the second 300°C) are included. In addition, one layer of ceramic fiber is also considered in configurations adopting a HTF overcoming 600°C [76].

The design is made imposing a piping outer temperature $T_{ext,des}$ at design conditions. The temperature difference with the ambient must be low both for reducing thermal losses and for safety reasons. To reach these conditions, starting from the inner diameter

of the pipe, a thermal resistance network is computed to establish the diameters of the insulation layers $D_{out,mf1|2}$ (thus their thicknesses) to achieve the temperature $T_{ext,des}$ on the outer surface, within an iterative procedure on the HTF temperature at the exit of the tube T_{out} . The main equations of this procedure are reported for the case of solar salts at 565°C , while a scheme of the thermal resistance network is shown in Figure 3.14.

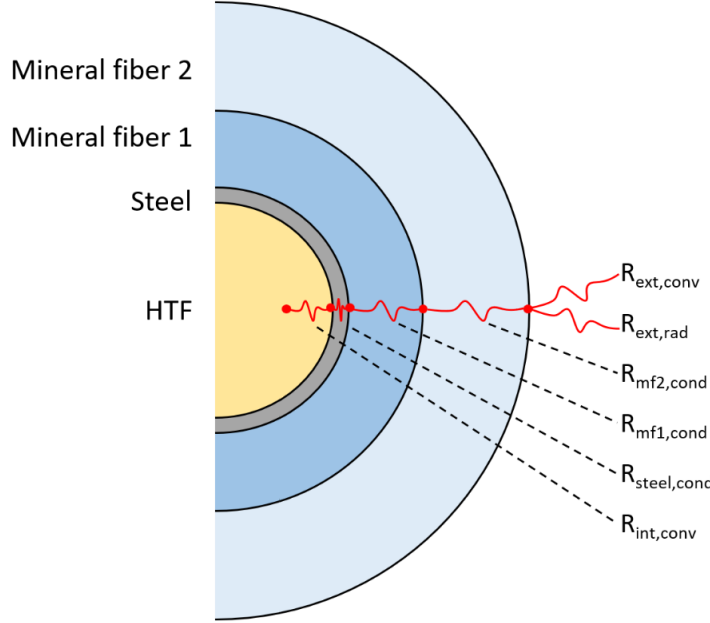


Figure 3.14: Thermal resistance network in the piping system's tubes

$$h_{in} = \frac{Nu_{HTF} \cdot k_{HTF}}{D_{in}}$$

$$h_{out} = h_{mix} + h_{rad}$$

$$R_{in|out} = \frac{1}{\pi \cdot D_{in,steel|out,mf2} \cdot h_{in|out}}$$

$$R_{steel|mf1,2} = \frac{\ln \frac{D_{out,steel|mf1,2}}{D_{in,steel|mf1,2}}}{2 \cdot \pi \cdot k_{steel|mf1,2}}$$

$$R_{tot} = R_{in} + R_{steel} + R_{mf1} + R_{mf2} + R_{out}$$

$$Q_{loss} = (T_{av} - T_{amb}) \cdot \frac{L_{pipe}}{R_{tot}}$$

$$T_{wall,in} = T_{av} - Q_{loss} \cdot \frac{R_{in}}{L_{pipe}}$$

$$T_{out,new} = T_{in} - \frac{Q_{loss}}{m_{flow} \cdot c_p}$$

Where h are the convective heat transfer coefficients, k are the thermal conductivities, R are the thermal resistances, Q is the thermal power, and c_p is the specific heat capacity.

The thermal losses of each section are calculated from the total thermal resistance and the average fluid temperature T_{av} between inlet and outlet. The pipe is not discretized axially because, since the temperature differences between inlet and outlet of each straight tube are very small, this would bring minimal benefits at the cost of a significant increase in the computational time. Furthermore, the conductive thermal losses through the supports that elevate the tubes from the ground are neglected. For the internal convection coefficient calculation, the Petukhov-Gnielinsky correlation is adopted for solar salts:

$$Nu_{HTF} = \frac{\frac{f}{8} \cdot (Re - 1000) \cdot Pr}{1.07 + 12.7 \cdot \sqrt{\frac{f}{8}} \cdot (Pr^{\frac{2}{3}} - 1)} \cdot \left(1 + \left(\frac{D_{in}}{L_{pipe}} \right)^{\frac{2}{3}} \right) \cdot \left(\frac{Pr}{Pr_w} \right)^{0.11}$$

While the Subbotin correlation is adopted for sodium:

$$Nu_{HTF} = 5 + 0.025 \cdot Pe^{0.8}$$

Where f is the friction factor, Re is the Reynolds number, Pr is the Prandtl number, Pr_w is the Prandtl number at the wall temperature, Pe is the Peclet number, Nu is the Nusselt number, and D_{in} is the pipe's inlet diameter.

Finally, a constant value of $h_{mix} = 10 \text{ W/m}^2\text{K}$ is assumed for the combined natural and forced convection with the external environment, while the radiative losses are computed from the surroundings temperature, even if their value is negligible due to the low temperature difference and the presence of a low-emissivity external aluminium foil cladding.

$$h_{rad} = \epsilon \cdot \sigma \cdot (T_{ext}^2 + T_{surr}^2) \cdot (T_{ext} + T_{surr})$$

Where ϵ is the external surface emissivity, $\sigma = 5.67 \cdot 10^{-8} \text{ W/m}^2\text{K}^4$ is the Stefan-Boltzmann constant, T_{ext} is the external pipe's temperature and T_{surr} the surroundings temperature.

3.3.4. Pressure losses

The concentrated (minor) and distributed (major) pressure losses are computed for each section once diameters, flow rates and velocities are known.

For minor pressure losses, the cases of "elbow", "combining T junction", "dividing T junction", "combining X junction" and "dividing X junction" are considered. The minor

loss coefficients for T junctions are obtained by interpolation of values from the tables reported in [77], depending on the cross section and volumetric flow rate ratios between the line and branch flows, while the X junctions are modelled as the combination of two T junctions. All the elbows are assumed to be flanged with a 90° curvature, and their minor loss coefficients are calculated from the following correlation function of the Reynolds number [78]:

$$K_{elbow} = 1.49 \cdot Re^{-0.145}$$

On the other hand, the implicit Colebrook equation, for $Re > 4000$, is computed iteratively to determine the friction factor for major pressure losses:

$$\frac{1}{\sqrt{f}} = -2 \cdot \log \left(\frac{2.51}{Re \cdot f} + \frac{\epsilon}{D_{in} \cdot 3.72} \right)$$

Where f is the friction factor, D_{in} is the internal diameter of the pipe and ϵ is the pipe roughness for stainless steel, whose value is set to 0.09mm.

Finally, the total pressure losses of each section are derived as the sum of concentrated and distributed pressure losses:

$$P_{loss} = \left(K_{minor} + f \cdot \frac{L_{pipe}}{D_{int}} \right) \cdot \rho_{HTF} \cdot \frac{v_{HTF}^2}{2}$$

Where K_{minor} is the sum of all minor pressure loss coefficients in the considered pipe.

3.3.5. Velocity optimization

The optimal HTF velocity at design conditions is computed minimising the piping system's total losses, that include the thermal losses and the power absorbed by the HTF pump (converted with a reference power block thermal-to-electric efficiency $\eta_{PB,ref}=40\%$). The variation of the reference PB efficiency turns out to have a negligible effect on the optimal velocity value. A second optimization procedure minimizes the specific cost [\$/kW_{th}] of the thermal power transferred to the TES. This function considers not only the system's thermal and pressure losses, but also its costs.

$$Q_{loss,tot} = Q_{loss,th} + \frac{W_{HTF,pump}}{\eta_{PB,ref}}$$

$$Cost_{spec} = \frac{Cost_{piping}}{Q_{in} - Q_{loss,tot}}$$

$$v_{HTF,opt,des} = \min(Q_{loss,tot} || Cost_{spec})$$

Figure 3.15 shows an example of the trends in thermal power losses, HTF pump power consumption, and piping specific cost as the HTF velocity changes.

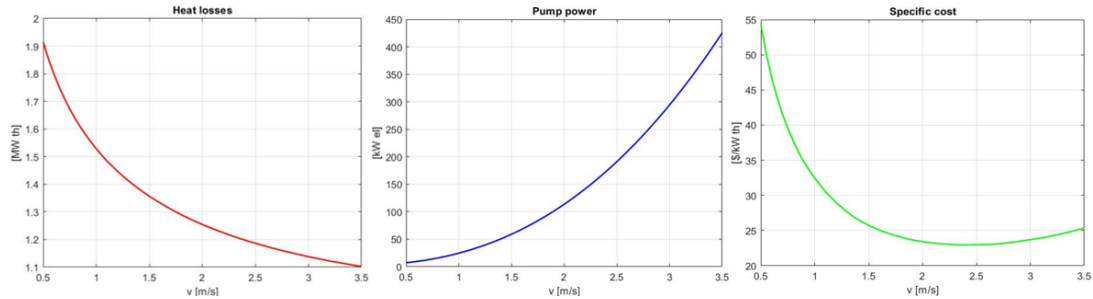


Figure 3.15: Example of the trends of thermal losses (left), HTF pump consumption (middle), specific costs of piping (right) as a function of the HTF velocity

It is verified from simulations that the minimum in specific costs occurs because of two different trends for the same HTF mass flow rate.

For low HTF velocity the pipe's diameter increases, while its thickness decreases due to the limited mechanical stress. This causes a modest increase in the amount of steel required, which adds to the increase in the insulation required due to the larger diameter, although convective heat transfer on the inner wall is reduced due to the low velocity.

For high HTF velocities, on the other hand, the reduction in the amount of insulation due to the reduction in the pipe's diameter is less pronounced than the increase due to higher losses because of the improved convective heat transfer. Moreover, the amount of steel required increases substantially because of the greater thickness that pipes must have to resist to the mechanical stresses due to the increase in the maximum pressure, even though the pipe's diameter decreases.

The validity of the optimization procedure is checked in terms of resulting HTF velocity with literature results, obtaining coherent values with those reported in [79] and [80].

3.3.6. Off-design

The off-design model generates maps of piping thermal efficiency and power absorbed by the HTF pump, as a function of the thermal power ratio with respect to design conditions and the ambient temperature, assuming the same operating conditions for all modules. This model uses the plant's geometry from the design piping model and the fluid's mass

flow rate and pressure drops from the receiver model in off-design. The HTF velocity is computed starting from the diameter and the mass flow rate, unlike in design conditions where it is used to size the pipes.

A negligible dependency of the off-design performances from the ambient temperature variation is observed, mainly due to the contextual change in the thermal conductivity of the outermost insulation layer (mineral fiber 2), which decreases as the temperature goes down, as shown in Figure 3.16. In practice, an ambient temperature decrease induces a reduction of the outer insulation layer's thermal conductivity, that is computed from a second-order polynomial as a function of the average temperature between the tube's external temperature and the allowable temperature of the material (300°C). This thermal conductivity reduction leads to an increase in the conductive thermal resistance of the outer layer, which effect almost balances the ambient temperature reduction.

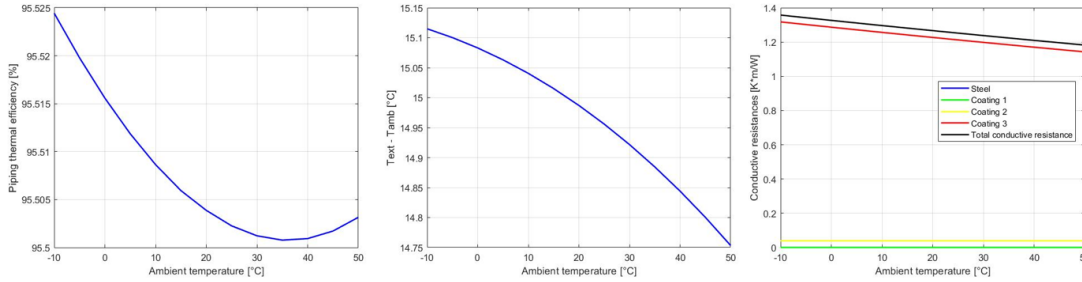


Figure 3.16: Example of the piping efficiency (left), external surface – ambient temperature difference (middle), and conductive resistances (right) as a function of the ambient temperature

Finally, the HTF pump's efficiency in off-design conditions is computed from the simplified approach proposed in [80] as:

$$\eta_{pump,ann} = \eta_{pump,des} \cdot \left(2 \cdot \left(\frac{m_{HTF,ann}}{m_{HTF,des}} \right) - \left(\frac{m_{HTF,ann}}{m_{HTF,des}} \right)^2 \right)$$

3.4. Power Block model

The PB models are needed to investigate the design and annual operation of this component, to evaluate performances and costs. For each cycle's layout, a desired net electric power is set as input to get the cycle efficiency as output. This efficiency allows to evaluate the thermal power input to the PB, necessary to size the TES and evaluate the solar multiple (SM), allowing to complete the plant's design.

3.4.1. 1-reheat cycle

The first model used for the power block operation, a subcritical steam Rankine cycle with 1 reheat, is developed in [81] on Thermoflex [63]. This is a heat balance software, that covers both design and off-design simulations. Figure 3.17 shows the schematic of the cycle.

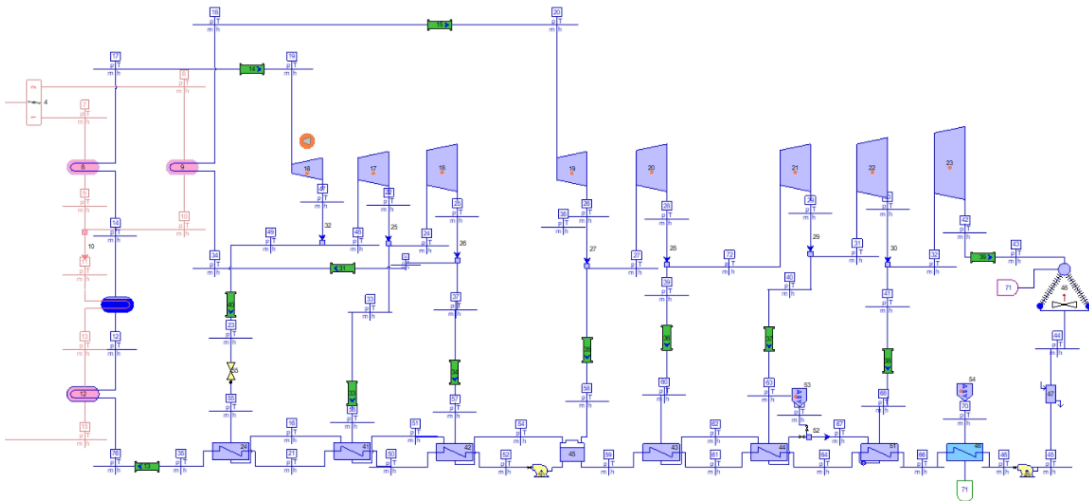


Figure 3.17: Schematization of the 1-reheat steam Rankine cycle on Thermoflex

The maximum pressure is set to 170bar. Moreover, the steam turbine has 8 stages: 3 high-pressure (HP), followed by the unique reheat, 2 medium-pressure (MP) and 3 low-pressure (LP). The condenser is air-cooled, as common for CSP plants that are usually located in regions with scarcity of running water. In addition, there are 4 low-pressure preheaters receiving steam spillages from the MP and LP stages of the turbine, a deaerator, and 3 high-pressure preheaters receiving spillages from the HP stages. Finally, the economizer, the superheater and the reheater consist of shell and tube heat exchangers with water/steam inside the tubes, while the evaporator is a shell and tube heat exchanger with solar salts on the tubes side and water evaporating outside.

3.4.2. 2-reheats cycle

From the cycle just shown, the model of a 2-reheats power block is derived to increase the average heating temperature and the maximum pressure, while still ensuring a dry expansion in the last LP stages. Both effects lead to an increase in the net electric efficiency compared to the 1-reheat case. The new plant configuration is shown in Figure 3.18.

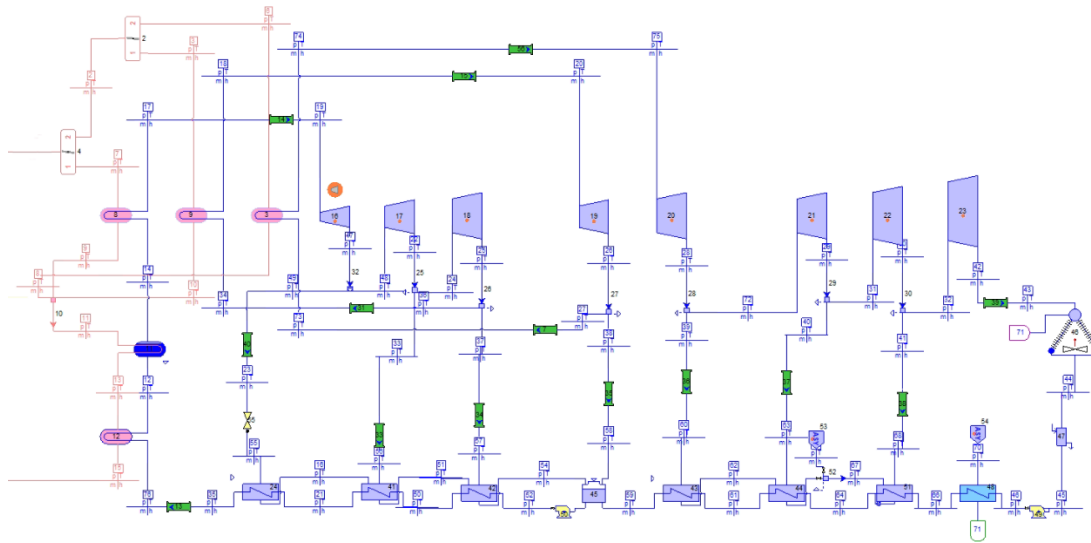


Figure 3.18: Schematization of the 2-reheats steam Rankine cycle on Thermoflex

In this cycle, the maximum pressure is increased to 190bar, and the steam flow distribution supplied by the second splitter to the reheats is optimized to maximize the cycle's net electric efficiency. In order not to excessively reduce the temperature before the second reheat, this is placed between the first and second MP stages and occurs, as the first reheat, inside a shell-and-tube heat exchanger with steam in the tubes side. The remaining cycle components are not changed from the previous case.

3.4.3. Off-design

In off-design conditions, the cycle's performance curves as the ambient temperature changes, affecting the air condenser's performance, are obtained, while the performances in partial load conditions are not investigated. This is because, given the simple TES operating strategy chosen for the present study, the PB either operates at full load maximizing the electric efficiency, or it is completely shut down.

3.5. Modular plant design and optimization

To optimize a modular CSP plant and compare such an optimal solution with a conventional plant, it is necessary to divide the procedure into several independent and consecutive steps, making the design process straightforward and avoiding iterative loops that complicate the procedure and increase the computational time. First, the least-cost modules are identified. Then, they are employed in the analysis of the whole plant.

The first step in the modular plant's optimization, after choosing an appropriate location, is to define modules of various sizes in terms of thermal power delivered to the outer surface of the receiver. For each size, many possibilities in terms of field layout, tower type, and receiver type are investigated. For each power size and type of module, each relevant parameter to reduce the LCOH is then defined and optimized.

Knowing the maximum flux (1 MW/m^2 for solar salts), the desired thermal power, and the type of field and receiver, the minimum size of the receiver that satisfies the flux constraint is set to reduce its capital cost as much as possible. This is simplified by choosing an aspect ratio, defined as $AR = H/W$ for Billboard receivers and $AR = H/D$ for cylindrical ones, in accordance with the typical values given in literature. Then, after having set an AR also for heliostats, a parametric analysis on SolarPILOT is performed by varying their size to find the maximum dimensions that ensure high spillage efficiency, thus reducing the number of mirrors and the system's complexity. In this study, it is then chosen for simplicity to increase linearly the heliostats' side with the supplied thermal power and thus proportionally to the receiver area, since the average flux is almost constant.

In the case of Billboard receivers, the tilt angle is also optimized to improve the spillage efficiency due to the larger area seen from the solar field. The optimization is held through a parametric analysis on SolarPILOT, gradually increasing the tilt until either a plateau in the optical efficiency is reached or the software starts placing mirrors behind the tower, a solution that is not acceptable.

At this point, the outer diameter of the receiver tubes is optimized, before applying the models for the analysis of the receiver's design and off-design operation.

Concerning the position of the tower along the north-south axis in surrounded fields, the default placement in SolarPILOT provides an optical optimum without considering the receiver's performance. Therefore, the tower location is investigated in surrounded modules, first from a purely thermodynamic perspective, identifying the maximum performance under design conditions, and then from an economic perspective, with the LCOH.

After establishing the geometry of the field's components, it is necessary to optimize the tower height. This trade-off is analysed on an annual basis with the LCOH through several cases in which the height is varied with a 10m step each time. A maximum height of 150m for steel monopole towers is considered, beyond which the tower is built in concrete as in most of the existing conventional plants. The minimum LCOH configuration is then selected.

Hence, several optimized modules are obtained, which differ in size (thermal power to

the receiver) and features of the solar field. Each module is characterized by a LCOH and occupies a certain area, which indirectly influences the piping system. In terms of performances, the combined efficiency of modules is defined as the product between optical efficiency and thermal efficiency.

A first selection among the alternatives is made to get few sub-optimal solutions to be evaluated at the plant's level. In fact, after identifying the module providing the lowest LCOH:

1. All modules of lower size and higher LCOH are discarded.
2. All modules of equivalent size and LCOH but occupying a larger area are discarded.
3. Modules of larger size with slightly higher LCOH cannot be discarded in advance, because less of them may be needed for the same power output, reducing the extent and the cost of the piping system. However, some cases among the latter can still be eliminated based on the first two criteria.

After identifying the best-performing modules, it is necessary to choose their number to obtain approximately the desired electric power, assuming a first guess solar multiple. Then, the piping system is analysed and the HTF velocity optimization is done by minimizing either the total losses or the specific costs. Subsequently, the models for the design case and the annual analysis are applied. Moreover, since the objective is to analyse large-scale plants with no spatial constraints, the code for the layout optimization is employed.

Next, the optimization of the SM [-] and TES size [h] is performed to further minimize the LCOE by sizing the last two plant components, PB and TES. In the present study, the solar multiple is varied by changing the power block's net electric power output with a 10% step from the first guess value. This procedure is simpler and more accurate than varying the number of modules when the plant is made of few large modules. In contrast, in the case where the plant consists of many small modules, it would be more accurate to vary the number of modules and keep the net electric power output constant.

As for the TES size optimization, for each SM, the TES maximum capacity is varied, identifying the solution that guarantees the lowest LCOE. To carry out this analysis, the simplest TES operating strategy is considered, where the power block works only at full load (under nominal conditions), maximizing its efficiency. The adopted TES strategy is shown in Table 3.3.

	SF power > PB power	SF power < PB power
TES not full	PB: full load, TES charged	
TES full	PB: full load, Excess: defocusing	
TES not empty		PB: full load, TES discharged
TES empty		PB: shut down, TES charged

Table 3.3: TES operating strategy

Finally, among the few remaining modular optimized plants, one of them provides the lowest LCOE or is the most compact. The final choice depends on the needs.

A schematization of the process and all the optimizations required to carry out the design of a modular CSP plant is shown in Figure 3.19.

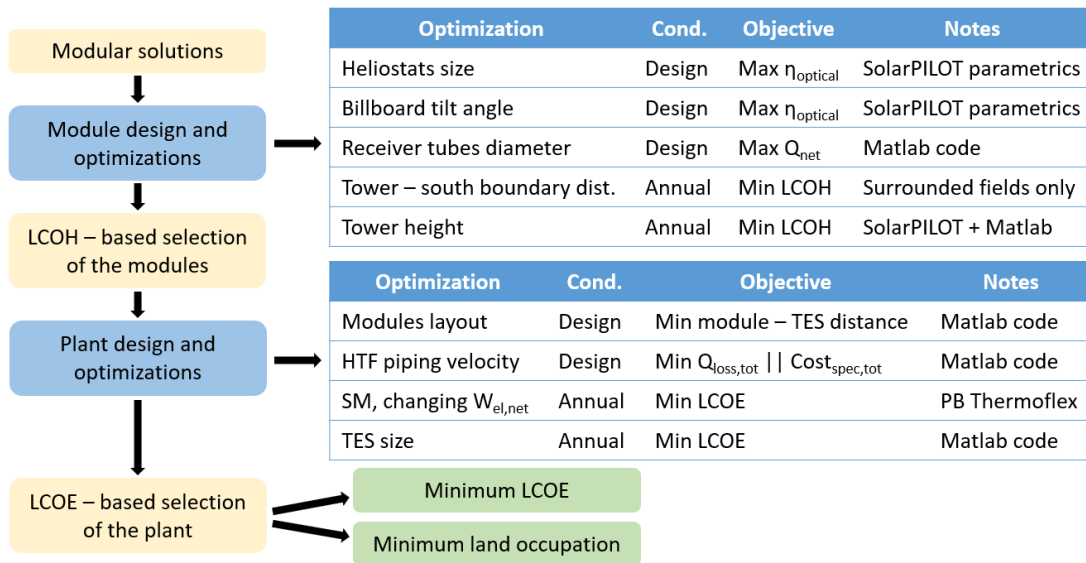


Figure 3.19: Flow diagram of the steps and optimizations for the design of a modular CSP plant

3.6. Conventional plant design and optimization

The optimization of a conventional state-of-the-art plant, which is necessary to perform a fair comparison with the modular case, is much simpler. In fact, it includes less steps and just one case is analysed because the solar field’s geometry is unique.

Starting from the maximum flux and the desired thermal power output, the dimensions of the cylindrical receiver are determined, after assuming an appropriate AR. Then, thanks to

a parametric analysis on SolarPILOT, the size of the heliostats is derived. Subsequently, the outer diameter of the receiver tubes is optimized under design conditions and the design and off-design models are applied. This is done for different tower heights, and the annual results are compared with the LCOH. Then, the piping models and the HTF velocity optimization are applied. Next, it is possible to optimize the last two parameters for minimizing the LCOE, which are SM and TES size.

In analogy with the modular case, the same solar field is used and the PB's electric power is varied with a 10% step from the first guess value. This procedure avoids the generation of several solar fields, reducing the computational time. It is possible that, by following this SM optimization mode, the electric power output of the modular system results different, by a small amount, from the conventional one. However, this does not invalidate the comparison, since the sizes are still similar, the technologies are the same, and the comparison takes place through intensive indicators.

Finally, for each SM, the TES size is varied to find the one providing the minimum LCOE.

A schematization of the process and all the optimizations required to carry out the design of a conventional state-of-the-art CSP plant is shown in Figure 3.20.

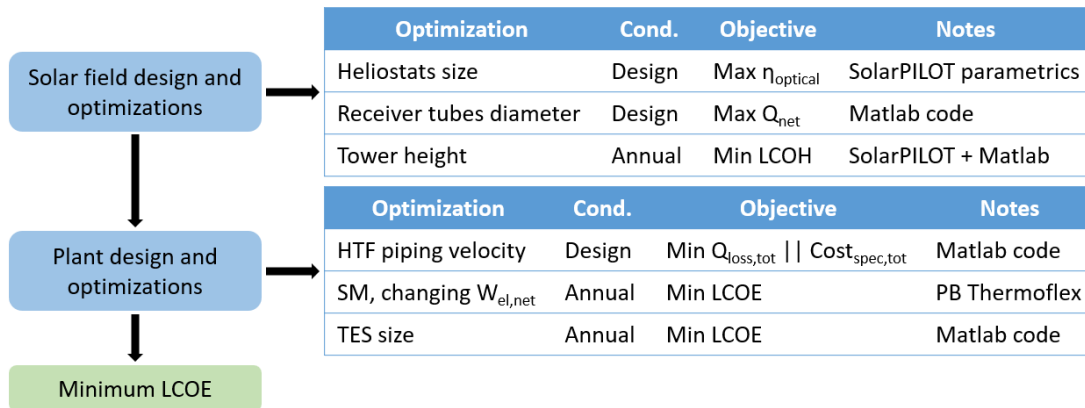


Figure 3.20: Flow diagram of the steps and optimizations for the design of a conventional CSP plant

3.7. Annual analysis

In the plant's annual analysis, carried out through an additional code developed on Matlab, the following relevant indicators are derived. These are the most representatives for the performances and costs of CSP plants, thus they are necessary to perform accurate comparisons between different layouts.

- Design and annual efficiencies (optical, receiver, piping, power block, auxiliary (HTF pump), solar-to-electric), the equations of which are given in Appendix A.
- Solar multiple (SM), defined as the ratio of thermal power delivered by the HTF after piping over thermal power input to the power block under design conditions.

$$SM = \frac{Q_{HTF,net}}{Q_{PB,in}}$$

This parameter is crucial in CSP plants because it determines the proportion of heat stored to the total heat produced, making it possible to decouple solar resource and electric generation by oversizing the solar field with respect to the power cycle. Therefore, its variation allows to change the weight of individual modules or power block on the total costs. Acting on the power block, the denominator changes following the relation:

$$Q_{PB,in} = \frac{W_{el,net}}{\eta_{PB,net}}$$

- TES size
- Net electric power output ($W_{el,des}$)
- Annual electricity production (AEP)
- Levelized cost of electricity (LCOE)
- Capacity factor (CF):

$$CF = \frac{AEP}{W_{el,des} \cdot 8760}$$

- Specific capital costs ($Cost_{spec}$):

$$Cost_{spec} = \frac{CAPEX}{W_{el,des}}$$

- Land-specific productivity (LSP) [GWh/km²y], a new intensive indicator representing the amount of electricity produced in one year per actual km² of land occupied by the plant, and allowing to compare plants with different layouts. In practice, this is an indicator of a plant's compactness in the electricity production, or even of the effectiveness of a plant's land use.

$$LSP = \frac{AEP}{Land}$$

4 | Case study

After detailing the models used for each component and the design and optimization methodology for both modular and conventional plants, it is necessary to specify all the technical data and assumptions used within this study, along with the scenarios analysed.

4.1. Vast Solar modules

To test the proper functioning of the models, except the power block one, and to further investigate the various trade-offs on components, an initial case study is conducted comparing a modular plant with a conventional plant of equivalent electric power.

The location chosen is Jemalong (New South Wales, Australia) which has an annual DNI equal to 2398 kWh/m²y. Two 5 MW_{el} plants with liquid sodium as HTF, Billboard receivers mounted on steel towers, two-tank TES in indirect configuration and steam Rankine power block are compared in two different HTF temperature ranges: 730°C - 550°C and 580°C - 430°C. The modules, used by Vast Solar in the Jemalong pilot plant, are described in [30] and their geometry is obtained from [82]. These are rectangular polar modules with cornfield layout method and produce a nominal thermal power of 1.2 MW_{th} each. The number of modules and the TES size are varied to minimize the LCOE.

The conventional plant is realized by a single radial staggered polar field, the size of which is varied to reduce the LCOE. The TES size is optimized also in this case.

4.2. Large scale modular plants

The core of the thesis is the techno-economic analysis of large-scale modular plants and the comparison with conventional systems. The main data and assumptions, along with the three scenarios employed are described in the sections below.

4.2.1. Locations and scenarios

The analysis is carried out by considering two different locations that allow a broader spectrum of results and their validity to be verified in a generalized way, avoiding misleading conclusions due to a single location.

The first location chosen is Tucson (Arizona, USA). This is a common location for a CSP plant, in fact it has all the typical features previously described: low latitude, high annual DNI, scarcity of rainfall and large available space. A region with a too high DNI is not chosen because it represents a singularity. The goal is to investigate a case as representative and generic as possible for most plants worldwide, rather than to identify the absolute optimal location.

The second location is Calgary (Alberta, Canada). This is a deliberately uncommon location for CSP, which has very high latitude (as no plant in the world either operational or under construction) and an annual DNI around the feasibility threshold of $1800 \text{ kWh/m}^2\text{y}$. This choice is due to the aim of investigating the variation of the optical optimum conditions, thus the possible benefits that polar configurations offer as opposed to surrounded ones at high latitude, and whether modularity could ensure CSP feasibility even in locations up till now considered prohibitively expensive. In fact, there is no study to the author's knowledge that has investigated the CSP modularity in such locations, and if successful, it would open the possibility to widespread the deployment of CSP technology in a new market that does not exist to date.

The plots of the hourly DNI on an annual basis at the two locations, used to estimate the hourly power delivered by the sun, and the hourly ambient dry temperature on an annual basis for the thermal components' off-design analysis (receiver, piping, power block), are shown in Figure 4.1. The values for the two locations are both taken from the SolarPILOT climate files library. It is worth pointing out that while an increase in DNI certainly improves the plant's operation, the same cannot be said for the ambient temperature. In fact, as it grows, the thermal efficiency of the receiver increases, the piping efficiency remains almost constant, while the electric efficiency of the power block decreases due to the worse performance of the air-cooled condenser.

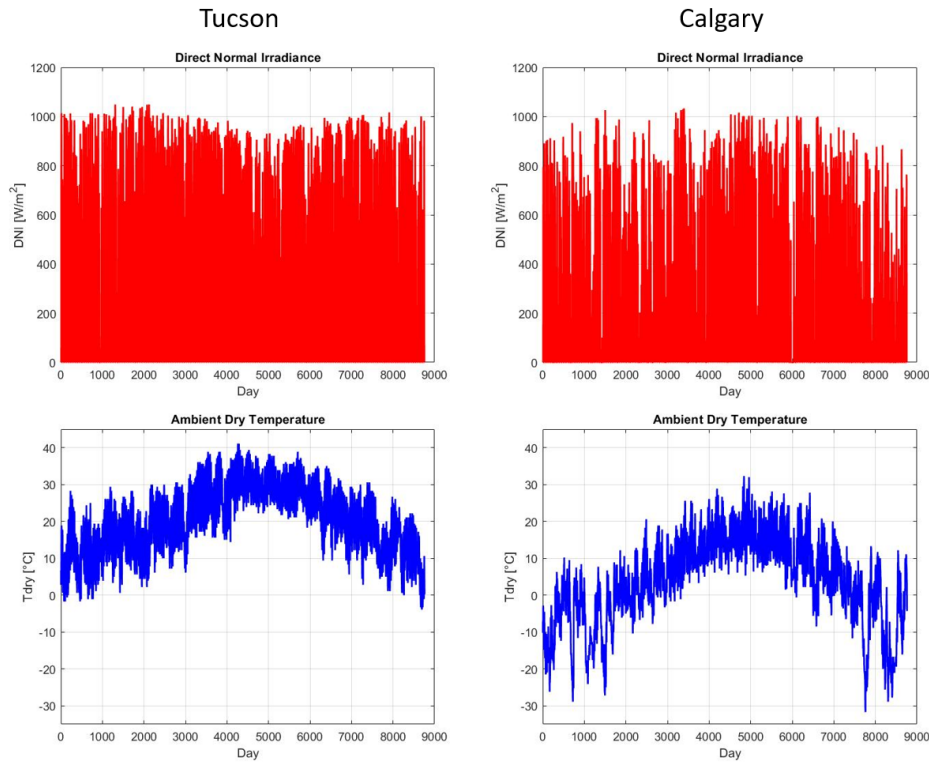


Figure 4.1: Annual DNI and annual ambient dry temperature in the two locations

Moreover, the study is made with a clear day atmospheric attenuation in both locations, and a hazy day atmospheric attenuation only in Tucson, aimed at verifying the benefits of modular fields under the possible unfavourable conditions due to desert locations. Therefore, 3 scenarios are analysed and, for each, a comparison is made at constant net electric power between the modular configurations and a corresponding conventional plant.

1. Tucson with clear atmospheric attenuation (Tucson clear)
2. Calgary with clear atmospheric attenuation (Calgary)
3. Tucson with hazy atmospheric attenuation (Tucson hazy)

In terms of geometry, five categories of modules are found to be the most interesting for further analysis, although additional combinations can also be defined.

1. Surrounded modules, radial stagger layout method, free shape
2. Surrounded modules, radial stagger layout method, square shape
3. Polar modules, radial stagger layout method, free shape
4. Polar modules, radial stagger layout method, square shape

5. Polar modules, cornfield layout method, rectangular shape

A schematic of all the scenarios and modules analysed is reported in Figure 4.2.

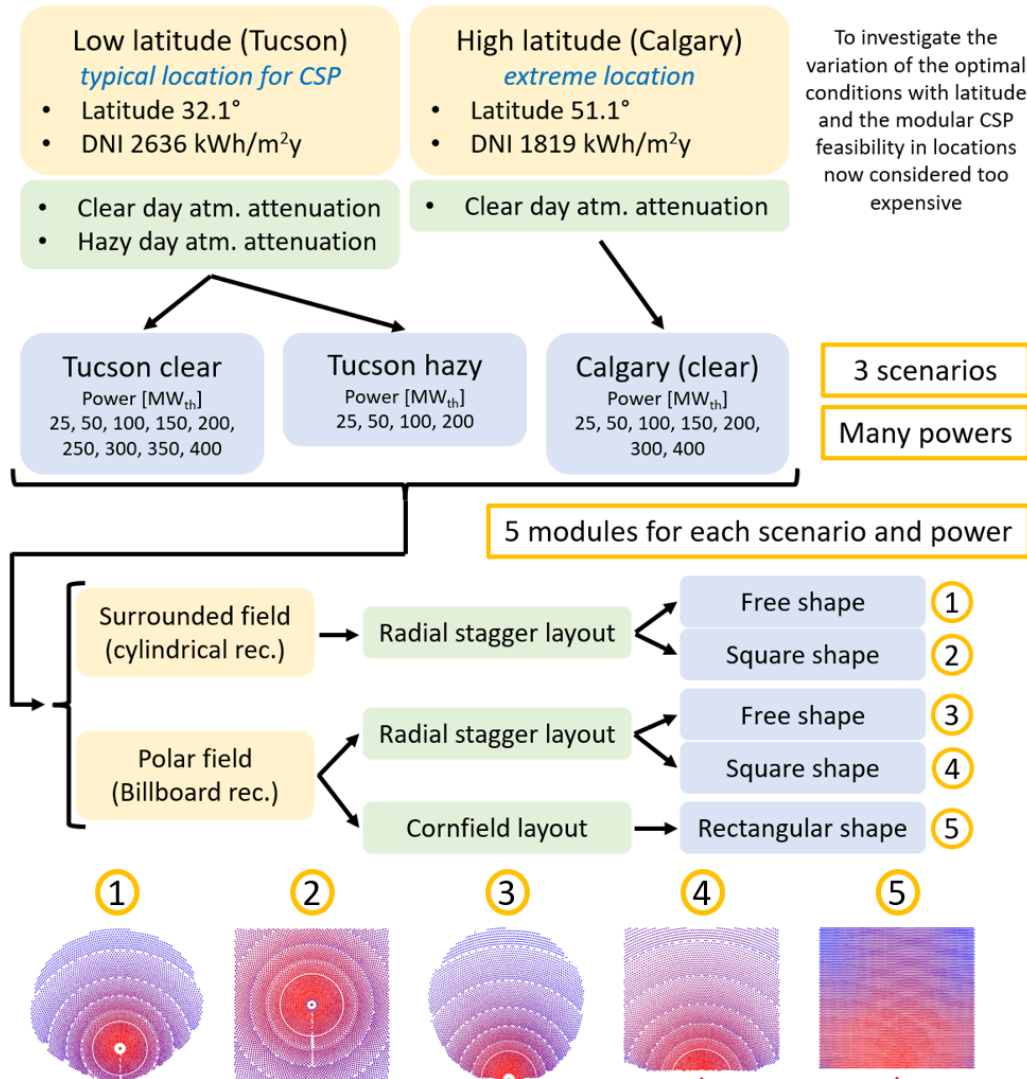


Figure 4.2: Decision tree for the cases analysed

In addition, in the most representative case under typical conditions, a study is carried out by varying the net electric power output of two modular plants up to 500 MW_{el} capacity. In fact, thanks to the modular approach it is possible to overcome the optical efficiency limit that prevents the achievement of sizes larger than 110 MW_{el} for conventional plants. With the same modules, therefore, the trade-off between piping system and power block as the installed capacity increases, both from the performance and cost perspectives, is analysed. Both the case with a 1-reheat and 2-reheats PB are studied, except for the case with 100 – 110 MW_{el} where only 1 reheat is considered since there are currently no such small cycles using 2 reheats.

Table 4.1 shows all the remaining data and assumptions for the two locations. The wind velocities, needed for the receiver's convective losses, are obtained from [83].

	Tucson	Calgary
Latitude [°]	32.1	51.1
Longitude [°]	-110.9	-114.0
Elevation [m]	779	1077
Time zone [h]	-7	-7
DNI annual [kWh/m ² /y]	2636	1819
DNI daily [kWh/m ² /d]	7.22	4.98
Average ambient T [°C]	20.1	4.0
Wind velocity [m/s]	$3.76+(H/100-1)\cdot 0.73$	$5.67+(H/100-1)\cdot 1.70$
Design DNI [W/m ²]	1000	900
Design ambient T [°C]	25	15

Table 4.1: Climatic data and assumptions for the two locations

4.2.2. Solar field

The design powers used for the modular fields are given in Table 4.2, along with the corresponding values of the side of the heliostats, which are assumed to be square in shape. As for the conventional plant, the design thermal power is set to 900 MW_{th} with 12m side heliostats in the clear sky scenarios.

Design thermal power [MW _{th}]	25	50	100	150	200	250	300	350	400
Heliostat's side [m]	2.5	3	4	5	6	7	8	9	10

Table 4.2: Design thermal power and heliostat's side of the investigated modules

Surrounded fields are associated to cylindrical receivers, while polar fields to Billboard receivers. Considering the layout of individual modules, square radial stagger modules (AR = 1) are selected due to their symmetry and simplicity, and since these would lead to more compact solar fields at the expense of an optical efficiency loss that has to be evaluated. The choice of a square rather than a rectangular shape is made as a matter of simplicity. In contrast, polar fields with cornfield layout have a rectangular shape in analogy with the modules proposed by Vast Solar [30].

About all surrounded modules, a minimum solar field radius scaled with the tower height is established, amounting to 0.25 times the tower height. This is a lower value than those found in conventional installations, however, no space is needed at the base of the tower in modular plants since the TES and PB are placed outside the boundaries of individual modules. In contrast, as for the conventional case, the minimum radius is defined as 0.75 times the tower height. The remaining parameters for defining the placement of heliostats within solar fields are defined in Table 4.3.

Radial stagger – radial spacing method	No blocking dense
Radial stagger – azimuthal spacing factor	2
Radial stagger – azimuthal spacing reset limit	1.33
Radial stagger – packing transition limit factor	1
Cornfield – heliostat spacing factor – X direction	1.1
Cornfield – heliostat spacing factor – Y direction	1.1
Cornfield – heliostat field layout shape	Rectangle

Table 4.3: Data and assumptions for the solar field layouts

The characteristic parameters of heliostats are not investigated in detail. Therefore, the SolarPILOT default values, shown in Table 4.4., are used. According to [84], the total image error is conservative, and a reduction of this parameter could lead to consistent improvements in the optical performances.

Heliostat focusing type	At slant
Total reflected image error [mrad]	3.07
Reflective surface ratio [-]	0.97
Mirror reflectivity [-]	0.95
Soiling factor [-]	0.95

Table 4.4: SolarPILOT default settings for the heliostats' design

Table 4.5 reports the input parameters selected for the design of receivers.

Billboard – aspect ratio [-]	1 [85]
Billboard – horizontal acceptance angle [°]	170
Billboard – acceptance angle shape	Elliptical
Billboard – radial stagger layouts – tilt angle [°]	-12
Billboard – cornfield layouts – tilt angle [°]	-20
Cylindrical – aspect ratio [-]	1.5 [86]
Cylindrical – horizontal acceptance angle [°]	360

Table 4.5: Receivers' input parameters in SolarPILOT

As for the design simulations, under summer solstice conditions (on June 21st), these are carried out at local time 12.425 in Tucson and 12.630 in Calgary to obtain an azimuth angle exactly equal to 180.0°. In addition, for the "image size priority" aim point method, a minimum image offset from the receiver edge of 4 in both X and Y directions is set for the Billboard receiver, while a value of 2 in Y direction is set for the cylindrical receiver. Finally, the flux map is discretized into 100 elements along both horizontal and vertical directions to obtain a detailed matrix for the receiver thermal model.

Last, regarding the off-design analysis, the azimuth angle is studied between 40° and 320° with a 20° step (assuming south = 180° in the Northern Hemisphere), and the elevation angle between 0° and 80° with a 10° step.

4.2.3. Tower, Receiver

Steel monopole towers are used up to 150m heights and conventional concrete towers beyond this value. In addition, solar salts in the traditional operating temperature range 565°C - 290°C [3] are used as HTF. Other data for the receiver model are given in Table 4.6.

Spacing between adjacent tubes [mm]	1
Tube material	Haynes 230 [87]
Tube emissivity [-]	0.87
Insulating wall emissivity [-]	0.75
Tube absorptivity [-]	0.93
Insulating wall reflectivity [-]	0.30
Sky emissivity [-]	0.895
Ground emissivity [-]	0.955

Table 4.6: Data and assumptions for the receiver thermal model

Regarding the off-design operation, the range from 20% to 120% with respect to the design flux is investigated with a 10% step. Therefore, it is considered that for fluxes lower than 20% of the design case, the HTF circulation is cut off. The same range is also used for the piping system's off-design.

4.2.4. Piping, TES

All the values characterizing the piping and TES design are given in Table 4.7.

Spacing between adjacent modules (N-S and E-W) [m]	10
Row-Tower distance, Polar fields [m]	5
Row-Tower distance, Surrounded fields [m]	5+(tower-south limit)
Distance between two adjacent expansion loops [m]	40
Distance between two adjacent ground supports [m]	20
HTF pump design hydraulic efficiency [-]	0.85
HTF pump electro-mechanical efficiency [-]	0.99
TES annual efficiency [-]	0.995
External surface temperature of tubes [°C] T. C.	30 20
Tube internal roughness [mm]	0.09 [74]
External Aluminium foil cladding emissivity [-]	0.03 [74]
SS 316 temperature expansion coefficient [$\mu\text{m}/\text{m}/\text{K}$]	16 [74]

Table 4.7: Data and assumptions for piping system and TES

4.2.5. Power block

At the inlet to the first high-pressure stage, the maximum pressure is set to 170bar for the 1 RH cycle and 190bar for the 2 RH cycle. The off-design performance is obtained at full-load as a function of the ambient temperature, which is varied from 0°C to 40°C in Tucson and from -15°C to 25°C in Calgary, with a 5°C step.

Within the analysis, the models are used to calculate the performances corresponding to the power ratings shown in Table 4.8 and in their surroundings.

1 RH cycle, cases [MW_{el}]	100	200	300	400	500
2 RH cycle, cases [MW_{el}]	-	200	300	400	500

Table 4.8: Electric power values studied with the PB models

4.3. Cost model

To perform an accurate techno-economic analysis, it is necessary to carefully evaluate the plant costs and the economies of scale. In fact, the parameter of merit is the Levelized Cost of Electricity (LCOE), consisting of the cost of generating electricity or the price at which the electricity must be sold to reach the break-even point at the end of the plant's lifetime. This is the meeting point between the technical and the economic analyses.

Some of the values used in the economic analysis are subject to a certain level of uncertainty, since for CSP technology it is very difficult to find current and realistic costs if they are needed for academic purposes. In fact, the manufacturing sector of CSP components is very closed and it is likely not to change until the technology becomes widely available.

In the present study, the selected economic currency is the USD (\$) and the main exchange rates, updated to June 2022, are set to EUR/USD = 1.10 and AUD/USD = 0.70.

4.3.1. CAPEX

The capital expenditures (CAPEX) are the direct and indirect fixed investment costs spent for the construction of the plant. Direct costs include all the tangible assets (land, components, auxiliary systems) that need to be purchased or built to complete the plant.

Land purchase and site improvements

The specific cost of land purchase is set to 2 \$/m². Indeed, large-scale CSP plants are often built in mostly uninhabited and desert locations, where the land has little value. This cost is in line with literature, such as in [88] and [89]. SAM (System Advisor Model) [88] is a free techno-economic software, provided by NREL [64], that facilitates decision-making in the renewable energy industry, so it turns out to be an authoritative source in this field.

Regarding site improvements, namely the expenses related to site preparation and other equipment not included in the cost of heliostats, a cost per square meter of total reflective area is assumed equal to 16 \$/m²_{hel}. This value coincides with [88] but also falls within the range identified in [90].

Heliostats

The specific cost of mirrors, usually given as cost per unit reflective area, is set to 100 \$/m²_{hel}. This value is slightly lower than those commonly used in previous CSP studies. However, considering both the continuing technological advances and the possibility that prices will be further reduced by a large-scale deployment of CSP technology in the coming years, it seems an appropriate value with a view to the future. Also, similar values already appeared in the recent literature. Some examples are [91] (2017), which states that "commercial suppliers of heliostat technologies are now claiming costs around 100 \$/m²_{hel} or even around 75 \$/m²_{hel}", [92] (2020) which uses a cost equivalent to 90 \$/m²_{hel}, [46] (2021) which sets it at 100 \$/m²_{hel}, while [93] (2021) assumes a cost of 100 €/m²_{hel}.

Tower

The cost of each tower is expressed through correlations as a function of the height. In fact, as the height increases, the construction materials required increase linearly, but the complexity of working and bringing them to height grows more than linearly.

Normally, the towers of conventional plants are built of concrete, having considerable heights (even more than 200m) and supporting the weight of large receivers. For such towers, a cost function is proposed by NREL in both its software (SolarPILOT [61], SAM [88]). The equation is a function of the tower height in m and provides a cost in M\$:

$$Cost_{tower} = 3 \cdot e^{0.0113 \cdot H_{tower}}$$

The use of steel monopole towers derived from wind turbines is chosen in this thesis for lower heights. More specifically, steel monopole towers are employed up to 150m, and

concrete towers above. This value is chosen by looking both at currently existing plants adopting such technology, and at the state-of-the-art of onshore wind turbines. Finally, the steel monopole solution is preferred over the steel lattice one because of the more promising heights and the already wide development in the same sector of CSP, the one of renewable power generation. The correlation, used to evaluate the costs of the steel monopole technology and expressed as a function of the tower height in m and providing a cost in M\$, is established in [94] and represents the complete investment cost of the tower construction plus foundations and transport, considering larger diameters providing enough space for the piping and the receiver. The height range for the correlation is from 50m to 200m, even if in the study it is set conservatively up to 150m.

$$Cost_{tower} = 1.50227 - 0.00879597 \cdot H_{tower} + 0.000189709 \cdot H_{tower}^2$$

In Figure 4.3, the trend of the two cost functions as the tower height varies, each one in the domain established by the assumptions, can be observed.

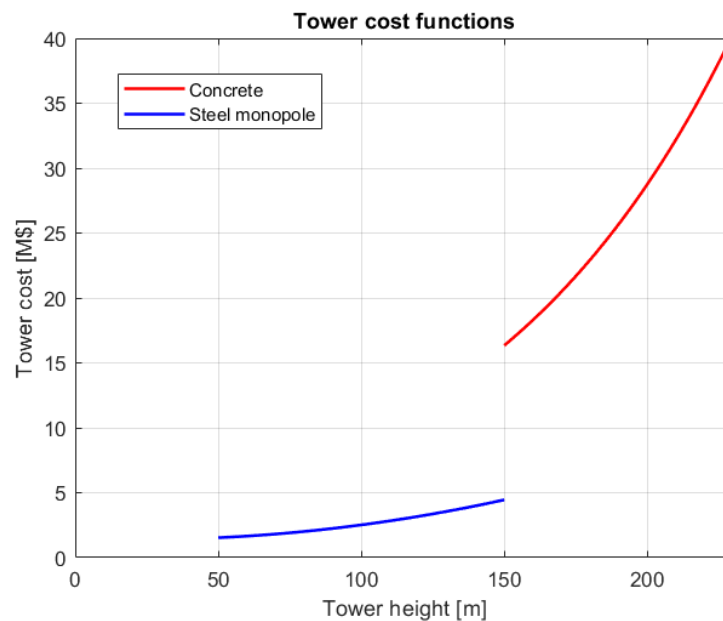


Figure 4.3: Cost functions for the towers

Receiver

The receiver cost is also evaluated through cost functions. The benchmark is the outer receiver's surface area, thus the set of panels hit by the heat flux from the solar field. The receiver's surface allows for the evaluation of size-dependent economies of scale through a cost scaling exponent typically equal to 0.7 [61], [88]. In the present analysis, two different

cost functions are used depending on whether the receiver is cylindrical or Billboard. This subdivision is necessary because of the reduced construction and assembly complexity of Billboard receivers, which require reduced panel support structures compared to cylindrical ones. As for the cylindrical receiver, the use of a cost function proposed by NREL in both SolarPILOT [61] and SAM [88] is chosen. The cost is expressed in M\$ while the external area of the receiver in m^2 .

$$Cost_{rec} = 103 \cdot \left(\frac{A_{rec}}{1571} \right)^{0.7}$$

For the Billboard receiver, no cost function is found in literature because of the limited commercial deployment of this technology. Therefore, the results set out in [45] for a cavity receiver (similar construction to the Billboard one except for the cavity, which does not represent a significant cost share) are used, adding an exponent of 0.7 to keep the same scaling effect as a function of the external surface and the consistency with the cylindrical case. In the obtained equation, the cost is expressed in M\$ while the outer surface in m^2 .

$$Cost_{rec} = 16.3 \cdot \left(\frac{A_{rec}}{137.6} \right)^{0.7}$$

In Figure 4.4, it is possible to observe the trends of the two cost functions as the external surface varies, over a range wide enough to contain all the cases analysed.

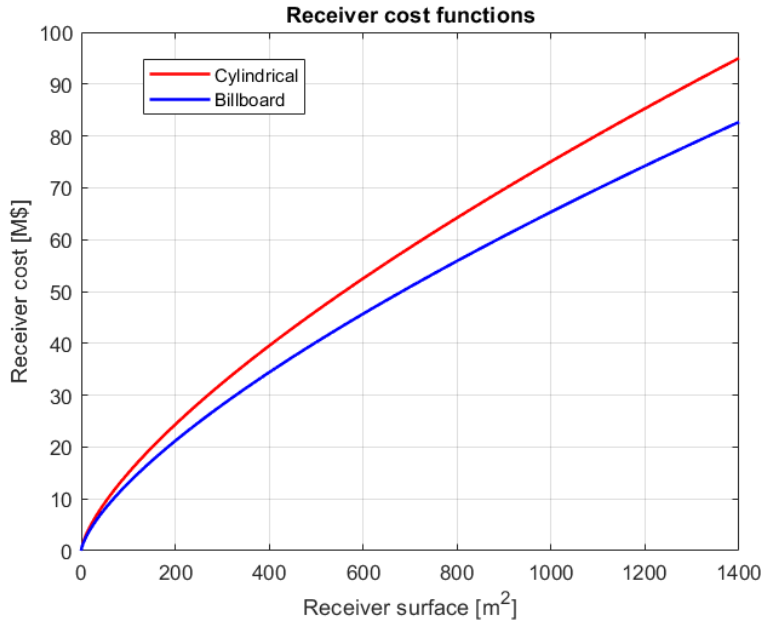


Figure 4.4: Cost functions for the receivers

Piping system

The piping system costs are derived through a bottom-up approach from the model built on Matlab, which includes several cost items for the different components.

- The cost of the materials is evaluated from the total volume of steel and insulation, using the specific costs reported in [76]: 48000 \$/m³ for SS 316, 110 \$/m³ for mineral fiber 1, 60 \$/m³ for mineral fiber 2.
- The cost of pressure control valves is assumed to 1000 \$ each.
- The HTF cost is computed from the total amount of salts needed in the piping, considering a specific cost of 0.5 \$/kg as in [95].
- The cost of pipes' supports from the ground is computed from the correlation developed in [96] in \$, while the steel pipes' outer diameter is in m.

$$Cost_{support} = 630.4 \cdot \ln(D_{out} \cdot 39.37) - 482.25$$

Therefore, the total direct cost of the piping system is:

$$Cost_{pip} = \sum_i^{material} C_i \cdot V_i + Cost_{valve} \cdot N_{valves} + Cost_{HTF} \cdot \rho_{HTF} \cdot V_{in,pip} + Cost_{tot,supp}$$

Thermal energy storage

The TES cost is assumed in relation to the maximum storage capacity through a specific cost of 22 \$/kWh_{th} stored, a value used in [88], [93] and [97]. This cost includes two tanks, HTF pump, electrical heaters, and salts needed as storage media (while the HTF is already included in the piping costs).

Power block

The PB cost is calculated using the same procedure proposed in [81]. In fact, Thermoflex has a wide database of components, PEACE. The PB cost is obtained as the sum of all the components (heat exchangers, pumps, air condenser, pipes, steam turbine) and is related to the site improvements, labour, installation, and components themselves. However, the results are low with respect to the literature. Hence, an additional multiplier equal to 1.49 is needed to align the results with those obtained in the last SAM update [98], which is considered a reliable reference. This way, the economies of scale are maintained as a function of the electric power, while the specific cost is consistent with literature.

Grid connection

Grid connection costs are estimated from [99], based on costs for plants in Italy. The cost is expressed in M\$, while P_{max} is in kW and L_{line} in km.

$$Cost_{connection-MV/HV} = 4 \cdot P_{max} + 7.5 \cdot P_{max} \cdot L_{line} + 6000$$

This equation provides the total connection cost of a new overhead transmission line from the plant to the closest medium-to-high voltage substation. The choice to investigate an overhead transmission line rather than an underground line is made because the former is more common and cheap, avoiding the excavation works for the entire distance, and because the plants under analysis are often located in almost uninhabited and desert locations where the presence of overhead lines is not an issue. In addition, the connection of such plants to LV/MV substations is excluded because large scale power plants need a high voltage to reduce the transmission losses. The total connection costs, shown in Figure 4.5, grow linearly with both installed power and the distance between the plant and the nearest MV/HV substation.

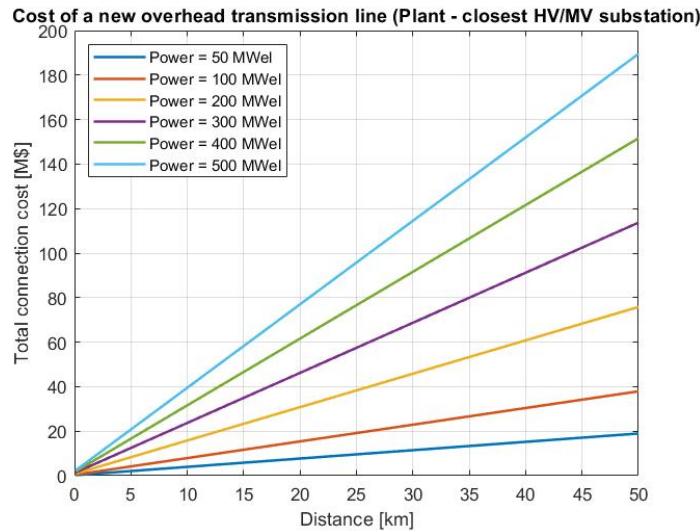


Figure 4.5: Cost of a new overhead transmission line as a function of the power and the distance from the closest MV/HV substation

In this thesis, plants built from scratch at the same time are considered. Consequently, also the transmission lines are built from scratch. Then, for the purpose of comparing modular and conventional plants, the absolute distance between plant and substation is not of interest since both the plants would still be built in the same location, the only interest being in the total costs compared to those of the plants. From the equation, the

cost of building two separate lines carrying a given power is almost identical to the cost of building a single line carrying twice that power. Building two separate lines does not affect costs more than a single line carrying twice as much power, since the latter would have larger diameter cables, more effective electrical insulation systems, and possibly higher trellises. Therefore, for the same transmission line's length and total electric power to be transported, building from scratch a modular plant or several conventional plants, whether these have one transmission line each or are unified near the plants into a single line, does not cause significant cost differences. Moreover, assuming an average line length of 20km, connection costs result 154 $\$/kW_{el}$ regardless of the power rating, a small value compared to the overall specific costs of a CSP plant. Therefore, given the irrelevance of the grid connection within the comparison between modular and conventional plants, and given the low specific cost value compared to the plant costs, these costs are incorporated within the Balance of Plant cost item, described in the next section.

Direct costs

Direct costs consist in the sum of all the costs of the individual components, to which are added the Balance of Plant costs (BoP). BoP costs represent the expenses related to the supporting components, auxiliary systems, and controls of the plant such as transformers, inverters, switching and control equipment, protection equipment, power conditioners, buildings and supporting structures. In the present study, the cost of BoP is assumed 290 $\$/kW_{el}$ as in [88].

Indirect costs

Indirect costs consist of all investment costs not defined as direct, thus not falling into the categories of components, systems, equipment, and buildings. They include design and installation, insurance, owner and contingency costs. In this thesis, the total indirect costs are assumed 20% of direct costs. In any case, for the purpose of comparing modular and conventional plants, a too accurate choice of this value is not relevant.

4.3.2. OPEX

Operating expenditures (OPEX) consist in the operation and maintenance costs of the plant (O&M), hence the costs that an operator faces for equipment and services after that the system is installed (during the plant's lifetime). These are divided into fixed O&M, proportional to the system's rated capacity in kW_{el} , to be faced each year regardless of the production, and variable O&M, specific to the MWh_{el} produced, which are proportional to the annual electricity production. In the present study, fixed O&M of 65 $\$/kW_{el}y$ and

variable O&M of 3.5 \$/MWh_{el} are assumed, in line with the values used in SAM's cost model [88]. The equation for the total annual O&M costs is reported, where P_{nom} is in kW_{el}, AEP in MWh_{el}, and the cost in \$.

$$OPEX = O\&M_{fix} \cdot P_{nom} + O\&M_{var} \cdot AEP$$

4.3.3. LCOE

The Levelized Cost of Electricity (LCOE) consists of the average net present cost of electricity generation over the lifetime and is an excellent indicator to evaluate and compare power plants from a techno-economic perspective. To properly evaluate the LCOE, it is first necessary to establish a discount rate d (or interest rate), which is the measure of the time value of money expressed as an annual percentage, that allows to annualize costs. From the many values in literature, a conservative discount rate of 8% on an annual basis is assumed. In addition, a plant's lifetime L of 30 years is also assumed (higher than the usual 25 years employed in many analyses, with a view to future technological advances and greater reliability of components), while the effect of inflation is neglected. However, the accurate choice of these values are of little relevance for the purpose of comparing modular and conventional plants.

From these, it is possible to compute the dimensionless Capital Recovery Factor (CRF), defined as the ratio of a constant annuity to the present value of receiving that annuity for a given period, allowing the CAPEX to be annualized over the entire lifetime. This factor is calculated as:

$$CRF = \frac{d \cdot (1 + d)^L}{(1 + d)^L - 1}$$

It is finally possible to compute the LCOE, expressed in \$/MWh_{el}, from the economic values of CAPEX, OPEX, and CRF, and from the AEP provided by the annual plant's performance analysis, assuming no degradation. The simplified equation employed is:

$$LCOE = \frac{CAPEX \cdot CRF + OPEX}{AEP}$$

4.3.4. LCOH

In addition to the LCOE, in the present study it is also necessary the use of a less common parameter. The Levelized Cost of Heat (LCOH), expressed in \$/MWh_{th}, allows the calculation of the heat production cost at the outlet of the receiver, thus without

considering the piping system and all the components downstream, but including the HTF pump's equivalent thermal power consumption to overcome the receiver pressure losses. This parameter is particularly useful in the modular analysis because it allows for a quick comparison of the performances of modules, which may have different geometries and technologies, avoiding the LCOE calculation, since the downstream components are the same. However, the piping configuration depends on the size of the modules, so it is necessary to adopt some tolerance on the LCOH results, although the piping system has little weight within the cost breakdown of CSP plants. In practice, should it turn out that the LCOH of a module A is just slightly lower than the LCOH of a smaller module B with the same power output, then it would be wrong to discard module B in advance, and a LCOE analysis would be needed. In the present study, all the assumptions and cost functions adopted in the LCOE calculation are also used for the LCOH, the only differences being that:

- Direct costs only include land, site improvements, heliostats, tower, and receiver.
- O&M are not included, because of their plant-level values referred to the PB (nominal capacity and AEP) that lead to the impossibility to estimate the O&M cost share attributable to the considered components only. However, this does not invalidate the results, since the goal of the LCOH is to allow for a comparison between modules to support decision making, without any claim to be accurate in absolute terms.

In similarity to the LCOE, the LCOH is calculated through the following equation:

$$LCOH = \frac{CAPEX \cdot CRF}{AHP}$$

where AHP is the annual heat production before the piping system, in MWh_{th} .

5 | Results and discussion

After describing the models of all components, the methodology, and both technical and cost data and assumptions, it is finally possible to comment on results.

5.1. Billboard discretization

For the Billboard receiver with 2 flows and 2 panels per flow, an aspect ratio $AR = 1$ is used with sodium as HTF in the $730^{\circ}\text{C} - 550^{\circ}\text{C}$ temperature range and the same heat flux map for all cases. The results are shown in Figure 5.1, while the other field parameters are not relevant for the purpose of this study.

1m x 1m						4m x 4m						7m x 7m						
η [%]	Ns					η [%]	Ns					η [%]	Ns					
	1	2	3	4	5		1	2	3	4	5		1	2	3	4	5	
N _{ax}	1	84.01%	83.89%	84.01%	84.02%	84.01%	1	86.52%	86.28%	86.39%	86.41%	86.40%	1	87.25%	86.87%	86.97%	86.97%	86.96%
	10	83.97%	83.89%	84.02%	84.04%	84.04%	10	86.51%	86.27%	86.39%	86.41%	86.40%	10	87.22%	86.84%	86.94%	86.95%	86.93%
	50	84.02%	84.06%	84.22%	84.26%	CRASH	50	86.52%	86.33%	86.46%	86.48%	86.48%	50	87.22%	86.86%	86.98%	86.99%	86.98%
	200	84.11%	84.26%	CRASH	CRASH	CRASH	200	86.55%	86.49%	86.65%	86.68%	86.68%	200	87.22%	86.96%	87.09%	87.11%	87.11%
	1000	84.19%	CRASH	CRASH	CRASH	CRASH	1000	86.71%	86.80%	CRASH	CRASH	CRASH	1000	87.31%	87.25%	87.43%	CRASH	CRASH
	5000	CRASH	CRASH	CRASH	CRASH	CRASH	5000	86.90%	CRASH	CRASH	CRASH	CRASH	5000	87.63%	CRASH	CRASH	CRASH	CRASH
10m x 10m						13m x 13m						16m x 16m						
η [%]	Ns					η [%]	Ns					η [%]	Ns					
	1	2	3	4	5		1	2	3	4	5		1	2	3	4	5	
N _{ax}	1	86.35%	86.11%	86.24%	86.25%	86.24%	1	87.32%	86.94%	87.05%	87.05%	87.04%	1	87.34%	86.79%	86.88%	86.87%	86.85%
	10	86.33%	86.09%	86.22%	86.23%	86.22%	10	87.30%	86.92%	87.02%	87.03%	87.01%	10	87.30%	86.75%	86.83%	86.83%	86.80%
	50	86.33%	86.12%	86.25%	86.27%	86.26%	50	87.29%	86.92%	87.04%	87.04%	87.03%	50	87.30%	86.75%	86.84%	86.84%	86.82%
	200	86.35%	86.20%	86.35%	86.38%	86.38%	200	87.29%	86.98%	87.11%	87.12%	87.11%	200	87.29%	86.79%	86.89%	86.89%	86.87%
	1000	86.44%	86.46%	86.64%	CRASH	CRASH	1000	87.33%	87.19%	CRASH	CRASH	CRASH	1000	87.27%	86.95%	87.10%	87.11%	CRASH
	5000	86.65%	CRASH	CRASH	CRASH	CRASH	5000	87.57%	87.60%	CRASH	CRASH	CRASH	5000	87.52%	87.43%	87.60%	CRASH	CRASH

Figure 5.1: Analysis of the discretizations of the Billboard receiver's model

To get results without strong oscillations, it is necessary to set $N_s \geq 3$ ($N_c \geq 12$) while the performance only increases as N_{ax} grows until the model crashes. It becomes less likely that the model crashes as the receiver's absolute size grows. As a safety threshold for the model not to crash and for accurate results to be obtained, the axial discretizations must have a minimum absolute size given by $H_{rec} / N_{ax} = 5\text{mm}$ providing reasonable computational times, while concerning the circumferential discretizations $N_s \geq 3$ is needed. However, the model's maximum error, that is the difference between the efficiency obtained with this criterion and the one without discretizations ($N_{ax} = 1$, $N_s = 1$), is lower

than 0.5% for all sizes.

5.2. Vast Solar modules

This study allows to verify the proper functioning of the models and to highlight some relevant technical aspects and trade-offs within the analysis and optimization of CSP plants. The assumptions and the numerical results obtained are not reported, being outside the scope of this thesis.

5.2.1. Optical efficiency maps

The difference in the optical efficiency maps between a cornfield and a radial stagger polar field is shown. These represent the optical performance of the solar field as a function of the azimuth angle and the elevation angle, used in the annual analysis. In Figure 5.2, beyond the higher optical efficiency of individual modules compared to the conventional field due to the smaller size, the cornfield layout causes strong anomalies in the optical performance for low elevation angles, in contrast to the homogeneous map obtained for the radial stagger configuration.

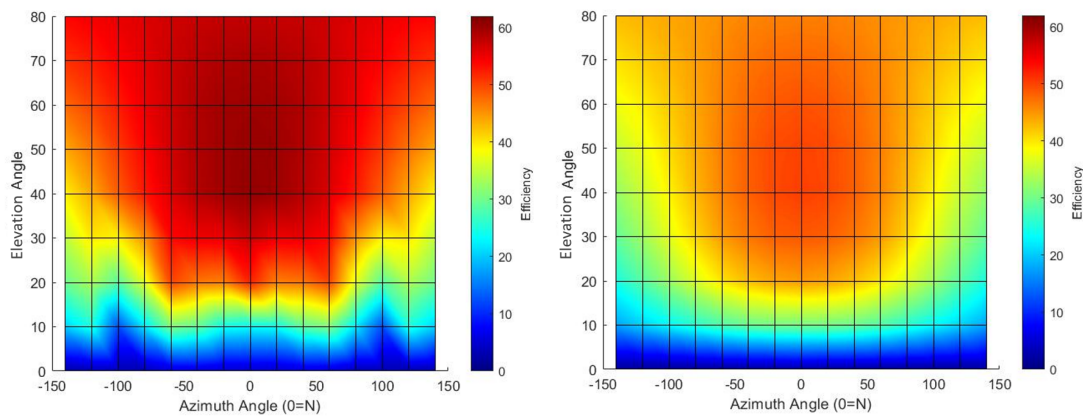


Figure 5.2: Optical efficiency maps for cornfield modules (left) and radial stagger field (right)

This is due to the relevant shading effect between rows of aligned heliostats when the azimuth is around $\pm 90^\circ$ – 100° at low elevation, representing a significant limitation of cornfield layouts. This condition is represented in Figure 5.3.

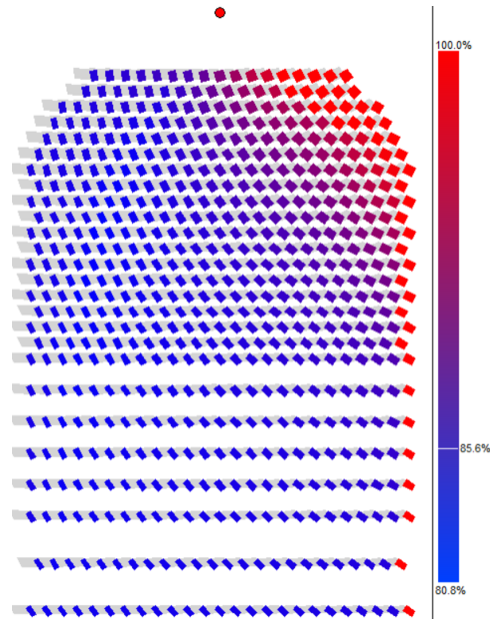


Figure 5.3: Shading effect in cornfield layouts with azimuth angle equal to 90° and low elevation angle

5.2.2. Receiver tubes diameter optimization

As shown in Figure 5.4 for two square Billboard receivers (0.89m side for modular fields and 4.65m for the conventional field), there is always an efficiency maximum when combining the thermal performance and pumping consumption, due to distributed pressure losses.

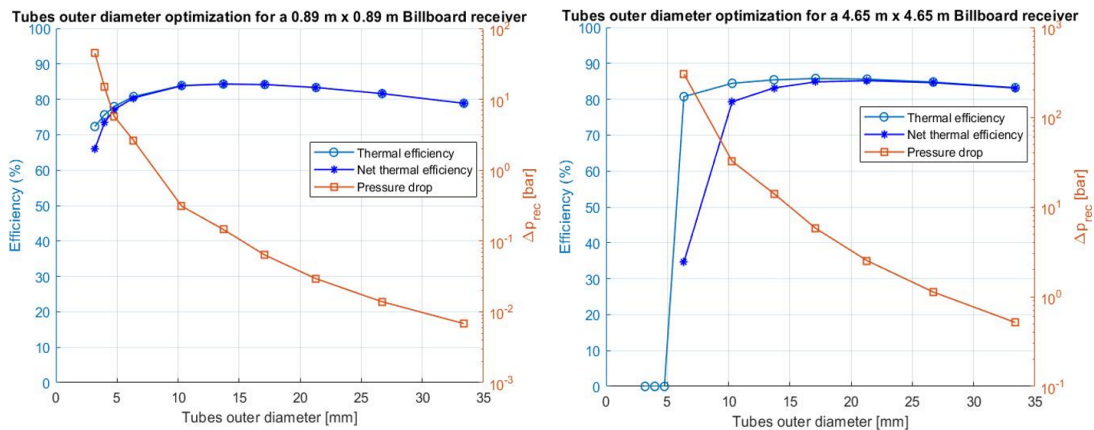


Figure 5.4: Receiver tubes' outer diameter optimization for a 0.89 x 0.89 m (left) and a 4.65 x 4.65 m (right) Billboard receiver

From the thermal perspective, at constant spacing between two adjacent tubes, smaller

tubes reduce the total useful surface area for the radiation absorption, while causing a higher HTF velocity and thus increasing the heat transfer coefficient by forced convection, providing more power to the fluid. Conversely, larger tubes increase the useful absorption area, but they worsen the convective heat transfer with the HTF. The distributed pressure losses lead to an increase in the HTF pump's power consumption, which is divided by a reference PB and piping efficiency to get the thermal losses equivalent to the electric consumption. As the diameter of the pipe increases, the HTF velocity decreases quadratically and the distributed pressure losses decrease in turn with the square of the velocity, in the case of turbulent regime where the friction factor does not depend on the Reynolds number. Therefore, especially for small pipes, a small increase in the diameter leads to a significant reduction in the pressure losses, following a polynomial of degree 4. Thus, the need for the optimization of the receiver tubes' diameter is explained.

5.2.3. Receiver size optimization

Although the maximum allowable flux on the outer wall of a sodium receiver can reach 2 MW/m^2 as in [85], this does not imply a maximum in the module's performance or a minimum in the LCOH. As shown in Figure 5.5 and Figure 5.6, for different tower heights, the combined efficiency decreases in both the modular and the conventional case with an increasing peak flux. This is because the increase in the efficiency of a high-flux receiver is lower than the increase in the spillage losses since, reducing the receiver's size with the same heliostats, part of the images of mirrors no longer hits the receiver. Also, the LCOH in the modular case has a minimum around $1 - 1.1 \text{ MW/m}^2$. This means that the cost reduction due to a smaller receiver is not enough to justify pushing the thermal flux to the maximum allowable. In contrast, for the single field, the minimum LCOH corresponds to the maximum flux due to the greater absolute variation in the receiver size, and thus in costs.

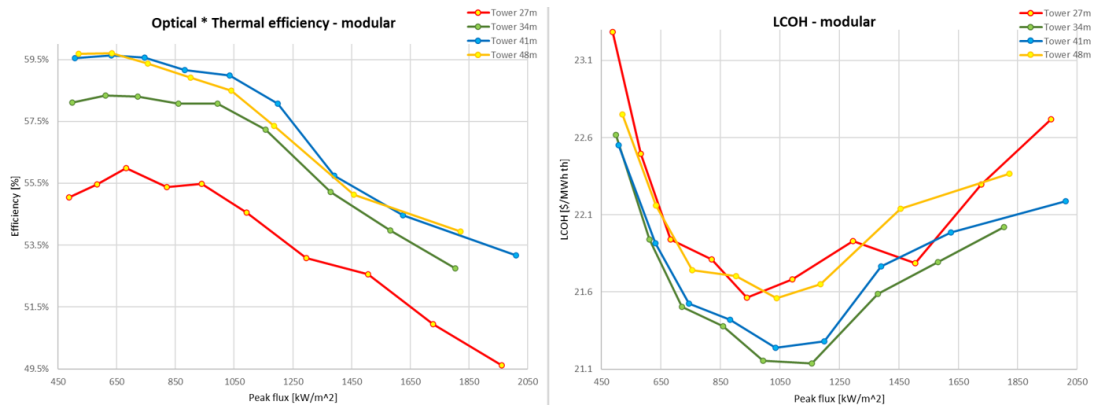


Figure 5.5: Design combined efficiency and LCOH as a function of the peak flux, at different tower heights, for the modular plant

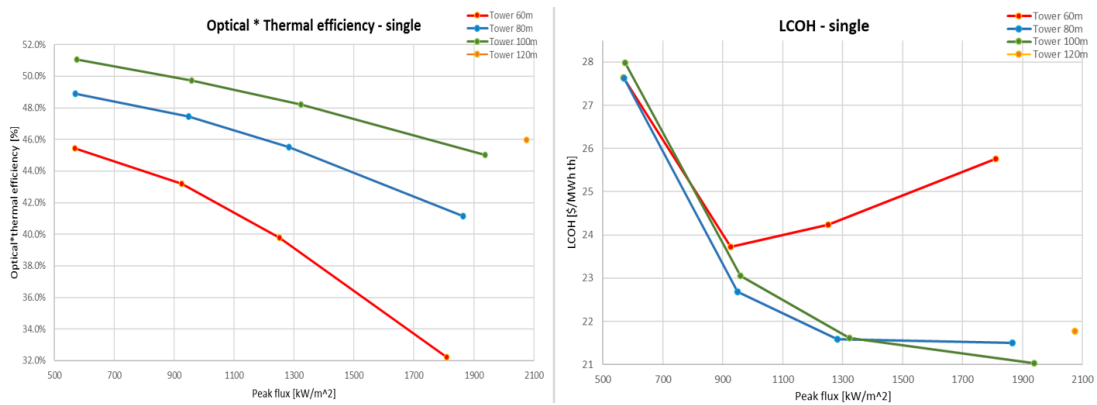


Figure 5.6: Design combined efficiency and LCOH as a function of the peak flux, at different tower heights, for the conventional plant

In conclusion, not always the maximum allowable flux on the receiver leads to the optimal configuration from a techno-economic perspective, thus it is necessary to investigate this trade-off in the case of small modules and high peak fluxes.

5.3. Large scale modular plants

In this section, the results of the main case study are presented for the three scenarios of Tucson clear, Calgary, and Tucson hazy.

5.3.1. Tower location in surrounded modules

The results of the tower location optimization are reported for Tucson clear and Calgary for both square and free modules.

Square-shaped modules

An example of the configurations analysed for 25 MW_{th} square surrounded modules, along with the respective flux maps on the cylindrical receiver's surface, is shown in Figure 5.7 for Tucson and in Figure 5.8 for Calgary. The tower location in surrounded modules is optimized as a function of the ratio y/Y between the distance from the tower to the field's south side (y) and the total North-South extension of the module (Y). Figure 5.9 shows the trends of the main field parameters in the two locations, as the position of the tower changes. The efficiencies are those of the design case.

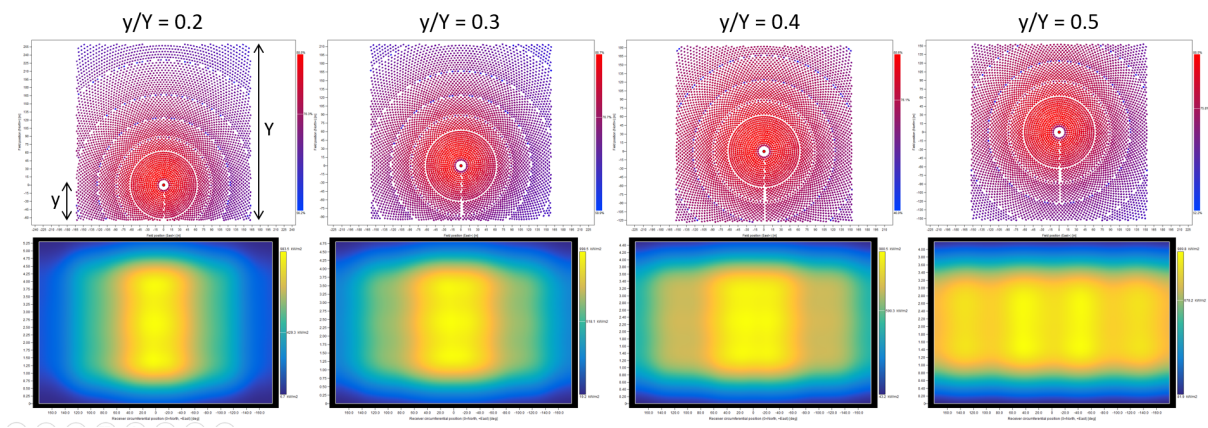


Figure 5.7: Field layout and receiver flux map as a function of the tower location, for square surrounded modules in Tucson

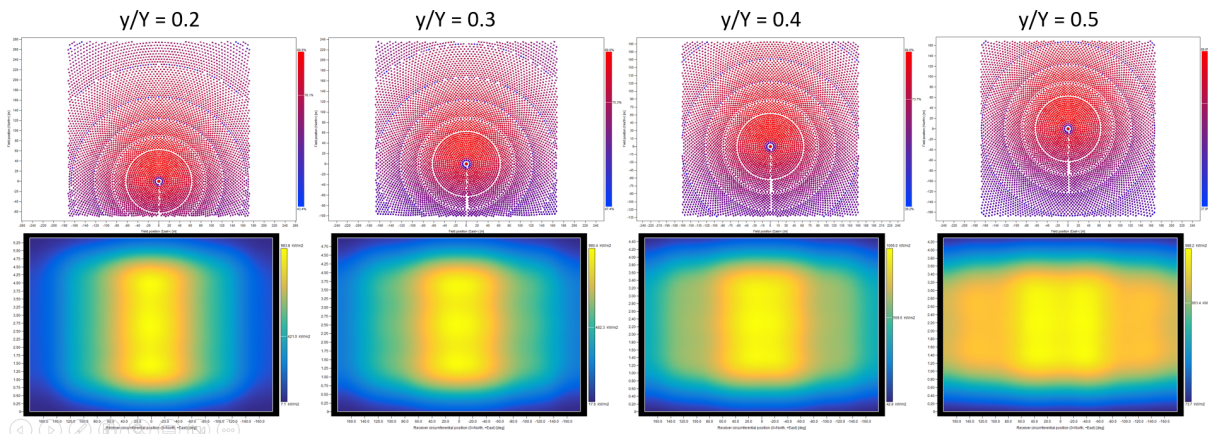


Figure 5.8: Field layout and receiver flux map as a function of the tower location, for square surrounded modules in Calgary

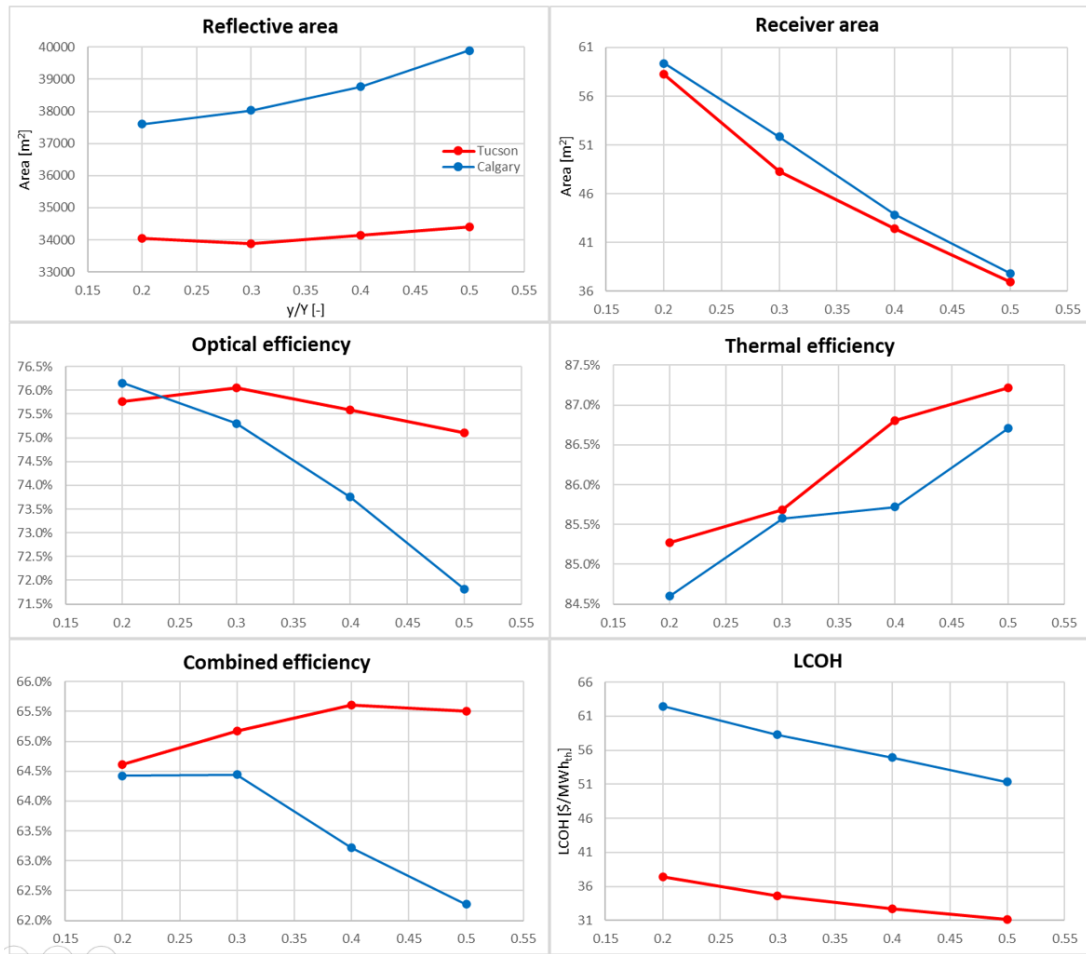


Figure 5.9: Reflective area, receiver area, optical efficiency, thermal efficiency, combined efficiency and LCOH, as a function of the tower location in square surrounded modules in Tucson (red) and Calgary (blue)

For the same thermal power, both the heliostat field and the receiver are smaller in Tucson, resulting in lower costs, as seen from the LCOH. The heliostat field has a smaller reflective area because of the higher DNI under design conditions that is experienced in Tucson. The lower receiver size in Tucson, on the other hand, is due to the higher average flux because of the greater elevation angle of the sun, for the same tower position. This reduces the difference in the power delivered to the receiver between the heliostats to the south and those to the north of the tower, allowing for a more homogeneous and a higher average flux. For example, the average flux at Tucson with the tower in the middle of the field ($y/Y = 0.5$) is 678 kW/m^2 , while at Calgary it is 661 kW/m^2 . The decreasing trend in the receiver size by moving the tower toward the centre is also due to the average flux increase, caused by the greater balance in the number of mirrors around the tower.

Turning to efficiencies, the optical efficiency has a maximum for $y/Y = 0.3$ in Tucson

and for $y/Y = 0.2$ in Calgary, mainly due to the cosine efficiency, which is heavily influenced by latitude. Moving to higher latitudes makes the mirrors to the south of the tower progressively less convenient than those to the north. In practice, the increase in cosine efficiency of the mirrors to the north more than compensates for the reduction in attenuation and spillage efficiencies that occurs by placing them farther from the tower, resulting in more unbalanced fields. Because of the average flux increase obtained by placing the tower in the centre of the field, the thermal efficiency trend is increasing. The combined efficiency is the result of a trade-off between these two aspects. On the one hand, unbalanced fields allow higher optical efficiencies because of the cosine effect. On the other hand, balanced fields allow higher thermal efficiencies because of the high average flux. Thus, the maximum combined efficiency stands at $y/Y = 0.4$ in Tucson and $y/Y = 0.3$ in Calgary, and the difference is due to latitude.

Integrating performances with costs yields that the optimal modules from the LCOH perspective are always those with the tower located in the centre ($y/Y = 0.5$). In fact, although this configuration reduces the combined efficiency by 0.1% in Tucson and by 2.2% in Calgary with respect to the maximum value, it simultaneously allows for a great reduction in the receiver area (12% in Tucson and 27% in Calgary) with a minimal increase of the reflective area.

The results determine the choice of square modules with towers placed exactly in the middle in both Tucson and Calgary. Such modules also allow for the minimum land consumption since the heliostats are on average closer to the tower and therefore closer to each other. They also allow for greater construction simplicity due to the field's symmetry. Generalizing this result:

- Plants at lower latitudes than Tucson always provide a centrally located optimal tower, since at low latitudes the cosine effect is further reduced, and this is the only factor that shifts the optimal layout toward unbalanced fields.
- Plants at latitudes between Tucson and Calgary have a centrally located optimal tower, since this is true for Calgary where the latitude is very high.
- Currently, there is no plant, either operational or under construction, at latitudes higher than Calgary because of the low DNI and the strong yearly unbalance between hours of light and darkness.

It is therefore concluded that, as far as square-shaped modules are concerned, it is always convenient to place the tower in the centre of the module leading to symmetrical and balanced fields, since the cost effect given by the average flux increase outweighs the

benefit provided by the cosine losses reduction.

Free-shaped modules

The same procedure is also applied to the free-shaped surrounded modules by gradually varying the maximum radius from the tower at which heliostats can be placed. Starting from the default (unconstrained) configuration provided by SolarPILOT, more balanced fields are obtained by decreasing the field's maximum radius. Figure 5.10 shows an example for a 25 MW_{th} module in Tucson, however this procedure is applied to every power size and scenario analysed in the study.

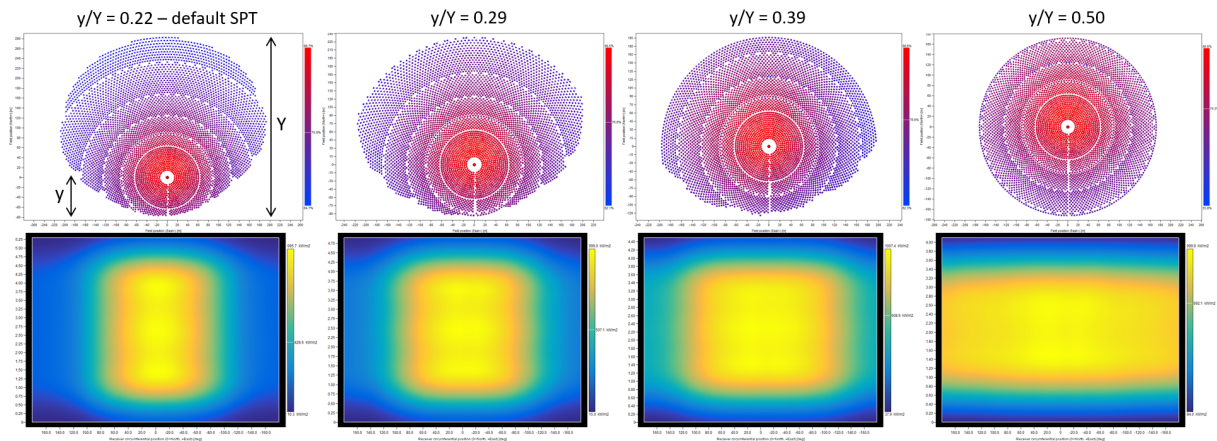


Figure 5.10: Field layout and receiver flux map as a function of the tower location, for free surrounded modules in Tucson

First evidence is that the shape of the unconstrained field, given the same mirror's size, strongly depends on the maximum flux allowed on the receiver surface. Figure 5.11 shows the comparison between two 25 MW_{th} modules in Tucson: the first employs solar salts with a maximum flux of 1 MW/m^2 , the second employs liquid sodium, which allows for 2 MW/m^2 , in a similar temperature range ($585^\circ\text{C} - 310^\circ\text{C}$).

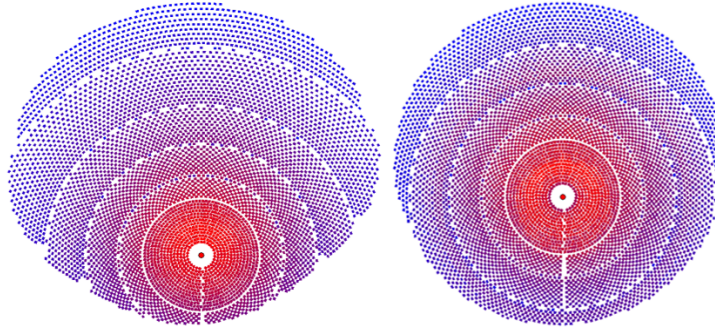


Figure 5.11: Field layout of 25 MW_{th} free surrounded modules with 1 MW/m² maximum heat flux (left) and 2 MW/m² maximum heat flux (right), in Tucson

For the same desired power, as the maximum flux increases, the receiver size is reduced. Because of this reduction, the spillage losses of the most distant mirrors (north of the tower) increase. When this increase exceeds the increase in cosine losses from placing those heliostats south of the tower, the mirrors are shifted from north to south, making the field more balanced. This explains why SolarPILOT, which aims to maximize the optical performance only, automatically generates very unbalanced fields using a peak flux of 1 MW/m².

Figure 5.12 shows the trend of combined efficiencies of each module's size as a function of the tower location. The values in Tucson are higher than those in Calgary, which confirms the better performance of surrounded fields at low latitudes. Moreover, the combined efficiency decreases as the size of the modules increases, which is due to the overall reduction in their optical performance.

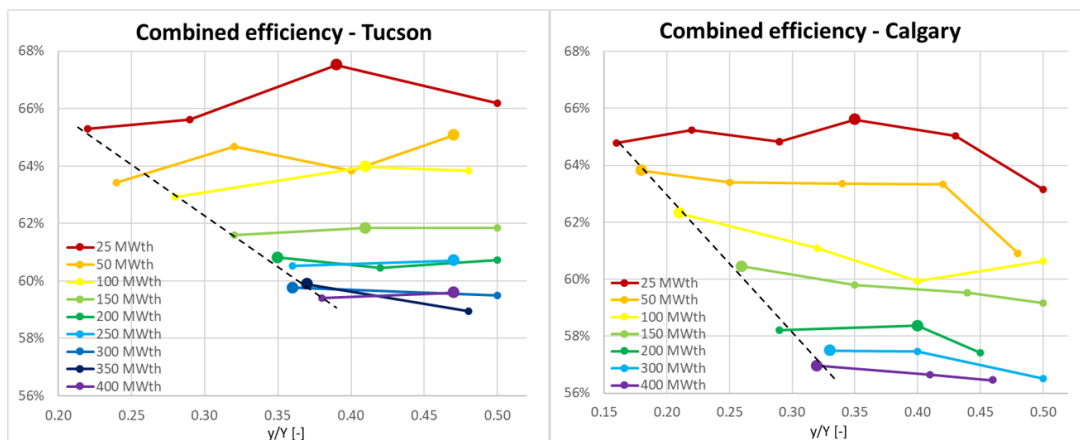


Figure 5.12: Combined efficiency at design conditions as a function of the tower location, for different modules' sizes in Tucson (left) and Calgary (right)

For each size, the configurations along the black dashed line are the unconstrained fields generated by SolarPILOT, while in the rightmost ones the tower is in the centre of the field. As the size grows, SolarPILOT generates increasingly balanced fields. This is due to the trade-off between cosine efficiency, which leads to a preference for mirrors north of the tower in the northern hemisphere, and spillage and attenuation losses, which increase significantly as the distance of the mirrors from the receiver grows. By increasing the size, therefore, it no longer pays to place many heliostats north of the tower. Placing them south, despite the cosine efficiency reduction, leads to higher performances. In practice, the trade-off between cosine efficiency on the one hand and spillage and attenuation efficiencies on the other, determines the shape of the field and depends on the nominal power and the maximum flux on the receiver, given the same heliostats' size.

A further consideration consists of the tower location to which the thermodynamic optimums for each module correspond. Beyond the discontinuities, mainly due to the heliostats' sizes and the discretized optimization of the receiver tubes' diameter, the optimal tower locations at Tucson are all between $y/Y = 0.35$ and 0.47 , while at Calgary this occurs between 0.18 and 0.40 . This confirms the similar result obtained for square surrounded modules. The thermodynamic optimum is around $y/Y = 0.4$ in Tucson and $y/Y = 0.3$ in Calgary, and this difference is because of latitude.

As for square modules, however, the LCOH analysis also demonstrates that the most cost-effective configurations are the ones with the tower in the middle of a circular module ($y/Y = 0.5$) because of the significant receiver's size and cost reduction. Again, this is expected to be the best configuration at any latitude at which a CSP plant can be built.

5.3.2. Modules

It is now possible to investigate in detail all the modules involved in the study.

Tower height

To reduce the number of simulations, the tower height is optimized through the LCOH for Tucson clear, and the results, shown in Figure 5.13, are then applied to the other cases.

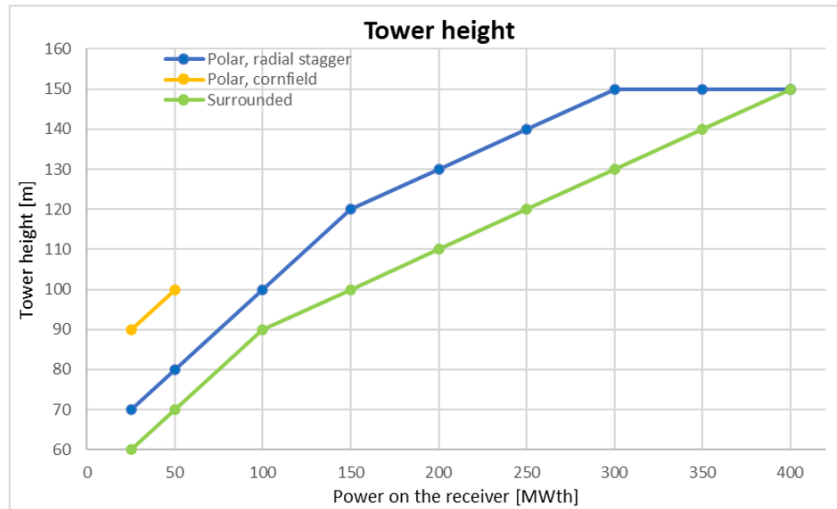


Figure 5.13: Optimal tower heights for different modules as a function of the power size

Polar fields generally require higher towers than surrounded fields, and cornfield layouts require even greater heights than radial stagger ones. This trend is explained by blocking losses, which particularly occur in polar fields since the mirrors to the north are much farther from the receiver than in surrounded ones, thus the angle drawn by the reflected rays to the ground is smaller and it is more likely that part of the reflected radiation hits the back of the heliostats just ahead. Also, in cornfield layouts the mirrors are all aligned, so each heliostat is much closer to the one ahead and an even higher tower is needed to reduce blocking losses. Another parameter affecting the tower height optimization is the cosine efficiency. Finally, in no case does the optimum exceed 150m due to the maximum height set for steel monopole towers. For greater heights, a concrete tower would be employed but this is not convenient in the power range in which the modules are analysed.

Land consumption

The increase in the land occupied by the modules as the nominal power raises is shown in Figure 5.14.

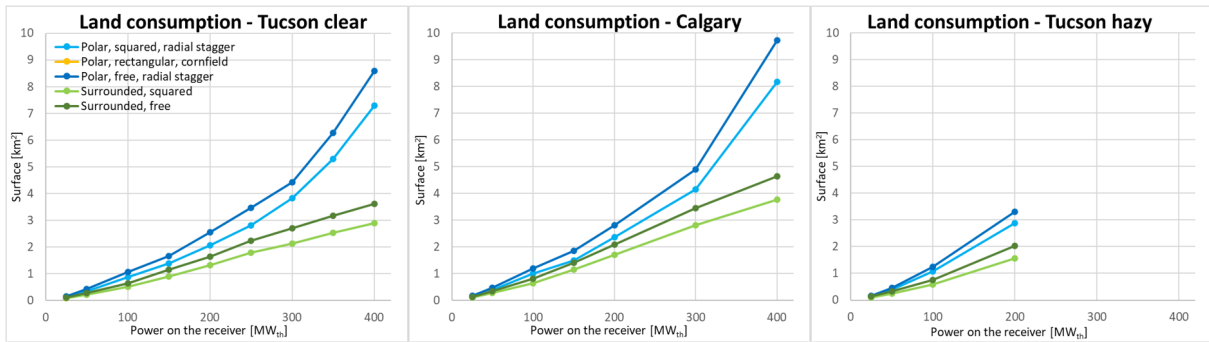


Figure 5.14: Land consumption of different layouts as a function of the power size for Tucson clear (left), Calgary (middle) and Tucson hazy (right)

In general, polar modules occupy more space than surrounded ones. This is because, even with the same optical efficiency, the last rows of heliostats in polar fields, being much more distant from the tower, have greater spacings in between. A steep growth in land occupancy of polar modules above 300 MW_{th} is seen.

In addition, in both polar and surrounded cases, square modules bring clear benefits in terms of land savings, with reductions for large sizes that can reach 1km², or 100 hectares, at the same power.

A greater land consumption in Calgary than in Tucson clear is noted, due to the lower elevation angle and thus the greater distance between rows. The land consumption further increases in the case of Tucson hazy, studied up to 200 MW_{th} because of the very low optical performances for larger modules due to the attenuation efficiency collapse.

It is pointed out that, other than adding a modest land cost, an excessive size can also affect O&M costs, as well as limit the maximum achievable power in the case of geographic obstacles. It is not just a matter of cost: if the plant is too large, the presence of mountains, rivers, cities, or other obstacles may limit the maximum power, as well as increase the chances of this being rejected by the local population for the NIMBY effect (Not In My Back Yard).

Efficiency

The efficiency items under design conditions are deepened to get a precise understanding of the several factors involved. The trends of the design optical efficiency items are shown in Figure 5.15 for Tucson clear and Calgary. Tucson hazy is not shown since it is very similar to the clear sky scenario, the only difference being that the attenuation efficiency decreases much more rapidly. In addition, the shading efficiency under design conditions

is always 100% because SolarPILOT purposely arranges heliostats to get this result, while the reflection efficiency is constant because the same default heliostat properties are used in all cases. Therefore, these values are not reported.

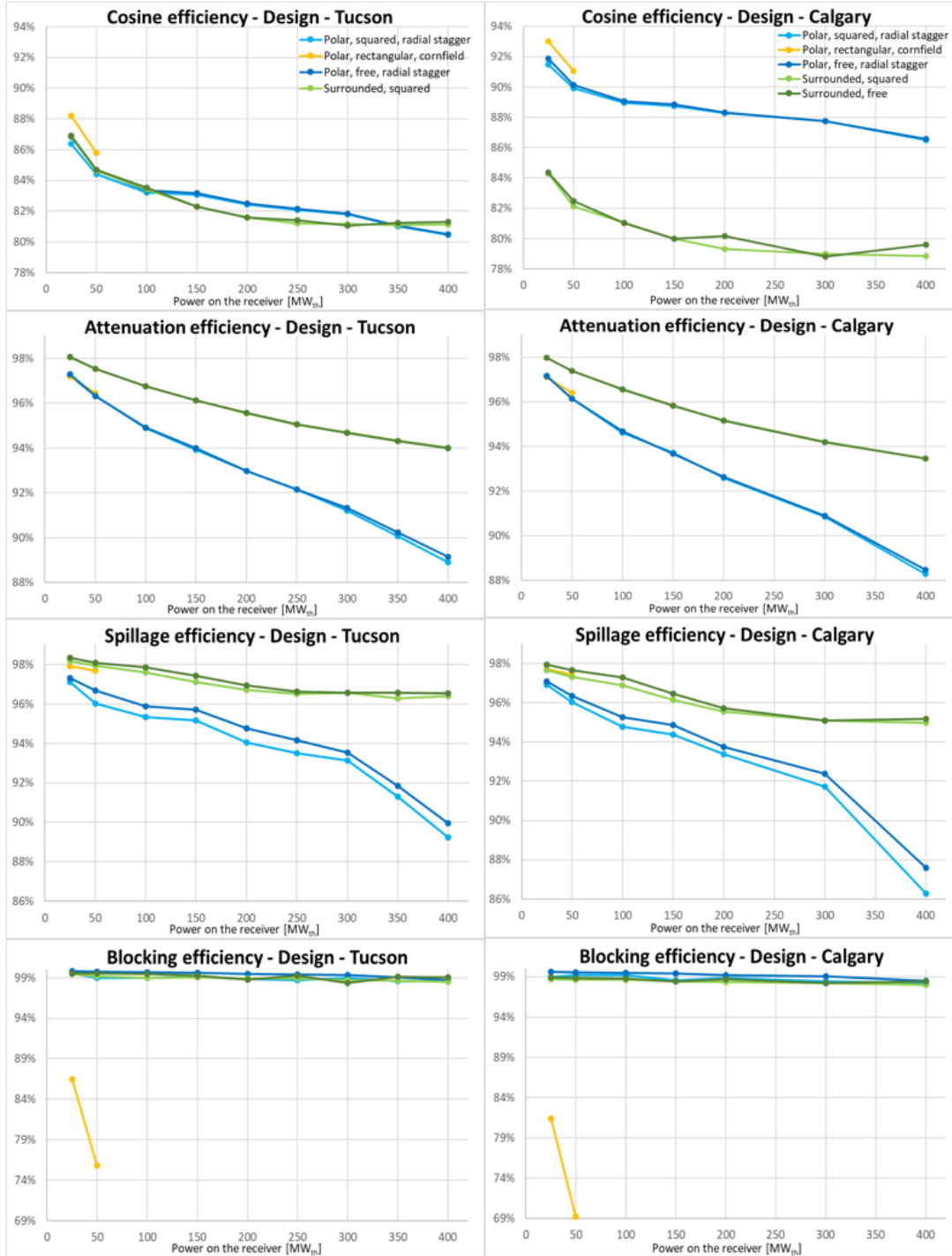


Figure 5.15: Cosine, attenuation, spillage and blocking efficiencies of the different layouts as a function of the power size for Tucson clear (left) and Calgary (right)

Regarding cosine efficiency, the trend is slightly decreasing as size increases and there is no significant difference between square and free-shaped fields. While in Tucson the cosine efficiency is very similar between polar and surrounded fields, in Calgary polar fields outperform surrounded ones by an average of 7-8% and exceed the Tucson values. Finally, the cosine efficiency of polar fields with cornfield layout is slightly higher than the corresponding radial stagger one. This is due to the greater tilt angle of the receiver, that is possible because SolarPILOT does not place heliostats behind the tower thanks to the field's geometric limits.

The attenuation efficiency, given the same clear atmospheric conditions, is progressively decreasing as the size increases and is almost the same between both square and free shape modules and between Tucson and Calgary. In practice, the attenuation efficiency is independent of both module's shape and latitude. On the other hand, a clear dominance of the surrounded fields over the polar ones is shown. This happens because, since in surrounded fields the heliostats are located on both sides of the tower, the average slant range is much smaller than in polar fields. Such difference grows from about 1% for 25 MW_{th} modules to approximately 5% for 400 MW_{th} fields.

Regarding the image intercept (spillage) efficiency, there is a slight superiority of the fields generated at Tucson compared to Calgary and of polar ones with free shape compared to square polar fields. These differences are explained because increasing the latitude results in larger fields, while square polar fields imply that some mirrors are too angled with respect to the receiver. In both cases the heliostats' position is not optimal, and their image does not completely hit the receiver. The main result lies in the better performance of surrounded fields compared to polar ones, similarly to the attenuation case. This difference is around 2-3% up to 300 MW_{th} and increases to 7-8% beyond. This reflects what happens for the land consumption. In fact, beyond 300 MW_{th} the polar fields' size grows uncontrollably, as the last rows are located very far from the receiver. As a result, their image on the receiver is much larger than its original shape and hits the tubes only partially.

Finally, the blocking efficiency trend reveals the poor optical performance of the cornfield layout, where the heliostats are all aligned, compared to the radial stagger one. This performance collapse confirms the inadequacy of such configuration for large field applications.

The overall design values of optical, thermal, and combined efficiencies in the three scenarios are shown in Figure 5.16.

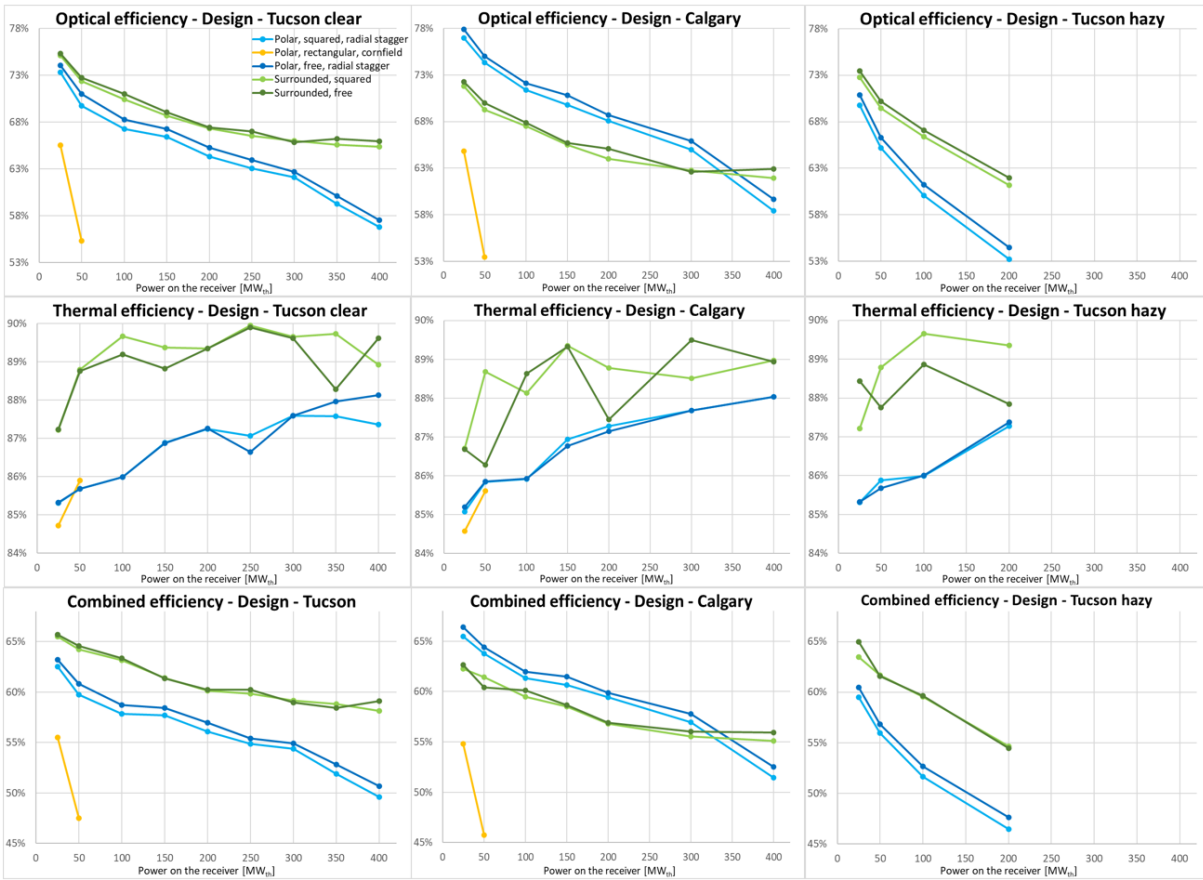


Figure 5.16: Optical, thermal, and combined efficiencies of the layouts as a function of the power size for Tucson clear (left), Calgary (middle) and Tucson hazy (right)

The optical efficiency trends consist of the product of all the terms described above. The poor performance of cornfield polar fields is immediately noticeable, along with the slight superiority of free shape fields over square fields. This difference, however, is just 1% on average in the polar case and 0.5% in the surrounded case. The most remarkable result is the great improvement in the optical performance of polar fields as latitude increases, accompanied by a slight decrease in the performance of surrounded fields. In fact, 25 MW_{th} free shape polar fields in Calgary reach the record optical efficiency of 78%. Furthermore, for large size surrounded modules, the optical efficiency almost reaches a plateau, while the polar ones decrease much markedly above 300 MW_{th}. Finally, the Tucson hazy scenario shows a faster decrease than the analogous clear case due to the attenuation efficiency collapse.

Turning to receiver thermal efficiencies, the increasing trend is due to two factors:

- The decrease in the weight of the spacing between tubes, set constant to 1mm, as the tube's diameter increases, which generally grows with the receiver size. This

means a higher ratio in useful heat transfer area over total receiver area.

- The decrease in the weight of low-flux regions on the receiver edges, hit by less images than central regions. As the receiver size grows, these regions occupy proportionally less space, leading to a growth in the average flux and thus in performance.

The high discontinuity of cylindrical receivers is due to the tubes' diameter optimization, which is discrete and based on standard diameters. The performance of cylindrical receivers is greater than the corresponding Billboard ones, due to the better flux distribution and the absence of the left and right low flux regions proper of Billboard. Figure 5.17 shows the comparison between a cylindrical and a Billboard receiver's flux map in the case of 25 MW_{th} free shape modules, for Tucson clear.

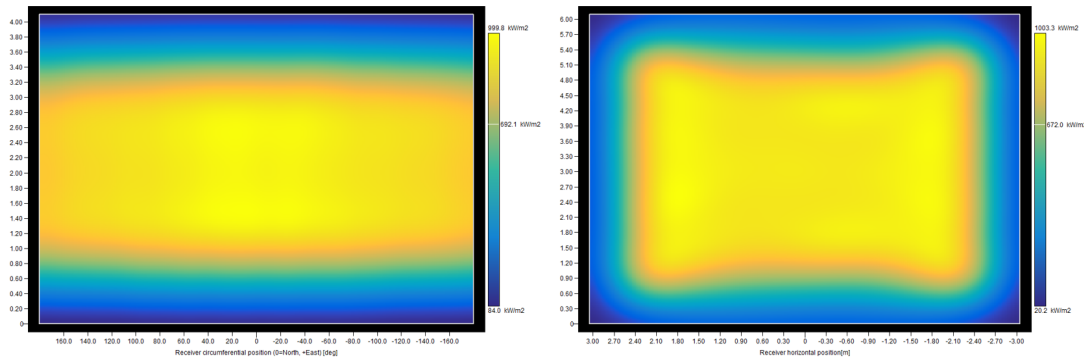


Figure 5.17: Cylindrical (left) and Billboard (right) heat flux maps for 25 MW_{th} modules

The combined efficiency is useful to evaluate the thermodynamic performance of modules under design conditions. The overall decreasing trend, the poor performances of polar cornfield modules, and the efficiency drop with a hazy sky can be seen. Most evident is the inversion of polar and surrounded field efficiencies between Tucson and Calgary. As latitude grows, polar fields improve their performance significantly while surrounded ones worsen it, thus polar layouts in Calgary perform better than surrounded ones up to about 300-350 MW_{th}. Moreover, surrounded layouts exhibit a plateau for high powers while polar ones show a drop in performance due to the sharp growth in dimensions. Finally, the difference in performances between square fields and free shape fields is further reduced. It averages less than 1% in the polar case, while it is practically negligible for surrounded modules.

LCOH

After analysing the performances of modules, it is necessary to include the economic part to determine which ones provide the lowest heat cost on annual basis, to employ them

in the further analysis. Figure 5.18 shows the LCOH trends for all modules, in the three scenarios. The values on the LCOH axes are the same in the Tucson cases, while they are different for Calgary, where the LCOH is significantly higher due to the lower DNI.

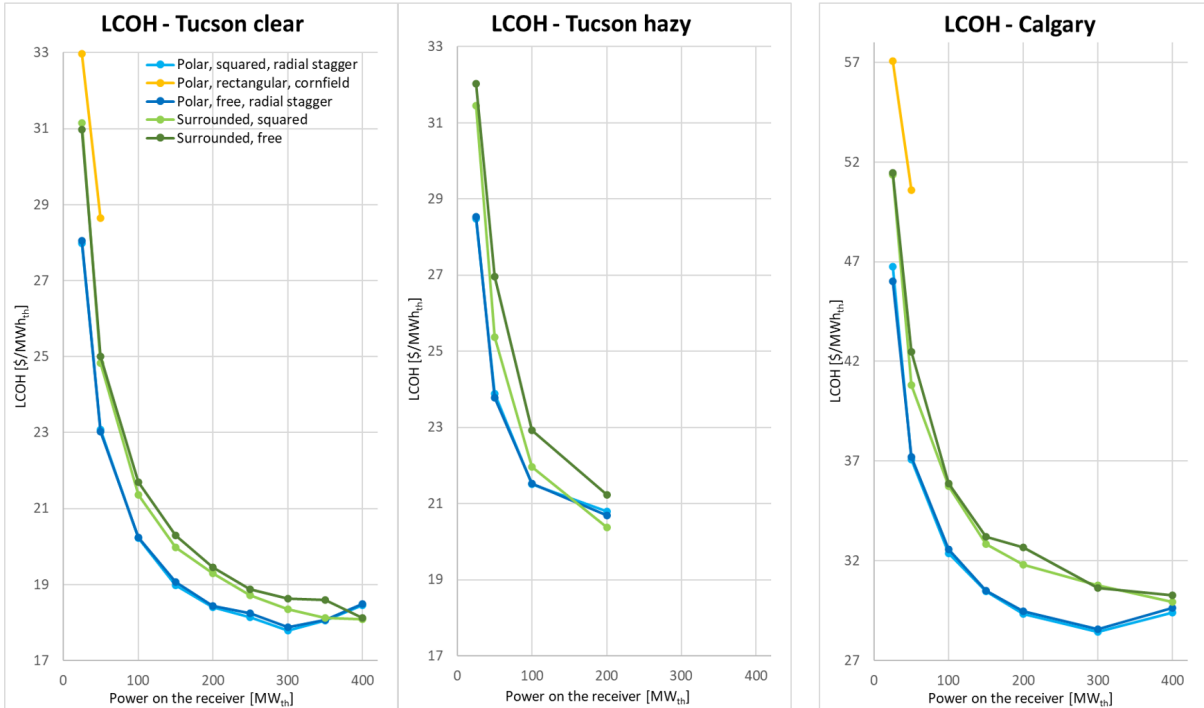


Figure 5.18: LCOH of the different layouts as a function of the power size for Tucson clear (left), Tucson hazy (middle) and Calgary (right)

The exponential decreasing trend of LCOH as size increases is suddenly apparent. This is closely related to economies of scale on the receiver cost and is gradually dampened by the performance decay of large modules especially for polar fields. Polar cornfield modules are excluded because of the previous considerations about performances.

In general, radial stagger polar modules are cheaper than their surrounded counterparts, and this gap grows with latitude because of the cosine efficiency. In fact, the transition thermal powers between polar and surrounded fields correspond to 350-400 MW_{th} for Tucson clear and overcome 400 MW_{th} for Calgary. On the other hand, when hazy atmospheric attenuation is considered, the transition occurs around 200 MW_{th}.

A further noteworthy result is that, in both polar and surrounded cases, square modules are slightly more competitive than free-shape ones. This happens because the lower performance is more than compensated in terms of capital cost by land saving.

Even before the piping system is analysed, it can be stated that few large size modules, rather than a multitude of smaller modules, will be convenient to reach large electric

powers with the present technology. This is confirmed by the numerical results shown in Table 5.1 for Tucson clear, Table 5.2 for Calgary, and Table 5.3 for Tucson hazy.

Tucson clear	Polar square	Polar free	Surr. square	Surr. free
Power [MW_{th}]	300	300	400	400
Land [km^2]	3.8	4.4	2.9	3.6
LCOH [$$/MWh_{th}$]	17.78	17.88	18.08	18.12

Table 5.1: Power, land size, and LCOH of the least-cost modules for Tucson clear

Calgary	Polar square	Polar free	Surr. square	Surr. free
Power [MW_{th}]	300	300	400	400
Land [km^2]	4.2	4.9	3.8	4.6
LCOH [$$/MWh_{th}$]	28.42	28.57	29.93	30.27

Table 5.2: Power, land size, and LCOH of the least-cost modules for Calgary

Tucson hazy	Polar square	Polar free	Surr. square	Surr. free
Power [MW_{th}]	200	200	200	200
Land [km^2]	2.9	3.3	1.6	2.0
LCOH [$$/MWh_{th}$]	20.79	20.68	20.37	21.23

Table 5.3: Power, land size, and LCOH of the least-cost modules for Tucson hazy

Finally, based on the selection criteria established in the methodology, just few modules among them are selected for further analysis.

In the Tucson clear case, for both polar and surrounded layouts, square modules have both a lower LCOH than corresponding free shape ones, and a smaller land footprint, thus the piping system will also be more compact and cheaper. It is therefore possible to exclude polar and surrounded modules with free shape in advance. Moreover, even if larger square polar modules ($350 MW_{th}$ and $400 MW_{th}$) could lead to improved performances after accounting for the piping system, they are still outperformed by the surrounded square $400 MW_{th}$ module, thus they are excluded. Hence, the modules analysed in this case are:

- Polar square 300 MW_{th}
- Surrounded square 400 MW_{th}

A similar reasoning is held for Calgary. Moreover, even if the polar square 400 MW_{th} module has a lower LCOH than the respective surrounded square 400 MW_{th} one, it is not analysed because of its excessive land footprint (8.2km²). Therefore, again, the following modules are selected:

- Polar square 300 MW_{th}
- Surrounded square 400 MW_{th}

Finally, considering Tucson hazy, the selection is easier since the module with the highest power also has the lowest LCOH and the smallest land footprint, and it is the case of:

- Surrounded square 200 MW_{th}

Piping system

The piping system's layout depends on the number of modules, and this is determined by the desired electric power output. In the present study, plants around 100 MW_{el} are studied for Tucson clear and Calgary, while a plant around 50 MW_{el} is investigated for Tucson hazy. Note that the actual size of the plants may not be exactly equal to the one defined here because of the solar multiple's optimization procedure. Given the thermal power output of the optimal layouts, the number of modules is estimated as follows.

- For both Tucson clear and Calgary, two modular systems are analysed. The first one consists of 3 polar square modules of 300 MW_{th} each, and the second one of 2 surrounded square modules of 400 MW_{th} each. These are compared to a conventional 900 MW_{th} plant for each location.
- For Tucson hazy, a single modular plant with 2 surrounded square modules of 200 MW_{th} each is compared to a conventional 400 MW_{th} plant.

The layouts whose piping system is studied are thus divided into three cases: 3 polar square modules, 2 surrounded square modules, 1 conventional plant. The schematizations of the modular plants are depicted qualitatively in Figure 5.19, while the conventional plant is shown in Figure 5.20.

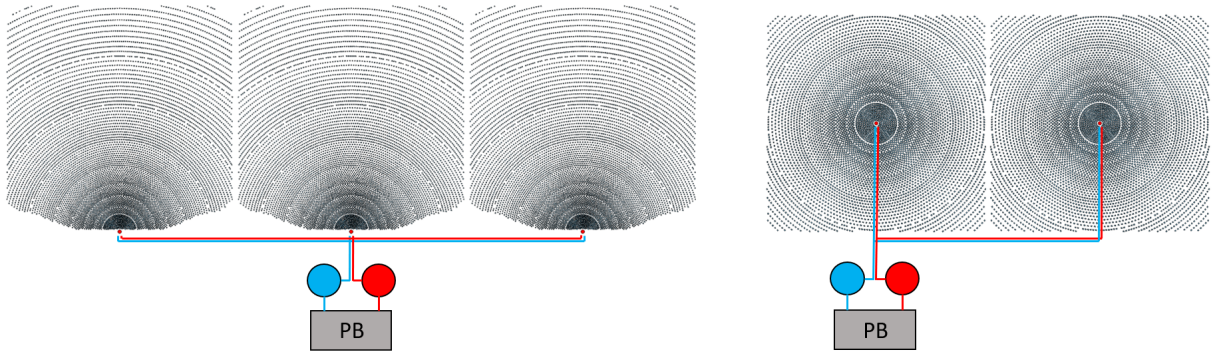


Figure 5.19: Layout of the modular plants with 3 polar square modules (left) and 2 surrounded square modules (right)

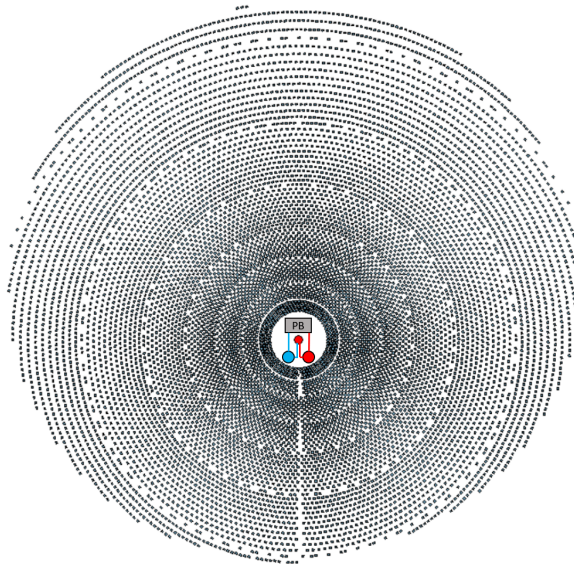


Figure 5.20: Layout of the conventional plant

5.3.3. Plants

Following the SM and TES size optimizations, as well as the generation of the optimized conventional plants, it is possible to compare the results at the plant level in the three scenarios. To keep the validity of the comparisons even among plants with slightly different power outputs and locations, mostly specific indicators are used.

Plant results

The main design features and results for the generated plants are given in Table 5.4 for Tucson clear, Table 5.5 for Calgary, and Table 5.6 for Tucson hazy. As noted, for Tucson clear the SM optimization results in the comparison of a 3 polar modules plant and a

conventional plant with a 110 MW_{el} PB, with a plant with 2 surrounded modules with an electric power of 100 MW_{el}. Similarly, in Calgary the plant with 3 polar modules and the conventional one have a power of 100 MW_{el} while the plant with 2 surrounded modules is 90 MW_{el}. Finally, for Tucson hazy, both the plant with 2 surrounded modules and the conventional one have an electric power of 45 MW_{el}.

Plant results – Tucson clear	3 x Polar	2 x Surr.	Conventional
Receiver power [MW _{th}]	300*3	400*2	900
Plant surface [km ²]	10.4	4.5	8.0
Tower height [m]	150 Steel	150 Steel	220 Concrete
Solar Multiple [-]	2.9	2.9	3.0
TES size [h]	14	13	14
Plant electric power [MW _{el}]	110	100	110
Sun-to-el. efficiency, des. [%]	20.9	21.9	21.4
AEP [GWh _{el} /y]	709	585	677
Capacity factor [%]	73.5	66.8	70.2
CAPEX [M\$]	639	545	637
CAPEX specific [\$/kW _{el}]	5809	5447	5791

Table 5.4: Main design parameters and results for Tucson clear

Plant results – Calgary	3 x Polar	2 x Surr.	Conventional
Receiver power [MW_{th}]	300*3	400*2	900
Plant surface [km^2]	11.3	5.8	11.1
Tower height [m]	150 Steel	150 Steel	210 Concrete
Solar Multiple [-]	3.2	3.2	3.3
TES size [h]	14	14	14
Plant electric power [MW_{el}]	100	90	100
Sun-to-el. efficiency, des. [%]	21.8	20.1	19.8
AEP [GWh_{el}/y]	448	378	438
Capacity factor [%]	51.1	48.0	50.0
CAPEX [M\$]	633	574	659
CAPEX specific [$$/kW_{el}$]	6330	6378	6590

Table 5.5: Main design parameters and results for Calgary

Plant results – Tucson hazy	2 x Surr.	Conventional
Receiver power [MW_{th}]	200*2	400
Plant surface [km^2]	2.5	3.2
Tower height [m]	110 Steel	170 Concrete
Solar Multiple [-]	3.2	3.2
TES size [h]	14	14
Plant electric power [MW_{el}]	45	45
Sun-to-el. efficiency, des. [%]	20.3	19.7
AEP [GWh_{el}/y]	284	287
Capacity factor [%]	72.0	72.8
CAPEX [M\$]	297	314
CAPEX specific [$$/kW_{el}$]	6600	6978

Table 5.6: Main design parameters and results for Tucson hazy

In general, the plants with 2 surrounded modules, although they have slightly lower power outputs in the first two scenarios, occupy almost half of the land. Even in the Tucson hazy case, the impact on land is lower than the conventional plant.

Solar multiples are generally high: 2.9 to 3.0 for Tucson clear, 3.2 to 3.3 for Calgary and 3.2 for Tucson hazy. This means that it is convenient to oversize the solar fields to make the plants dispatchable during the hours when the DNI is too low or absent, and results in high TES sizes of 13-14h. In addition, for Calgary (where the DNI is lower) and Tucson hazy (where the combined efficiency is lower) the solar multiples are higher. Here, the reduction in the heat delivered by the HTF is compensated by a decrease in the PB size.

Regarding solar-to-electric efficiency, in no case does the conventional field present the highest efficiency. Moreover, while for Tucson clear the modular configuration with 2 surrounded fields presents a higher efficiency than the 3 polar modules, this is reversed in Calgary due to the combined efficiency.

The capacity factor is slightly lower for plants with 2 surrounded modules than for the other configurations. Furthermore, the capacity factor at Calgary is about 20% lower in absolute terms than at Tucson because of the lower annual DNI.

Finally, conventional plants do not have the lowest specific CAPEX in any case. In these terms, Tucson hazy results the most expensive due to the low optical efficiency and the small scale, followed by Calgary for the low capacity factor. Hence, the Tucson clear scenario is cheaper due to the better conditions.

Annual efficiencies

To analyse the plant performances in detail, the components' annual efficiencies are reported in Table 5.7 for Tucson clear, Table 5.8 for Calgary, and Table 5.9 for Tucson hazy. Annual efficiencies are preferred because they better represent the actual operation of the plant, as opposed to design efficiencies which are evaluated at a single instant with optimal conditions and therefore can be misleading. However, all design efficiencies are given in Appendix B.

Annual efficiencies [%] – Tucson clear	3 x Polar	2 x Surr.	Conventional
Optical	57.3	55.0	54.2
Receiver	84.2	84.9	85.7
Piping	99.6	99.6	>99.9
Power block	40.8	40.8	40.8
Auxiliary	98.0	97.7	97.6
Solar to electric	18.0	17.6	17.4

Table 5.7: Annual efficiencies of the modular and conventional plants for Tucson clear

Annual efficiencies [%] – Calgary	3 x Polar	2 x Surr.	Conventional
Optical	53.5	48.5	47.6
Receiver	80.4	81.2	81.1
Piping	99.5	99.5	>99.9
Power block	41.1	41.0	41.0
Auxiliary	98.0	97.2	97.5
Solar to electric	15.5	14.1	13.8

Table 5.8: Annual efficiencies of the modular and conventional plants for Calgary

Annual efficiencies [%] – Tucson hazy	2 x Surr.	Conventional
Optical	51.5	49.7
Receiver	85.3	84.7
Piping	99.5	>99.9
Power block	40.4	40.4
Auxiliary	98.0	98.1
Solar to electric	16.0	15.4

Table 5.9: Annual efficiencies of the modular and conventional plants for Tucson hazy

Looking at the optical efficiencies, conventional fields always perform worse than modular fields, due to the large size and thus the huge reduction that occurs especially in attenuation and spillage efficiencies. In addition, a clear superiority of polar modules over surrounded ones is shown, due to the greater annual balance of cosine efficiency that polar layouts allow as the sun's elevation angle varies. This difference goes from 1.8% to 2.3% in low-latitude cases, up to 5.0% at high-latitude. Finally, with the same plant configuration, the annual efficiencies for Tucson clear are significantly higher than those in Calgary due to the latter's low elevation angle in the winter months, and thus to the reduction in the annual cosine efficiency. For Tucson hazy, instead, the optical efficiency reduction is due to the sharp increase of the attenuation losses.

The receiver thermal efficiency varies slightly among the configurations. The efficiency of Billboard receivers is lower than their cylindrical counterparts. Finally, the receivers of the systems placed in Calgary have on average annual efficiencies 4% lower than the counterparts in Tucson. This is because, in low DNI and high-latitude locations, the receiver operates for many hours during the year in a low heat flux off-design regime, which results in higher thermal losses.

Since the external temperature of the piping tubes is just 5°C higher than the ambient temperature at design conditions, the thermal efficiency of the piping system is always very high. For the modular configurations it is around 99.5% – 99.6%, while in the conventional case it is almost 100% due to the minimal spatial extent of the system.

The 1 reheat PB does not depend on the solar field set-up, so under the same conditions at comparable sizes its efficiency is very similar for all the configurations. Compared to Tucson clear, the efficiency at Calgary is slightly higher due to the lower average ambient temperature, which improves the air-cooled condenser's performance. In contrast, moving to Tucson hazy, the efficiency goes down due to the size reduction from 100-110 MW_{el} to 45 MW_{el}.

The auxiliary efficiency represents here just the HTF pump's electric consumption, necessary to overcome the HTF pressure losses within receiver and piping. It is almost constant in all cases, since the pressure losses in the modular plants' piping system are large against those inside the small receivers, while in conventional plants the opposite occurs. Polar systems with Billboard receivers exhibit slightly higher efficiencies due to the lower pressure losses, because the number of receiver panels in series crossed by the HTF is smaller compared to the cylindrical receiver.

Finally, looking at the annual solar-to-electric efficiency, in all cases conventional systems perform worse than their modular counterparts, while modular configurations with 3

polar fields perform better than those with 2 surrounded fields in both scenarios. Finally, Tucson clear has the highest efficiencies, followed by Tucson hazy and Calgary because of the lower optical and thermal performances on annual basis.

Specific costs

Specific CAPEX, referring to the nominal electric power output, are a good indicator of the weight of the components on the total plant's cost. The results, for each component of each plant in each scenario, are shown in Figure 5.21.

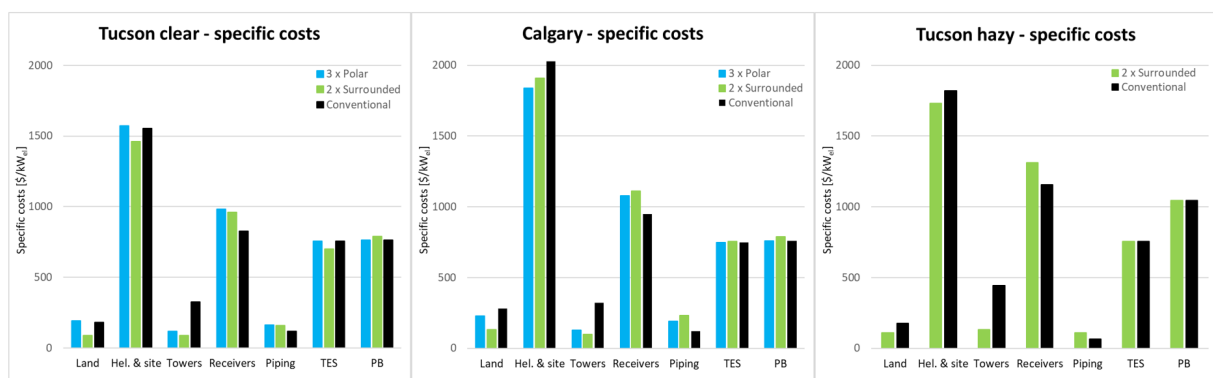


Figure 5.21: Specific CAPEX of the components of each plant, for Tucson clear (left), Calgary (middle) and Tucson hazy (right)

The heliostat field has the largest costs, followed by receivers, PB, and TES. In contrast, the cost of the land, towers and piping system is much lower.

The land costs for the plant with 2 surrounded modules are significantly lower than those in the other cases because of the smaller space occupied. Similarly, the piping system's cost of conventional plants is generally lower than in modular ones.

In addition, the receiver's cost in the conventional plant is always lower than the total specific cost of the modular plants' receivers, because of the economies of scale involved in purchasing a single large receiver as opposed to two or three small ones for the same power. However, this is offset by the higher cost of a concrete tower in conventional fields, compared to buying even more than one steel monopole tower. This is also shown in Figure 5.22, in which the cost breakdowns of the three plants for Tucson clear are depicted. The sum of the weight of towers and receivers is 24%-25% in all cases. Also noticeable is the significantly low weight of land and piping costs.

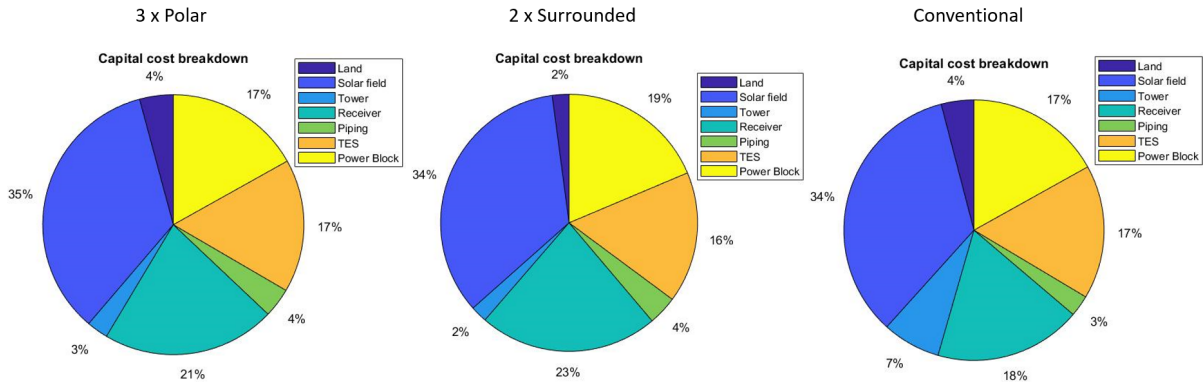


Figure 5.22: Direct costs breakdown of each plant for Tucson clear

Finally, the weight of PB and TES costs is almost constant between the modular and conventional cases in all conditions, since the main difference between the configurations lies in solar fields and piping systems, not in the downstream components.

Land-specific productivity

Table 5.10 shows the land-specific productivity results for all configurations in the three scenarios. The reference for calculating the variations is the conventional plant.

LSP [GWh/km ² y]	3 x Polar	2 x Surr.	Conventional
Tucson clear	68 (-20%)	130 (+53%)	85
Calgary clear	40 (+3%)	65 (+67%)	39
Tucson hazy	-	114 (+27%)	90

Table 5.10: Land-specific productivity of plants in the three scenarios

The configuration with 2 surrounded modules brings excellent benefits in terms of compactness in all cases, reaching the record increase of 67% in the high-latitude case of Calgary. These benefits go beyond the LCOE calculation and may consist in the actual feasibility of the plant due to geographic constraints or in greater acceptance by the populations living near the selected location. Regarding 3 polar modules, on the other hand, for Tucson clear the plant is less compact than the conventional one, while in Calgary the benefits are almost negligible due to the increased performances of polar fields compared to surrounded ones.

To make an indicative comparison with other renewable technologies, from [100] the LSP is calculated for 12 currently operating photovoltaic plants worldwide between 32° and

35.5° latitude (Tucson is 32.1°). All these plants have rated capacities greater than 250 MW_{el}, however, their LSP is not affected by the plant size since PV is a modular technology. Comparing these values with the plants generated in the most likely conditions for CSP, Tucson clear, yields the results depicted in Figure 5.23. The configuration with 2 surrounded modules outperforms all the PV systems in terms of compactness.

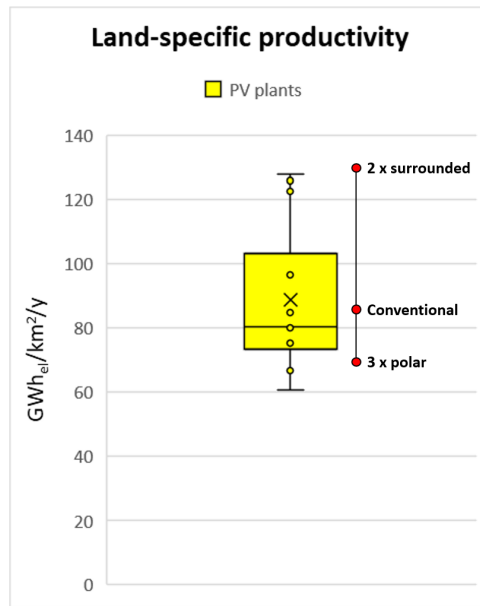


Figure 5.23: LSP comparison between PV and CSP plants at Tucson's latitude

Levelized cost of electricity

Table 5.11 shows the LCOE results for all plants and scenarios analysed, along with the percentage variations of modular plants compared to the respective conventional ones.

LCOE [\$/MWh _{el}]	3 x Polar	2 x Surr.	Conventional
Tucson clear	93.74 (-4.0%)	97.31 (-0.4%)	97.67
Calgary clear	143.61 (-5.6%)	153.70 (+1.1%)	152.08
Tucson hazy	-	106.77 (-3.6%)	110.79

Table 5.11: Levelized cost of electricity of plants in the three scenarios

For Tucson clear, a modular system with 3 square polar fields allows for a 4% LCOE reduction compared to the conventional case. This is mainly due to the great optical efficiency increase on annual basis, which in the polar case is 3.1% higher in absolute terms, given the substantial parity in specific costs. However, this plant has a 20% lower

LSP than the conventional case, which means it is less compact. On the contrary, the plant with 2 square surrounded modules has an LCOE almost equal to the reference case (just 0.4% lower) but ensures the construction of a much more compact plant (+53% in LSP). Furthermore, in absolute terms, the LCOEs result just slightly higher than those of other renewables presented in Figure 1.6, and competitive with fossil fuel plants. However, the results in absolute terms should be taken with caution given the uncertainty around costs.

Looking at the results for Calgary, an even greater LCOE reduction for 3 square polar modules is shown, corresponding to 5.6%. This is due to both a reduction in specific costs and to the higher annual optical efficiency at high-latitude, which is 5.9% higher than the conventional case in absolute terms. This plant is also slightly more compact than the conventional one (+3% in LSP) due to the inconvenience of large surrounded fields at high latitudes. The case with 2 square surrounded modules is slightly more expensive (+1.1% in LCOE compared to the conventional case) but enormously more compact (+67% in LSP), so it would be plausible to accept a slightly higher electricity cost to build a plant that covers much less land. In absolute terms, due to the reduction in the yearly DNI, the LCOE is more than 50% higher than for Tucson clear.

From the Tucson hazy case it is understood that, with high atmospheric attenuation, even for smaller plants (45 MW_{el}) the case with 2 square surrounded modules leads to some benefits. In fact, there is a 3.6% reduction in LCOE associated to a 27% increase in LSP. This is due to both a decrease in specific costs (from 6978 \$/kW_{el} to 6600 \$/kW_{el}) and an increase in the annual optical efficiency, from 49.7% to 51.5%, due to the reduction of the field's size and specifically of the average slant range.

Finally, for Tucson clear and Calgary, the benefits of modular fields are found just for sizes of 100-110 MW_{el}, while decrease as the size is reduced until they are nullified around 50 MW_{el}, where a single field is more cost-effective than a modular system. This can be deduced from the LCOH trends, and similarly applies to Tucson hazy, where for sizes below 45 MW_{el} a conventional solution starts to be convenient.

5.3.4. Modularity up to 500 MW_{el}

Table 5.12 shows all the cases studied in terms of net electric power and number of modules, varying the type of square modules (polar or surrounded) and reheats, in the Tucson clear scenario.

Polar – 1 reheat	Polar – 2 reheats	Surr. – 1 reheat	Surr. – 2 reheats
110 MW _{el} , 3 mod.	-	100 MW _{el} , 2 mod.	-
200 MW _{el} , 5 mod.	200 MW _{el} , 5 mod.	200 MW _{el} , 4 mod.	200 MW _{el} , 4 mod.
300 MW _{el} , 8 mod.	300 MW _{el} , 8 mod.	300 MW _{el} , 6 mod.	300 MW _{el} , 6 mod.
400 MW _{el} , 11 mod.	400 MW _{el} , 11 mod.	400 MW _{el} , 8 mod.	400 MW _{el} , 8 mod.
500 MW _{el} , 13 mod.	500 MW _{el} , 13 mod.	500 MW _{el} , 10 mod.	500 MW _{el} , 10 mod.

Table 5.12: Set of modular plants analysed

Figure 5.24 shows the trends of the main design efficiencies involved in the analysis.

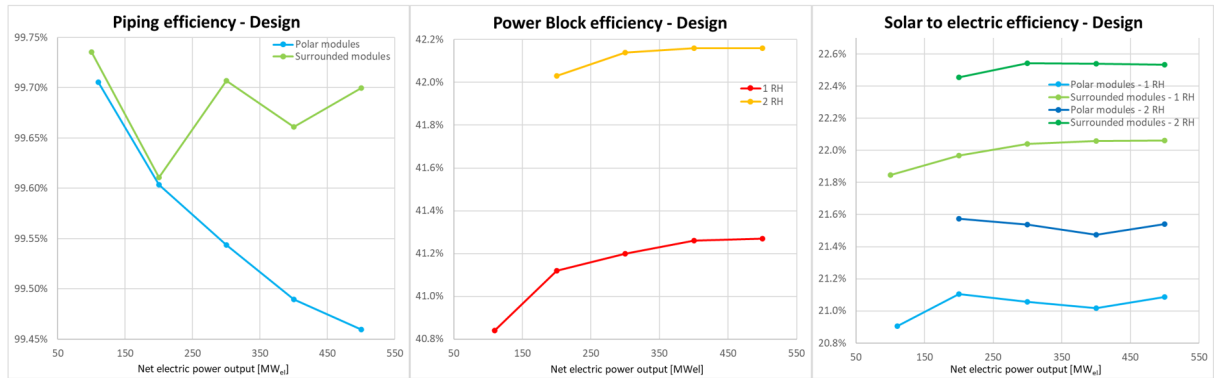


Figure 5.24: Piping, PB, and solar-to-electric efficiency function of the electric power

Regarding the piping efficiencies, as size and number of modules increase, the value varies very little. Furthermore, in the case of polar square modules the efficiency has a monotonic decreasing trend, while for surrounded square ones the variation is smaller and the trend is quite stable. This is because surrounded modules are smaller and more compact than polar ones, and fewer of them are required for the same electric power. The addition of new surrounded modules does not decrease the efficiency due to the high compactness of the field, because, in the pipe sections closest to the TES that carry the largest flow rates, the addition of a module results in an increase in the local thermal efficiency allowing for a reduction of the ratio wall surface / flow rate. In fact, a doubling of the cross section (hence of the mass flow rate at constant density and HTF velocity) results in a $\sqrt{2}$ increase

in the pipe's perimeter, and thus in the heat transfer area.

$$A_1 = \pi \cdot r^2$$

$$P_1 = 2 \cdot \pi \cdot r$$

$$A_2 = 2 \cdot A_1 = 2 \cdot \pi \cdot r^2$$

$$P_2 = 2 \cdot \sqrt{2} \cdot \pi \cdot r < 2 \cdot P_1$$

Due to the field's compactness, such efficiency-increasing effect in the main collectors closer to the TES compensates the new smaller pipes with higher losses, brought by the connection of new modules farther from the TES. In contrast, such compensation does not occur in polar fields due to their reduced compactness, and the effect of the low-efficiency pipes connecting the new modules farther from the TES prevails, leading to a reduction in the overall piping efficiency. The PB's design efficiency shows an increase around 1% moving from 1 to 2 reheats. Furthermore, the trend is increasing because, as the size of the cycle's components grows, some losses decrease, such as the leakages between the turbine's blade tip and the casing. Finally, given the use of the same modules, the trends of the solar-to-electric efficiency as the net electric power output increases are determined by those just exhibited for piping system and power block. On average, systems with surrounded square modules exhibit solar-to-electric efficiencies that are approximately 1% higher than their counterparts with polar modules. Also, for each type of module, systems with 2-reheats cycles have, on average, solar-to-electric efficiencies approximately 0.5% higher than their counterparts with 1-reheat cycles.

The specific costs as a function of net electric power output are depicted in Figure 5.25.

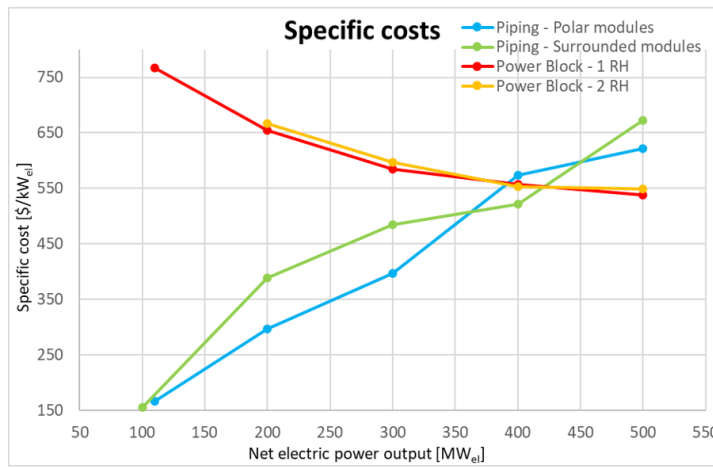


Figure 5.25: Specific costs of the piping systems and PB function of the electric power

While the specific cost of the power block decreases as the installed power raises due to

the economies of scale, the specific cost of the piping system increases significantly. This occurs because modules are added at an increasing distance from the TES, so for the same power addition, the amount of material required is always greater due to the increasing size and distance covered by the system. The discontinuity in the piping trends between polar and surrounded modules is due to the different sizes and number of modules that are progressively added. Lastly, the specific cost increase obtained by adding a second reheat to the power block is almost negligible, so such an addition seems always convenient, if technically possible.

Finally, in Figure 5.26, the trends in land consumption and LCOE are shown, compared to the case where several conventional plants, side-by-side but independent, are built to generate the same power.

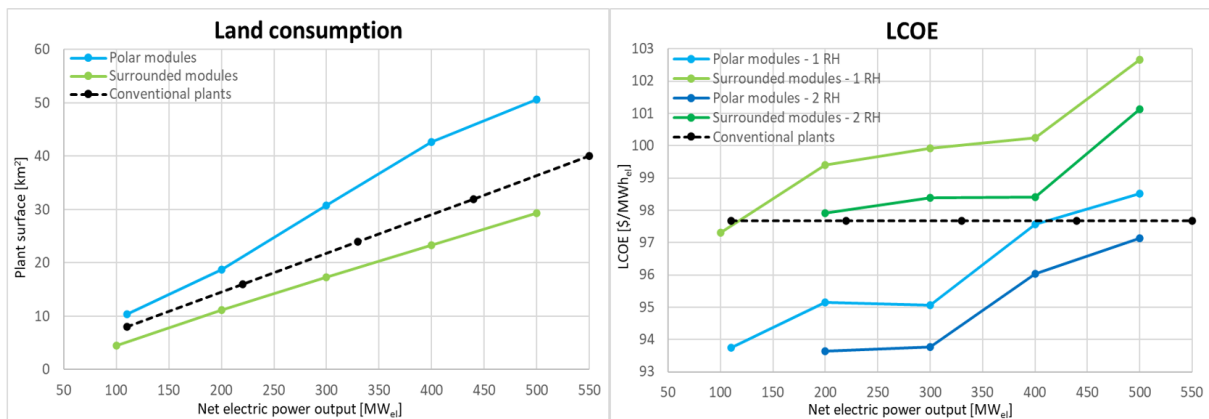


Figure 5.26: Land consumption (left) and the LCOE (right) for the modular plants and many adjacent conventional plants

Looking at the land consumption, modular plants made by surrounded square modules are more compact than equivalent conventional plants, while those with polar square modules occupy a much larger space, which is almost prohibitive for high powers. For example, considering a 500 MW_{el} plant, the case with surrounded modules occupies around 30km² of land, conventional plants occupy about 37km², while a plant with polar modules covers 51km², or 5100 hectares.

The lowest LCOEs correspond to the smallest plants. This is because the increase in the piping system's specific cost weighs much more than the decrease in the power block's specific cost and the improvement in its performance. Hence, even if modularity allows to overcome the conventional size limit of 110 MW_{el} caused by the subsequent optical decay of conventional plants, the piping system hinders the achievement of large power sizes for CSP tower plants.

In addition, the LCOEs of modular polar layouts are always lower than surrounded ones and multiple conventional plants. In contrast, the plants with surrounded modules have higher LCOEs than conventional plants. However, the LCOE increase of modular systems as the electric power increases is low. In fact, a 5-fold increase in the plant's size corresponds on average to a +5% in the LCOE.

Then, the 2-reheats cycles always allow for a slight LCOE reduction compared to the similar cases with 1 reheat, averaging around 1.5 \$/MWh_{el}. This ensures the possibility to build plants up to 300 MW_{el} without raising the LCOE significantly. Therefore, the construction of 500 MW_{el} modular plants is not recommended in either case.

In conclusion, while polar modular layouts generally have a lower LCOE than conventional plants, they lead to a higher land use. In contrast, surrounded modular layouts allow for a reduction in the land footprint, even if the LCOE is slightly higher than in conventional plants. Therefore, the choice of the optimal configuration depends on the specific needs, that can be the minimization of costs rather than the reduction of the land footprint. Another outcome is that cycles with 2 reheats are always cost-effective compared to the analogous cases with 1 reheat.

6 | Conclusions and future developments

In this thesis, a techno-economic analysis and optimization of large-scale modular CSP tower plants employing solar salts as heat transfer fluid and a steam Rankine cycle is carried out.

After introducing Concentrated Solar Power technology and its dispatchability advantage over variable renewable technologies such as solar PV and wind power, a literature review is carried out, and the main research trends are highlighted. One of these consists in modularity, which has been little explored at present, while the literature results appear to be discordant. Then, the few existing small-size modular systems are described and the main advantages and disadvantages that such innovation would bring on a large scale, compared to conventional state-of-the-art plants, are identified.

Next, the thermodynamic models needed to evaluate the design and annual performances of the main components are described. SolarPILOT is used for the solar field, a Matlab model from literature is used for the receiver, while a Thermoflex model is also taken from literature for a 1-reheat PB, and is later modified to analyse a PB with 2 reheats. In addition, a detailed Matlab model of the piping system is developed from scratch, allowing the evaluation of thermal losses, pressure losses, and costs of this component within a modular system. This model is very flexible since it allows the analysis of plants with any number of modules, geometry, size, and arrangement around the TES. Such model is also essential to link the solar field and receiver models to the PB, ensuring the possibility to perform a detailed thermodynamic analysis of all plant components. Furthermore, a step-by-step methodology for the design and optimization of modular and conventional plants is defined. This consists in a bottom-up approach in which modules of different geometries and sizes are studied. The parameters of merit are LCOH, LCOE, and the new LSP, a specific indicator to compare the plants' compactness in producing electricity, which is given by the ratio of the annual electricity production to the land size of the entire plant. A cost model is also developed, which based on data from

literature estimates the costs of each component and evaluates the main economies of scale. These costs are aggregated in the CAPEXs, which along with OPEXs contribute to the LCOH and LCOE calculation. The major technical innovation, concerning the analysis of modular plants, consists in the combination of thermodynamic models of all components with a precise methodology and a cost model. This makes the whole modular plant's design and optimization a straightforward and accurate process, meanwhile simplifying the comparison with reference plants by means of few intensive indicators.

First, the results of the Billboard thermal model's discretization analysis are reported and a brief case study employing Vast Solar modules is carried out. Then, the results of the main case study are investigated. After stating data and assumptions, modules of different sizes and geometries are analysed in three scenarios depending on latitude, DNI and atmospheric attenuation.

As for the tower location with respect to the south side of square and free-shaped surrounded fields, the LCOH optimum always results in the case with the tower placed exactly in the centre of the field at every latitude. This happens because such arrangement allows for a higher and more homogeneous thermal flux, thus a smaller and cheaper receiver is needed.

The combined efficiency of modules as a function of their nominal power shows a progressive increase with latitude in the performances of polar modules compared to surrounded ones, mainly due to the cosine efficiency growth at high latitudes. From the LCOH perspective, polar modules are mostly cheaper than their surrounded counterparts. In fact, the transition at which surrounded fields become more convenient than polar ones is around 350 MW_{th} at low latitudes, while it moves beyond 400 MW_{th} at high latitudes. Furthermore, square modules are cheaper than free-shape ones in all scenarios, as the slightly lower performances are more than compensated by the reduced land costs.

The plant-level results show that the design solar-to-electric efficiency of conventional plants is always lower than in modular plants, while specific costs are generally higher. This is mainly due to the annual optical efficiency, which shows a clear superiority of modular systems over conventional ones in all scenarios, and of polar modules over surrounded ones. As for the piping, even if modular systems have higher losses and costs, the impact on plants overall is almost negligible around 100 MW_{el} . Moreover, the higher specific costs of modular plants in terms of receiver are almost totally offset by the cost reduction due to towers, which are steel monopole instead of concrete. Large surrounded square modules result much more compact than conventional CSP and equivalent PV plants. In fact, compared to conventional CSP, compactness increases by +53% at low

latitudes, +67% at high latitudes, and +27% with hazy sky, while the LCOE is almost the same in clear sky conditions (-0.4% at low latitudes and +1.1% at high latitudes), but faces a reduction (-3.6%) in the hazy sky case. In contrast, large polar square modules are less compact, -20% at low latitudes and +3% at high latitudes, but allow for LCOE reductions both at low latitudes (-4.0%), and at high latitudes (-5.6%). However, even if the LCOE reduction in high-latitude locations is more pronounced, the absolute value still stands around +53% compared to low latitude (rather than +56% in the reference case). It is therefore concluded that modularity alone hardly opens to CSP deployment in such regions.

Increasing the net electric power up to 500 MW_{el}, the relevance of the piping system arises. In fact, even if the piping efficiency varies negligibly as new modules are added, its specific costs significantly grow, as modules are progressively added further away from the TES. This growth overcomes the benefits provided by a larger PB in terms of performance (efficiency increase with size and number of reheats) and cost (economies of scale), causing an increasing LCOE trend. Therefore, while CSP modularity allows to go beyond the conventional plants' size due to its optical advantages, the piping system sets a new limit to the achievement of the large powers typical of gas-fired or nuclear plants. Moreover, plants made of polar modules are much larger but cheaper than many conventional plants, while those with surrounded modules are more expensive and compact. This latter layout, bringing significant land savings, is equally interesting because it offers the possibility of overcoming geographic constraints or even the opposition of local populations. Finally, a 2-reheats Rankine PB allows for modular plants up to 300 MW_{el} without raising the LCOE, since the addition of a second reheat allows for a LCOE reduction averaging 1.5 \$/MWh_{el}.

To further detail the analysis, the main points that could be explored by future studies are the following.

- The development of a more accurate cost analysis, possibly by obtaining real data sets and correlations from the components' manufacturing industry, to assess all the economies of scale between modular and conventional plants, dependent on both size and number of components purchased. This would be useful mainly for heliostats and small receivers. In addition, to assess the long-term competitiveness of this technology, reliable factors and correlations regarding the future cost decrease of all major components should be identified.
- The analysis of rectangular modules, with aspect ratio other than 1, instead of square modules, both in polar and surrounded cases. In fact, square modules are

selected as a matter of simplicity, but they may not consist in the optimal layout in terms of performance or land occupancy.

- The study of the modular system's off-design in the case of partial shading of the plant, where the assumption that all modules operate under the same conditions is overcome. This implies the calculation of different performances for each module and the presence of unbalanced mass flow rates in the branches of the piping system.
- The analysis of different features of the components, such as heliostats with lower optical errors, heliostats and receivers with different aspect ratios, liquid sodium as heat transfer fluid, different dispatch strategies managed by the TES, and sCO₂ power blocks.

Bibliography

- [1] NASA. *Global Climate Change, Vital Signs of the Planet: Understanding our planet to benefit humankind*. URL: <https://climate.nasa.gov/>.
- [2] M. Aengenheyster, Q. Yi Feng, F. Van Der Ploeg, H.A. Dijkstra. “The point of no return for climate action: Effects of climate uncertainty and risk tolerance”. In: *Earth System Dynamics* 9 (3 Aug. 2018), pp. 1085–1095. ISSN: 21904987. DOI: 10.5194/esd-9-1085-2018.
- [3] G. Manzolini. *Notes from the course “Solar and biomass power generation”*.
- [4] Us Epa and Climate Change Division. *Atmospheric Concentrations of Greenhouse Gases*. URL: www.epa.gov/climate-indicators.
- [5] R. K. Pachauri, L. Mayer, Intergovernmental Panel on Climate Change. *Climate change 2014: synthesis report*, p. 151. ISBN: 9789291691432.
- [6] F. Lopes et al. “Milankovic Pseudo-cycles Recorded in Sediments and Ice Cores Extracted by Singular Spectrum Analysis”. In: (). DOI: 10.5194/cp-2021-126.
- [7] J. Cook et al. “Quantifying the consensus on anthropogenic global warming in the scientific literature”. In: (2013). DOI: 10.1088/1748-9326/8/2/024024.
- [8] E. Colombo. *Notes from the course “Engineering and cooperation for development”*.
- [9] United Nations, Department of Economic and Social Affairs. *Sustainable Development: The 17 goals*. URL: <https://sdgs.un.org/goals>.
- [10] Trading Economics. *EU Natural Gas*. URL: <https://tradingeconomics.com/commodity/eu-natural-gas>.
- [11] International Renewable Energy Agency. *Renewable power generation costs in 2021*. 2022. ISBN: 978-92-9260-452-3. URL: www.irena.org.
- [12] Wikipedia. *Nuclear power by country*. URL: https://en.wikipedia.org/wiki/Nuclear_power_by_country.
- [13] ITER - *The way to new energy*. URL: <https://www.iter.org/>.
- [14] IEA - *International Energy Agency*. URL: <https://www.iea.org/data-and-statistics>.
- [15] McKinsey Company. *Commercialisation of Energy Storage in Europe*. URL: <https://www.mckinsey.com>.

- [16] A. Casalegno. *Notes from the course “Electrochemical energy conversion and storage”*.
- [17] L. Mauler et al. *Battery cost forecasting: A review of methods and results with an outlook to 2050*. Sept. 2021, pp. 4712–4739. DOI: 10.1039/d1ee01530c.
- [18] REN21. *Renewables 2022, Global Status Report*. 2022. ISBN: 978-3-948393-04-5.
- [19] URL: greenrhinoenergy.com/solar/radiation/spectra.
- [20] Global Solar Atlas. URL: <https://globalsolaratlas.info/map>.
- [21] M. Romero, J. González-Aguilar. “Solar thermal CSP technology”. In: *Wiley Interdisciplinary Reviews: Energy and Environment* 3 (Jan. 2014), pp. 42–59.
- [22] E. Karatairi. “Improving the efficiency of concentrating solar power systems”. In: *MRS Bulletin* 43 (Dec. 2018).
- [23] URL: <https://www.dreamstime.com/>.
- [24] URL: <https://www.pinterest.it/>.
- [25] M.R. Rodríguez-Sánchez, A. Sánchez-González, C. Marugán-Cruz, D. Santana. *New designs of molten-salt tubular-receiver for solar power tower*. 2014, pp. 504–513. DOI: 10.1016/j.egypro.2014.03.054.
- [26] X. Yang, Z. Cai, T. Luo. *A special type of tube receiver unit for solar thermal power generation towers*. 2020. DOI: 10.1016/j.egypr.2020.10.017.
- [27] G. Tiryaki, U. Çamdali. *Cavity receiver optimization of the solar tower power system*. 2017. URL: <https://www.researchgate.net/publication/323704221>.
- [28] N. Boerema, G. Morrison, R. Taylor, G. Rosengarten. “High temperature solar thermal central-receiver billboard design”. In: *Solar Energy* 97 (Nov. 2013), pp. 356–368. ISSN: 0038092X. DOI: 10.1016/j.solener.2013.09.008.
- [29] European Union External Action. URL: <https://www.eeas.europa.eu>.
- [30] C. Wood, K. Drewes. *Vast Solar: improving performance and reducing cost and risk using high temperature modular arrays and sodium heat transfer fluid*. 2019.
- [31] Wikipedia. *Greenway CSP Mersin Solar Tower*. URL: https://en.wikipedia.org/wiki/Greenway_CSP_Mersin_Solar_Tower.
- [32] SUPCON solar experience. URL: www.supconsolar.com.
- [33] BrightSource. *Ivanpah Solar Electric Generating System*. Apr. 2014.
- [34] S. Schell. “Design and evaluation of eSolar’s heliostat fields”. In: *Solar Energy* 85 (4 Apr. 2011), pp. 614–619. ISSN: 0038092X. DOI: 10.1016/j.solener.2010.01.008.
- [35] Wikipedia. *Sierra SunTower*. URL: https://en.wikipedia.org/wiki/Sierra_SunTower.
- [36] SunDrop. *Overview of Sundrop Farms*. Oct. 2017.
- [37] URL: <http://envienta.net/>.

- [38] Siemens Gamesa. URL: <https://www.siemensgamesa.com/products-and-services>.
- [39] Vestas. URL: <https://www.vestas.com>.
- [40] General Electric. URL: <https://www.ge.com/renewableenergy/wind-energy>.
- [41] R. Serrano-López, J. Fradera, S. Cuesta-López. “Molten salts database for energy applications”. In: *Chemical Engineering and Processing - Process Intensification* 73 (Nov. 2013), pp. 87–102. ISSN: 02552701. DOI: 10.1016/j.cep.2013.07.008.
- [42] B. Mahmoud. “Thermal Energy Storage Using Molten Salts Containing Nanoparticles”. In: (June 2016).
- [43] G. Angelini, A. Lucchini, G. Manzolini. “Comparison of thermocline molten salt storage performances to commercial two-tank configuration”. In: *Energy Procedia* 49 (2014), pp. 694–704. ISSN: 18766102. DOI: 10.1016/j.egypro.2014.03.075.
- [44] J.H. Lim, B.B. Dally, A. Chinnici, G.J. Nathan. “Techno-economic evaluation of modular hybrid concentrating solar power systems”. In: *Energy* 129 (2017), pp. 158–170. ISSN: 03605442. DOI: 10.1016/j.energy.2017.04.067.
- [45] M. Puppe, S. Giuliano, C. Frantz, et al. “Techno-economic optimization of molten salt solar tower plants”. In: (Nov. 2018). DOI: doi.org/10.1063/1.5067069.
- [46] F. Rovense, M.Á. Reyes-Belmonte, M. Romero, J. González-Aguilar. “Thermo-economic analysis of a particle-based multi-tower solar power plant using unfired combined cycle for evening peak power generation”. In: *Energy* 240 (Feb. 2022). ISSN: 03605442. DOI: 10.1016/j.energy.2021.122798.
- [47] P.J. Turner, C. Sansom. “A Tubed, Volumetric Cavity Receiver Concept for High Efficiency, Low-cost Modular Molten Salt Solar Towers”. In: *Energy Procedia* 69 (May 2015), pp. 553–562. ISSN: 18766102. DOI: 10.1016/j.egypro.2015.03.064.
- [48] J. García-Barberena, A. Monreal, A. Mutuberria, M. Sánchez. “Towards cost-competitive solar towers - Energy cost reductions based on decoupled solar combined cycles (DSCC)”. In: *Energy Procedia* 49 (2014), pp. 1350–1360. ISSN: 18766102. DOI: 10.1016/j.egypro.2014.03.144.
- [49] J. Sorbet, M. Iñigo, J. García-Barberena, A. Bernardos. “Advanced power cycles and configurations for solar towers: Techno-economical optimization of the decoupled solar combined cycle concept”. In: *AIP Conference Proceedings* 2033 (Nov. 2018). ISSN: 15517616. DOI: 10.1063/1.5067073.
- [50] J.E. Rea et al. “Performance modeling and techno-economic analysis of a modular concentrated solar power tower with latent heat storage”. In: *Applied Energy* 217 (May 2018), pp. 143–152. ISSN: 03062619. DOI: 10.1016/j.apenergy.2018.02.067.

- [51] T. Lindquist et al. “A novel modular and dispatchable CSP Stirling system: Design, validation, and demonstration plans”. In: *AIP Conference Proceedings* 2126 (July 2019). ISSN: 15517616. DOI: 10.1063/1.5117591.
- [52] J. Serrano-Arrabal, J.J. Serrano-Aguilera, A. Sánchez-González. “Dual-tower CSP plants: optical assessment and optimization with a novel cone-tracing model”. In: *Renewable Energy* 178 (Nov. 2021), pp. 429–442. ISSN: 18790682. DOI: 10.1016/j.renene.2021.06.040.
- [53] G. Augsburger, D. Favrat. *From single- to multi-tower solar thermal power plants: investigation of the thermo-economic optimum transition size*.
- [54] P. Piroozmand, M. Boroushaki. “A computational method for optimal design of the multi-tower heliostat field considering heliostats interactions”. In: *Energy* 106 (July 2016), pp. 240–252. ISSN: 03605442. DOI: 10.1016/j.energy.2016.03.049.
- [55] F. Arbes et al. “Multi tower systems and simulation tools”. In: *AIP Conference Proceedings* 2126 (July 2019). ISSN: 15517616. DOI: 10.1063/1.5117516.
- [56] Z.A. Hussaini, P. King, C. Sansom. “Numerical simulation and design of multi-tower concentrated solar power fields”. In: *Sustainability (Switzerland)* 12 (6 Mar. 2020). ISSN: 20711050. DOI: 10.3390/su12062402.
- [57] L. Crespo, F. Ramos. “Making central receiver plants modular, more efficient and scalable”. In: *AIP Conference Proceedings* 2303 (Dec. 2020). ISSN: 15517616. DOI: 10.1063/5.0028916.
- [58] Vast Solar. URL: <https://vast solar.com/>.
- [59] Esolar. URL: <http://www.esolar.com/>.
- [60] URL: <https://www.springer.com/it>.
- [61] SolarPILOT. URL: <https://www.nrel.gov/csp/solarpilot-background.html>.
- [62] MATLAB. URL: <https://it.mathworks.com/products/matlab.html>.
- [63] Thermoflex. URL: <https://thermoflow.com/>.
- [64] National Renewable Energy Laboratory. URL: <https://www.nrel.gov/>.
- [65] URL: <https://climate.onebuilding.org/>.
- [66] A. Zeghoudi, M. Debbache, A. Hamidat. “Contribution to minimizing the cosine loss in a thermodynamic solar tower power plant by a change in the target position”. In: *European Journal of Electrical Engineering* 19 (5-6 2017), pp. 367–374. ISSN: 21167109. DOI: 10.3166/EJEE.19.367-374.
- [67] URL: <https://infosys.beckhoff.com/>.
- [68] G. Gentile et al. “Dynamic thermal analysis and creep-fatigue lifetime assessment of solar tower external receivers”. In: *Solar Energy, under review*. (2022).
- [69] ASME. URL: <https://www.asme.org/codes-standards>.

- [70] M.R. Rodriguez-Sanchez, A. Sanchez-Gonzalez, C. Marugan-Cruz, D. Santana. “Flow patterns of external solar receivers”. In: *Solar Energy* 122 (Dec. 2015), pp. 940–953. ISSN: 0038092X. DOI: 10.1016/j.solener.2015.10.025.
- [71] K. Cooreman Magnus. “Techno-Economic Analysis of Multi-Tower Solar Thermal Power Plants”. In: (2021).
- [72] B. Kelly, D. Kearney. *Parabolic Trough Solar System Piping Model*. 2002. URL: <http://www.osti.gov/bridge>.
- [73] M. Sarvghad, S. Delkasar Maher, D. Collard, M. Tassan, G. Will, T.A. Steinberg. “Materials compatibility for the next generation of Concentrated Solar Power plants”. In: *Energy Storage Materials* 14 (Sept. 2018), pp. 179–198. ISSN: 24058297. DOI: 10.1016/j.ensm.2018.02.023.
- [74] URL: <https://www.engineeringtoolbox.com/>.
- [75] I. Sutton. “Plant Design and Operations”. In: *Second Edition* (2017).
- [76] A.M. Bonanos, M.C. Georgiou, K.G. Stokos, C.N. Papanicolas. “Engineering aspects and thermal performance of molten salt transfer lines in solar power applications”. In: *Applied Thermal Engineering* 154 (May 2019), pp. 294–301. ISSN: 13594311. DOI: 10.1016/j.applthermaleng.2019.03.091.
- [77] I.E. Idel’chik. “Handbook of hydraulic resistance”. In: (1966).
- [78] F.M. White, University of Rhode Island. “Fluid Mechanics”. In: *Fourth Edition* ().
- [79] F. Sutter et al. “Dynamic corrosion testing of metals in solar salt for concentrated solar power”. In: *Solar Energy Materials and Solar Cells* 232 (Oct. 2021). ISSN: 09270248. DOI: 10.1016/j.solmat.2021.111331.
- [80] D.A. Arias, A. Gavilán, R. Muren. *Pumping power parasitics in parabolic trough solar fields*. 1150. URL: <https://www.researchgate.net/publication/303718533>.
- [81] D. Belverato. “Off-Design analysis of Steam Rankine Cycles for CSP application”. In: (2021).
- [82] Google Earth. URL: <https://www.google.it/intl/it/earth/>.
- [83] Global Wind Atlas. URL: <https://globalwindatlas.info>.
- [84] C.A. Asselineau, J. Pye, J. Coventry. “Exploring efficiency limits for molten-salt and sodium external cylindrical receivers for third-generation concentrating solar power”. In: *Solar Energy* 240 (July 2022), pp. 354–375. ISSN: 0038092X. DOI: 10.1016/j.solener.2022.05.001.
- [85] T. Conroy, M.N. Collins, J. Fisher, R. Grimes. “Levelized cost of electricity evaluation of liquid sodium receiver designs through a thermal performance, mechanical reliability, and pressure drop analysis”. In: *Solar Energy* 166 (May 2018), pp. 472–485. ISSN: 0038092X. DOI: 10.1016/j.solener.2018.03.003.

- [86] J. Stalin, M. Jebamalai. *Receiver Design Methodology for Solar Tower Power Plants*. 2016.
- [87] Haynes International. *Haynes 230*. 2021. URL: <http://haynesintl.com>.
- [88] System Advisor Model. URL: <https://sam.nrel.gov/>.
- [89] G. Ausburger. *Thermo-economic optimisation of large solar tower power plants*. 2013.
- [90] M.A. Meybodi, A.C. Beath. “Techno-economic analysis of supercritical carbon dioxide power blocks”. In: (2017).
- [91] A. Pfahl et al. “Progress in heliostat development”. In: *Solar Energy* 152 (2017), pp. 3–37. ISSN: 0038092X. DOI: 10.1016/j.solener.2017.03.029.
- [92] A. De la Calle, A. Bayon, J. Pye. “Techno-economic assessment of a high-efficiency, low-cost solar-thermal power system with sodium receiver, phase-change material storage, and supercritical CO₂ recompression Brayton cycles”. In: *Solar Energy* 199 (Mar. 2020), pp. 885–900. ISSN: 0038092X. DOI: 10.1016/j.solener.2020.01.004.
- [93] T. Bauer et al. *Suggested Citation CSP-Reference Power Plant Final Report*. URL: <https://elib.dlr.de/141315/https://blog-tractebel.lahmeyer.de/publications/>.
- [94] F. Zaversky et al. *Techno-Economic Optimization and Benchmarking of a Solar-Only Powered Combined Cycle with High-Temperature TES Upstream the Gas Turbine*. 2020.
- [95] T. Conroy, M.N. Collins, J. Fisher, R. Grimes. *Thermohydraulic analysis of single phase heat transfer fluids in CSP solar receivers*. 2018.
- [96] A.A. Robbiati. *Sviluppo di un codice di calcolo per l’ottimizzazione di un impianto solare termodinamico con fluido termovettore gassoso*. 2013.
- [97] V.T. Cheang, R.A. Hedderwick, C. McGregor. “Benchmarking supercritical carbon dioxide cycles against steam Rankine cycles for Concentrated Solar Power”. In: *Solar Energy* 113 (Mar. 2015), pp. 199–211. ISSN: 0038092X. DOI: 10.1016/j.solener.2014.12.016.
- [98] C.S. Turchi et al. *CSP Systems Analysis - Final Project Report*. 2016. URL: www.nrel.gov/publications.
- [99] ARERA - Autorità di regolazione per Energia, Reti e Ambiente. URL: <https://www.arera.it/it/schede/0/faq-tica.htm#>.
- [100] Wikipedia. URL: https://en.wikipedia.org/wiki/List_of_photovoltaic_power_stations.

A | Appendix A

Design and annual efficiency calculation [-].

$$\eta_{optical,des} = \frac{Q_{rec,des}}{Q_{sun,des}}$$

$$\eta_{receiver,des} = \frac{Q_{HTF,des}}{Q_{rec,des}}$$

$$\eta_{piping,des} = \frac{Q_{HTF,net,des}}{Q_{HTF,des}}$$

$$\eta_{powerblock,des} = \frac{P_{el,des}}{Q_{in,PB,des}}$$

$$\eta_{auxiliary,des} = 1 - \frac{P_{HTF,pump,des}}{P_{el,des}}$$

$$\eta_{solar-to-electric,des} = \eta_{optical,des} \cdot \eta_{receiver,des} \cdot \eta_{piping,des} \cdot \eta_{powerblock,des} \cdot \eta_{auxiliary,des}$$

$$\eta_{optical,ann} = \frac{\sum_1^{8760} Q_{rec,year}}{\sum_1^{8760} Q_{sun,year}}$$

$$\eta_{receiver,ann} = \frac{\sum_1^{8760} Q_{HTF,year}}{\sum_1^{8760} Q_{rec,year}}$$

$$\eta_{piping,ann} = \frac{\sum_1^{8760} Q_{HTF,net,year}}{\sum_1^{8760} Q_{HTF,year}}$$

$$\eta_{powerblock,ann} = \frac{\sum_1^{8760} P_{el,year}}{\sum_1^{8760} Q_{in,PB,year}}$$

$$\eta_{auxiliary,ann} = 1 - \frac{\sum_1^{8760} P_{HTF,pump,year}}{\sum_1^{8760} P_{el,year}}$$

$$\eta_{solar-to-electric,ann} = \frac{\sum_1^{8760} P_{el,year}}{\sum_1^{8760} Q_{sun,year}}$$

B | Appendix B

The design efficiency results are given in Table B.1 for Tucson clear, Table B.2 for Calgary, and Table B.3 for Tucson hazy.

Design efficiencies [%] – Tucson clear	3 x Polar	2 x Surr.	Conventional
Optical	62.1	65.4	62.9
Receiver	87.6	88.9	89.8
Piping	99.7	99.7	>99.9
Power block	40.8	40.8	40.8
Auxiliary	94.4	92.3	92.5
Solar to electric	20.9	21.9	21.4

Table B.1: Design efficiencies of the modular and conventional plants for Tucson clear

Design efficiencies [%] – Calgary	3 x Polar	2 x Surr.	Conventional
Optical	65.0	61.9	59.1
Receiver	87.7	89.0	88.9
Piping	99.7	99.7	>99.9
Power block	40.9	40.9	40.9
Auxiliary	93.7	89.7	92.3
Solar to electric	21.8	20.1	19.8

Table B.2: Design efficiencies of the modular and conventional plants for Calgary

Design efficiencies [%] – Tucson hazy	2 x Surr.	Conventional
Optical	61.2	58.3
Receiver	89.4	89.0
Piping	99.7	>99.9
Power block	40.3	40.3
Auxiliary	92.5	94.2
Solar to electric	20.3	19.7

Table B.3: Design efficiencies of the modular and conventional plants for Tucson hazy

List of Figures

1.1	Global temperature anomaly compared to pre-industrial levels [1]	1
1.2	Total annual anthropogenic GHG emissions by gases 1970 – 2010 [5]	2
1.3	Historical trend of the CO ₂ atmospheric concentration [1]	2
1.4	Total energy supply per capita over gross national income per capita of all the countries worldwide [8]	4
1.5	EU natural gas price trend [€/MWh] in the last five years, updated to 21/10/2022 [10]	5
1.6	Global weighted average LCOEs [\$/kWh] from newly commissioned, utility-scale renewable power generation technologies, 2010 – 2021 [11]	5
1.7	Renewable electricity generation by source (non-combustible), OECD Total 1990 – 2020 [14]	6
1.8	Effect of VRES electricity generation on the grid [16]	7
2.1	Concentrating solar thermal power global capacity, by country and region, 2011 – 2021 [18]	9
2.2	Examples of the Air Mass coefficient [19]	10
2.3	Yearly Direct Normal Irradiation worldwide [kWh/m ² y] [20]	11
2.4	Schematic diagrams of the four Solar Thermal Energy systems [21]	13
2.5	Schematization of a CSP tower plant with direct configuration [22]	15
2.6	PSI 10 and PSI 20 CSP plants, located in Andalusia, Spain [23]	16
2.7	Crescent Dunes CSP plant, located in Nevada, USA [24]	16
2.8	Cylindrical (left) [26], cavity (middle) [27], and Billboard (right) [28] receivers	17
2.9	Concrete tower in the Cerro Dominador CSP plant, Chile [29]	18
2.10	Steel lattice 80m tower in SUPCON Delingha 10 MW plant [32]	19
2.11	Steel monopole 55m towers in Sierra SunTower plant [35]	19
2.12	Steel monopole 127m tower in Sundrop plant [37]	20
2.13	Indirect (up) and direct (down) configurations of CSP plants [42]	21
2.14	Schematization of a thermocline storage system [43]	22

2.15	Fraction of annual DNI-weighted energy reflected by every heliostat to the adjacent field's central receiver during the daylight hours over the year. h_T is the tower height and f_X is the relative distance between the towers [52]	25
2.16	Jemalong modular pilot plant by Vast Solar [58]	27
2.17	Sierra Sun Tower modular plant by eSolar [60]	28
3.1	Schematic of the methodology	32
3.2	Trend of the attenuation losses as a function of the slant range for DELSOL clear and hazy day models [61]	34
3.3	Radial stagger layout method [61]	36
3.4	Cornfield layout method [61]	36
3.5	Cosine loss mechanism [66]	38
3.6	Azimuth angle and Zenith angle [67]	39
3.7	Typical flux asymmetry on cylindrical receivers [25]	41
3.8	Cross section of the receiver tubes and heat transfer mechanism [68]	43
3.9	Layout of the Billboard receiver (left) and cylindrical receiver (right)	43
3.10	Schematization of the piping system's modelling of a modular plant	46
3.11	Example of the layout matrix for the layout illustrated in Figure 3.10	46
3.12	Flow diagram for the piping model of modular plants	47
3.13	Geometry of an expansion loop [75]	49
3.14	Thermal resistance network in the piping system's tubes	50
3.15	Example of the trends of thermal losses (left), HTF pump consumption (middle), specific costs of piping (right) as a function of the HTF velocity	53
3.16	Example of the piping efficiency (left), external surface – ambient temperature difference (middle), and conductive resistances (right) as a function of the ambient temperature	54
3.17	Schematization of the 1-reheat steam Rankine cycle on Thermoflex	55
3.18	Schematization of the 2-reheats steam Rankine cycle on Thermoflex	56
3.19	Flow diagram of the steps and optimizations for the design of a modular CSP plant	59
3.20	Flow diagram of the steps and optimizations for the design of a conventional CSP plant	60
4.1	Annual DNI and annual ambient dry temperature in the two locations	65
4.2	Decision tree for the cases analysed	66
4.3	Cost functions for the towers	73
4.4	Cost functions for the receivers	74

4.5	Cost of a new overhead transmission line as a function of the power and the distance from the closest MV/HV substation	76
5.1	Analysis of the discretizations of the Billboard receiver's model	81
5.2	Optical efficiency maps for cornfield modules (left) and radial stagger field (right)	82
5.3	Shading effect in cornfield layouts with azimuth angle equal to 90° and low elevation angle	83
5.4	Receiver tubes' outer diameter optimization for a 0.89 x 0.89 m (left) and a 4.65 x 4.65 m (right) Billboard receiver	83
5.5	Design combined efficiency and LCOH as a function of the peak flux, at different tower heights, for the modular plant	85
5.6	Design combined efficiency and LCOH as a function of the peak flux, at different tower heights, for the conventional plant	85
5.7	Field layout and receiver flux map as a function of the tower location, for square surrounded modules in Tucson	86
5.8	Field layout and receiver flux map as a function of the tower location, for square surrounded modules in Calgary	86
5.9	Reflective area, receiver area, optical efficiency, thermal efficiency, combined efficiency and LCOH, as a function of the tower location in square surrounded modules in Tucson (red) and Calgary (blue)	87
5.10	Field layout and receiver flux map as a function of the tower location, for free surrounded modules in Tucson	89
5.11	Field layout of 25 MW _{th} free surrounded modules with 1 MW/m ² maximum heat flux (left) and 2 MW/m ² maximum heat flux (right), in Tucson	90
5.12	Combined efficiency at design conditions as a function of the tower location, for different modules' sizes in Tucson (left) and Calgary (right)	90
5.13	Optimal tower heights for different modules as a function of the power size	92
5.14	Land consumption of different layouts as a function of the power size for Tucson clear (left), Calgary (middle) and Tucson hazy (right)	93
5.15	Cosine, attenuation, spillage and blocking efficiencies of the different layouts as a function of the power size for Tucson clear (left) and Calgary (right)	94
5.16	Optical, thermal, and combined efficiencies of the layouts as a function of the power size for Tucson clear (left), Calgary (middle) and Tucson hazy (right)	96
5.17	Cylindrical (left) and Billboard (right) heat flux maps for 25 MW _{th} modules	97

5.18	LCOH of the different layouts as a function of the power size for Tucson clear (left), Tucson hazy (middle) and Calgary (right)	98
5.19	Layout of the modular plants with 3 polar square modules (left) and 2 surrounded square modules (right)	101
5.20	Layout of the conventional plant	101
5.21	Specific CAPEX of the components of each plant, for Tucson clear (left), Calgary (middle) and Tucson hazy (right)	107
5.22	Direct costs breakdown of each plant for Tucson clear	108
5.23	LSP comparison between PV and CSP plants at Tucson's latitude	109
5.24	Piping, PB, and solar-to-electric efficiency function of the electric power . .	111
5.25	Specific costs of the piping systems and PB function of the electric power .	112
5.26	Land consumption (left) and the LCOE (right) for the modular plants and many adjacent conventional plants	113

List of Tables

2.1	Advantages and disadvantages of modular plants over conventional plants	30
3.1	Input sections and main outputs of the solar field model on SolarPILOT	33
3.2	Standard diameters and thicknesses employed in the tubes optimization	42
3.3	TES operating strategy	59
4.1	Climatic data and assumptions for the two locations	67
4.2	Design thermal power and heliostat's side of the investigated modules	67
4.3	Data and assumptions for the solar field layouts	68
4.4	SolarPILOT default settings for the heliostats' design	68
4.5	Receivers' input parameters in SolarPILOT	69
4.6	Data and assumptions for the receiver thermal model	70
4.7	Data and assumptions for piping system and TES	70
4.8	Electric power values studied with the PB models	71
5.1	Power, land size, and LCOH of the least-cost modules for Tucson clear	99
5.2	Power, land size, and LCOH of the least-cost modules for Calgary	99
5.3	Power, land size, and LCOH of the least-cost modules for Tucson hazy	99
5.4	Main design parameters and results for Tucson clear	102
5.5	Main design parameters and results for Calgary	103
5.6	Main design parameters and results for Tucson hazy	103
5.7	Annual efficiencies of the modular and conventional plants for Tucson clear	105
5.8	Annual efficiencies of the modular and conventional plants for Calgary	105
5.9	Annual efficiencies of the modular and conventional plants for Tucson hazy	105
5.10	Land-specific productivity of plants in the three scenarios	108
5.11	Levelized cost of electricity of plants in the three scenarios	109
5.12	Set of modular plants analysed	111
B.1	Design efficiencies of the modular and conventional plants for Tucson clear	127
B.2	Design efficiencies of the modular and conventional plants for Calgary	127
B.3	Design efficiencies of the modular and conventional plants for Tucson hazy	128

Ringraziamenti

Sono stati cinque anni piacevoli, un po' stressanti a causa della pandemia, ma tutto sommato mi sono divertito.

Innanzitutto, vorrei ringraziare il Prof. Manzolini per la disponibilità che ha mostrato in questi mesi e per avermi sempre fornito indicazioni precise, obiezioni mirate e commenti brillanti, permettendomi di migliorare e arricchire regolarmente il mio lavoro. Un meritatissimo grazie va anche all'Ing. Gentile e all'Ing. Morosini per avermi seguito quotidianamente anche in date inusuali e ad orari inconsueti, oltre che al Prof. Binotti che mi ha fornito buona parte del materiale.

Ma anche i miei genitori, Marina e Raffaele, hanno fatto la loro parte. Mi avete sempre cresciuto in piena libertà, assecondandomi e supportandomi nelle mie scelte con ogni mezzo, senza mai imporre nulla che andasse contro i miei progetti, i miei desideri. Se sono qui oggi è certamente grazie a voi. Vi voglio bene.

Bisogna ammettere poi che questo percorso sarebbe stato molto più arduo senza miei amici. Nicolò, Eleonora, Sarah, Sara, Riccardo, Federico, Isabella, Francesca, Matteo, Daniele, Gregorio, Anna, Alice, Erika e molti altri non meno importanti. Nei mesi, negli anni, siamo cresciuti e cambiati insieme, ci siamo aiutati, supportati e sopportati oltremodo, abbiamo condiviso serate, birre, viaggi, kebab, sogni, disgrazie, idee, multe, colazioni, foto, canoe, film, go-kart, stimolanti riflessioni notturne e tanto di quell'affetto che questa tesi in confronto è un post-it. Grazie per esserci sempre stati, grazie perché ci sarete sempre.

A mio nonno Giovanni, infine, dedico la tesi. La passione che ho per la tecnologia è solo merito tuo.

